DISSERTATION

submitted to the

COMBINED FACULTY OF MATHEMATICS, ENGINEERING
AND NATURAL SCIENCES

of

HEIDELBERG UNIVERSITY, GERMANY

for the degree of

DOCTOR OF NATURAL SCIENCES

Put forward by

Luisa Bergmann

born in: Ulm, Germany

Oral examination: April 30, 2025

Jet-hadron correlations with respect to the event plane in PbPb and pp collisions at $\sqrt{s_{\mathrm{NN}}}$=5.02 TeV with ALICE

Referees:	Prof. Dr. Johanna Stachel apl. Prof. Dr. Monica Dunford
Scientific Advisor:	Alice Ohlson

ABSTRACT

In relativistic heavy-ion collisions, a deconfined medium with high energy density is created, the quark-gluon plasma. Jets -– originating from primordial hard scatterings -– act as useful probes for the properties of this medium. As the initial partons traverse the quark-gluon plasma, they lose energy by interacting with the constituents of the medium. The study of this so called ”jet quenching” yields insight into the properties of the medium.

By analyzing the angular correlations of jets with charged hadrons and comparing the per-trigger yields in PbPb and pp collisions (I_{AA}), one obtains information about the energy loss of jets in the medium. The study of these correlation functions for different orientations of the jet to the event plane allows for testing of the importance of dependence of the I_{AA} observable on the in-medium path length. This thesis presents measurements of the I_{AA}, measured with data from the ALICE detector at the LHC. As part of this thesis, an unfolding procedure for jet-hadron correlations was developed, showing in a closure test good agreement between the truth and re-weighted distributions. The measurement of the I_{AA} exhibits signatures of jet energy modifications, with an ordering of ratios with the event planes. Out-of-plane jets show higher yields than in-plane jets. However, evaluating the I_{AA} as function of the PbPb centrality suggests that fluctuations are the dominant effect for jet energy modifications over the path-length dependence.

KURZFASSUNG

In relativistischen Schwerionen-Kollisionen wird ein Medium mit hoher Energiedichte erzeugt, das Quark-Gluon Plasma. Jets – entstehend aus Streuungen mit hohem Impulsübertrag – sind eine nützliche Messgröße um die Eigenschaften dieses Mediums zu untersuchen. Während die ursprünglichen Partonen das Quark-Gluon Plasma durchqueren verlieren sie Energie bei der Wechselwirkung mit den Teilchen des Mediums. Die Untersuchung dieses so genannten "jet quenchings" ermöglicht Einblicke in die Eigenschaften den Mediums.

Durch die Analyse von winkelabhängigen Korrelationen der jets mit den geladenen Hadronen und dem Vergleich der Produktion an Teilchen pro Trigger-Jet in PbPb und pp (I_{AA}), werden Informationen über den Energieverlust von Jets im Medium gewonnen. Die Untersuchung dieser Korrelationsfunktionen für verschiedene Orientierungen des Jets zur Symmetrieachse des Events erlaubt das Evaluieren der Wichtigkeit der Weglänge im Medium für die I_{AA} Observable. Diese Arbeit präsentiert die Messung des I_{AA} für Daten die mit dem ALICE Detektor am LHC aufgenommen wurden. Als Teil dieser Arbeit wurde eine Unfolding-Technik für Jet-Hadronen Korrelationen entwickelt. Der Closure-Test zeigt eine gute Entsprechung zwischen der wahren und der gewichteten Verteilung. Die Messung des I_{AA} zeigt Anzeichen von Jet-Energie Modifikationen, wobei die Anordnung des Verhältniswerts einer Symmetriachsen-Ordnung folgt. Jets transvers zur Symmetrieachse zeigen eine höhere Teilchenproduktion als Jets die parallel zur Symmetrieachse verlaufen. Die Auswertung des I_{AA} als Funktion der Zentralität in PbPb Kollisionen stellt zur Vermutung, dass Fluktuationen einen größeren Einfluss auf Jet-Energie Modifikationen haben als die Weglänge.

CONTENTS

LIST OF FIGURES

LIST OF TABLES

1 Introduction

The matter that builds the world around us, consisting on the most fundamental level of quarks and leptons, interacts on a microscopic level via four fundamental forces [1]. In increasing order of interaction strength those are gravity, the weak interaction, electromagnetism and the strong interaction. With the exception of gravity, they are described by the standard model of particle physics. The study of these forces enables us to gain insight into the foundational laws of our universe.

1.1 Quantum Chromo Dynamics

Quantum chromodynamics (QCD) is the theory of the strong interaction [1]. The charge associated with this force is the color charge. All fermions that carry color charge, which are the quarks, partake in the strong interaction. Since the exchange bosons, the gluons, also carry this color charge, QCD behaves differently from the other fundamental forces which decrease in strength with increasing distance of two participants. When two colored objects are separated, the self-interactions of the gluons result in an increasing potential in the color field, as can be also seen schematically in Fig. 1.1. Therefore, to seperate two colored objects to larger distances, increasing amounts of energy are necessary. At the point where the energy in the color field becomes larger than the rest mass of fundamental particles, it becomes energetically advantageous to create new particles from this color field. Thus, preventing color fields from forming on a long range, quarks

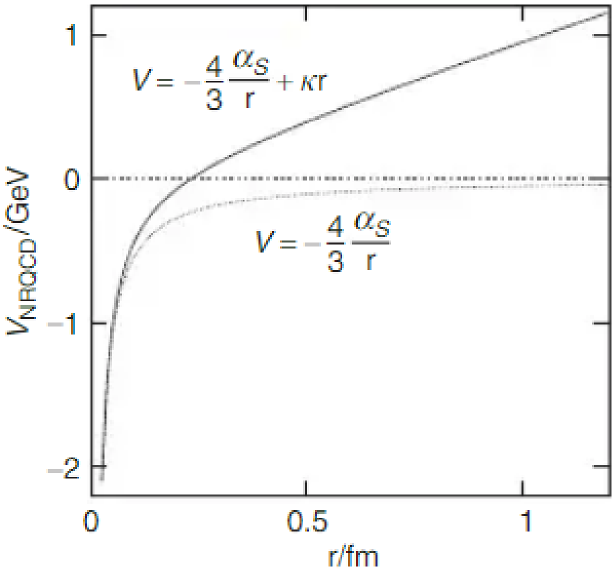

Figure 1.1: Non-relativistic QCD potential between a quark and an anti-quark, with the assumptions $\alpha_s = 0.2$ and $\kappa = 1\,\mathrm{GeV/fm}$ [1].

and gluons build colorless hadrons. This is known as confinement and the reason why single quarks and gluons cannot be observed in nature.

Another consequence of the gluon self-interaction is its effect on the running strong coupling constant α_s. As can be seen in Fig. 1.2, for each (QCD) process, there are higher order corrections, eg. quantum loops. There is no upper limit for these corrections, and due to the self-interactions of gluons they do not decrease in strength for increasing order, as is the case for example in electromagnetism. This leads to a diverging integral when cal-

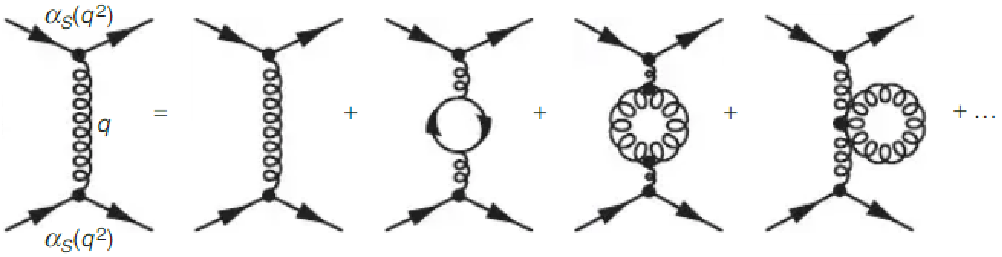

Figure 1.2: Higher order corrections to a leading order QCD Feynman diagram [1].

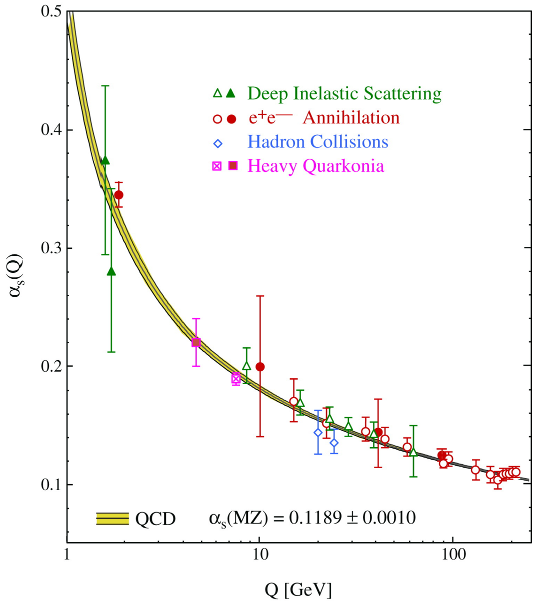

Figure 1.3: The QCD calculation of α_s with the Z boson mass as reference scale. Different measurements are shown as well [2].

culating interaction cross sections. Therefore, these higher order corrections are absorbed into the definition of the coupling constant, in a so called renormalization process, resulting in a scale dependent α_s [1]:

$$\alpha_s(Q^2) = \frac{\alpha_s(\mu^2)}{1 + B\alpha_s(\mu^2)\ln\frac{Q^2}{\mu^2}}, \quad B = \frac{11N_c - 2N_f}{12\pi} \tag{1.1}$$

Q^2 is the momentum transfer in the process. μ is an energy reference scale and N_c, N_f the number of colors and quark flavors, respectively. Fig. 1.3 shows the QCD calculation for α_s using the Z boson mass as reference energy scale, along with measurements from different experiments. At low Q^2 the constant diverges, reflecting the confinement nature of the strong interaction. However, at high energy scales, α_s is small, allowing for a perturbative treatment of strong processes. This is called asymptotic freedom and indicates that quarks and gluons behave as quasi free particles at high energies.

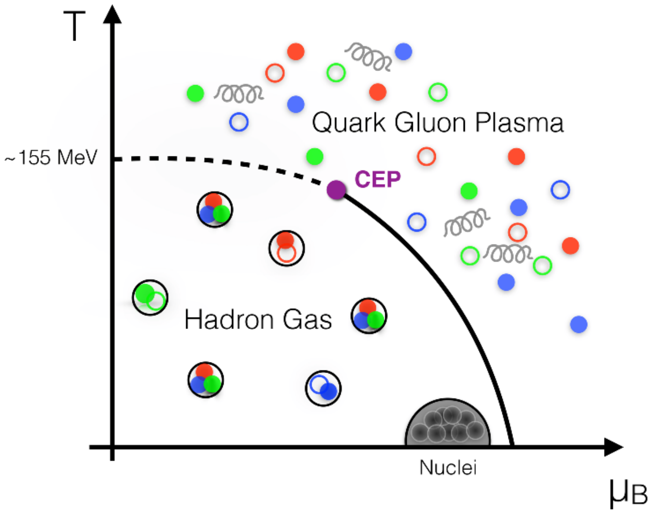

Figure 1.4: Schematic QCD phase diagram showing the states of hadronic matter for different temperatures and baryon chemical potential [3].

1.2 The QCD phase transition and quark-gluon plasma

There are different states of hadronic matter. Fig. 1.4 shows the QCD phase diagram, where the temperature of quarks and gluons is plotted against the baryon chemical potential. At normal conditions, i.e. low temperature and baryon chemical potential, matter exists as nuclei. However, when matter is heated up and/or compressed to high degrees, confinement is broken and the matter undergoes a phase transition. Lattice QCD calculations show [3] (see also Fig. 1.5) that there is an increase in energy density when matter is heated beyond a critical temperature T_c, with a flattening curve at higher temperatures. The critical temperature was recently calculated with high precision to be at $T_c = 156.5 \pm 1.5$ MeV [24, 25]. This coincides with a change of dominant degrees of freedom from hadrons to quarks and gluons [3] and a phase transition of the nuclear matter. This new state of matter is then called quark-gluon plasma (QGP). Fig. 1.5 also shows the calculation result for a non-interacting quark-gluon gas. Since this is above the

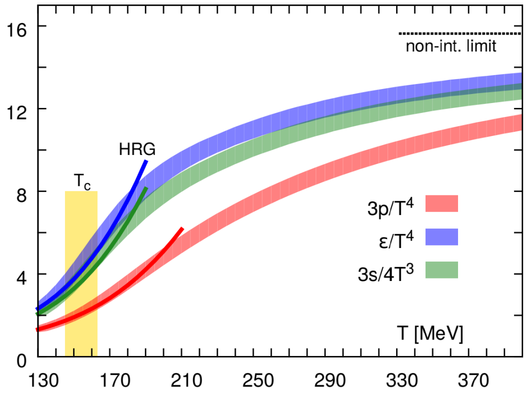

Figure 1.5: Calculations of the energy density, pressure and entropy of hadronic matter at different temperatures, together with a calculation of the critical temperature. The grey dashed lines indicates the limit for a non-interacting quark-gluon gas [4].

expected energy density of the QGP, this indicates remaining strong interactions between the plasma constituents.

Due to the remaining interactions between the quarks and gluons in the plasma, studying the QGP gives access to the most fundamental aspects of the strong force and the behavior of quasi-free quarks and gluons. In addition, more than being just a theoretical concept, the QGP also appears in the macroscopic world. It has been suggested that the universe was in a QGP state shortly after the Big Bang and underwent the phase transition in the other direction, as well as for the presence of QGP matter in the core of neutron stars [26, 27], making the QGP also an interesting research ground to deepen our understanding of the world.

1.3 HEAVY-ION COLLISIONS

While "real-life" environments like the Big Bang or neutrons stars are highly interesting to study, they are hard to impossible to access in a way to be able to study the quark-gluon plasma and its properties. The state of matter can, however, be created for a very short amount of time in heavy-ion collisions. For nuclear matter to undergo the phase transition to a QGP, extreme nuclear densities or temperatures are necessary. This can be achieved in high energy colliders like RHIC [28] at the Brookhaven National Laboratory or the LHC at CERN, described in more detail in Ch. 3.

In colliders, heavy nuclei (gold at RHIC and lead at the LHC), are accelerated to near the speed of light, reaching center of mass energies of up to 5.36 TeV in a collision at the LHC. They are then collided at the interaction points, resulting in energy densities high enough to produce the QGP. Fig. 1.6 shows the space-time evolution of such a collision. The x-axis indicates the ion beam position, while the y-axis indicates the time. At $t = 0$ the two beams collide. The quarks and gluons contained in the ions, liberated for a short amount of time from confinement, begin to interact and move towards a state of thermal equilibrium. This happens over a timespan of $\tau_0 \leq 1$ fm/c. Over the next ~10 fm/c, the produced droplet of QGP expands and cools down from its initial temperature until it reaches the critical temperature T_c. At this point, the quarks and gluons undergo a phase transition in the other direction and build out a hadron gas. The newly built hadrons can still collide inelastically while the gas is expanding and cooling further, changing abundancies of different particle types. When the chemical freeze-out temperature T_{ch} is reached, the hadrons don't scatter inelastically anymore and the particle cocktail is fixed. After the (kinetic) freeze-out temperature T_{fo} is reached, elastic scatterings between the particles stop and the kinematic profile is fixed. The particles spread out further and eventually reach the detector.

CENTRALITY AND FLOW

The initial conditions of the collision influence the behaviour of the bulk particles during the evolution. Parameters like the number of nucleons that participate in the collision are determined by the impact parameter, which is defined as the distance between the centers of the two colliding ions. For small impact parameters the overlap region of the two nuclei is large and the number of participants is as well. For larger impact parameters and

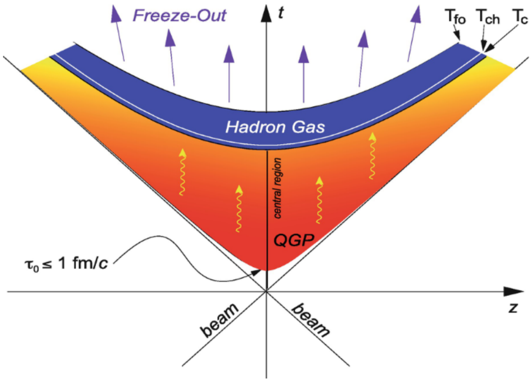

Figure 1.6: Space-time evolution of a heavy ion collision, indicating the different phases of matter [5]

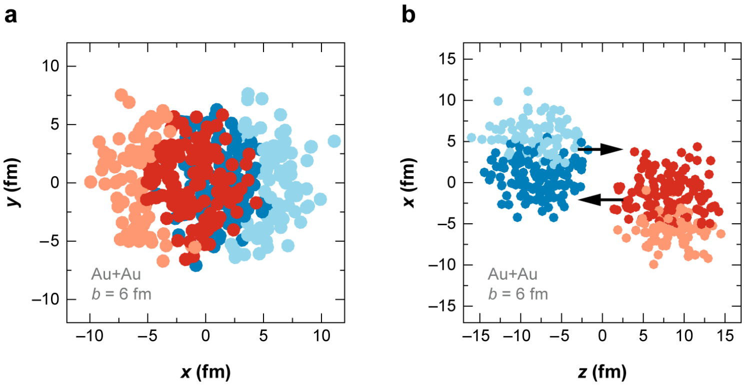

Figure 1.7: Glauber Monte Carlo event, in the transverse plane (left) and along the beam axis (right). The participants are depicted in darker colours. The collision is simulated for two gold ions at an impact parameter of 6 fm. Taken from [6]

smaller overlap regions, the number of participating nucleons is accordingly smaller. In the Glauber model [6], the heavy ion collision is modeled as a series of individual nucleon-nucleon collisions. Fig. 1.7 depicts such a Glauber Monte Carlo event for the collision of two gold ions, both in the transverse plane as well as along the beam axis. The two nuclei are colored in red and blue, where the darker shades indicate the participating nucleons. In the Glauber model, the number of participants, along with other parameters of the collision, can be calculated from the impact parameter and the inelastic nucleon-nucleon cross section $\sigma_{\text{inel}}^{\text{NN}}$.

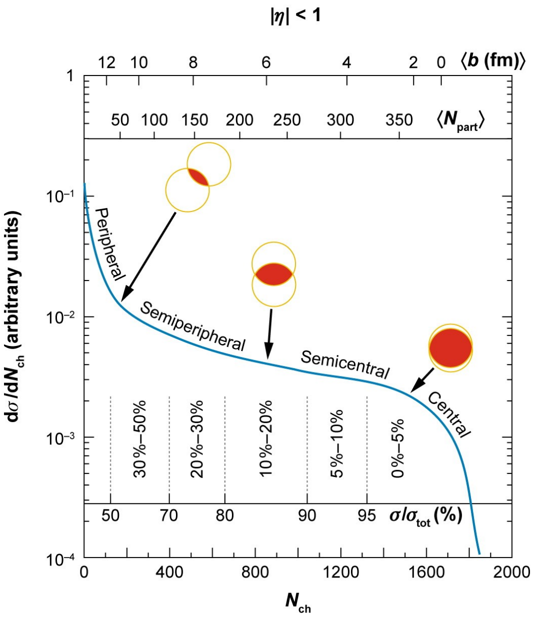

Figure 1.8: Schematics of centrality determination [6]

While the number of participants cannot be accessed directly in real collisions, existing measures can be used to classify an event in a Glauber picture. For events with low impact parameter and large number of participants, the number of measured particles at midrapidity will be large, while the number of particles measured in forward and backward direction (non-participating nucleons from the collision) will be low. The reverse is true for high impact parameters. Fig. 1.8 shows schematically the multiplicity distribution of charged particles N_{ch} per event, measured at midrapidity. Assuming a monotonous relationship between the number of charged particles and the number of participants and impact parameter, those quantities are depicted as well. To classify an event, this distribution is divided into percentiles of the interaction cross section, 0 % being the most "central" and 100 % being the most "peripheral" collisions.

Other quantities that are defined by the geometry of the collision are the "reaction plane" and "participant plane". The reaction plane is defined by the impact parameter and the beam direction. Fig. 1.9 shows the reaction plane from the transverse perspective, where x_{RP} corresponds to the vector in impact parameter direction and y_{RP} is the

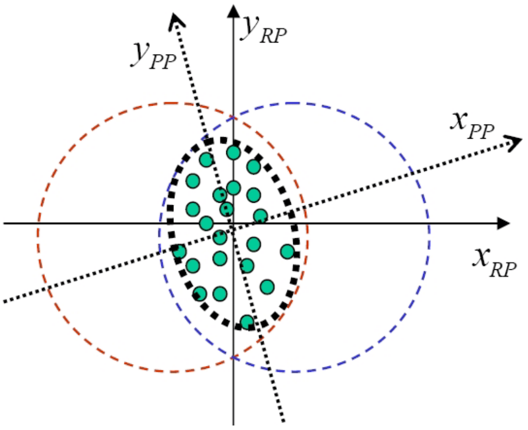

Figure 1.9: Schematic depiction of the reaction plane and participant plane [7].

normal vector to the reaction plane. In non-central collisions, the reaction plane acts as a symmetry plane for the overlap region. Due to fluctuations of the nucleon positions within the nucleus, the participant plane is defined as a further symmetry plane. It is also depicted in 1.9. Depending on the positions of the nucleons inside the ions, the participant plane may deviate from the reaction plane. The reaction and participant planes, similar to the number of participants, are not directly measurable. They can, however, be approximated by the distribution of particles in the event. The experimental quantity is then called the "event plane". The method used in this thesis to reconstruct the event plane is discussed in chapter 5.

Due to the asymmetric shape of the overlap region in non-central events, the energy density distribution is not azimuthally isotropic. At the center, where many nucleons participate in the collision it is much higher than at the tips. This translates into a pressure gradient inside the collision region and forming QGP, resulting in a boost of particles along the participant plane. Fig. 1.10 shows the distribution of charged particles relative to the event plane measured by the STAR experiment, clearly demonstrating the preferred direction of particles being alongside the event plane rather than transverse to it. The effect increases for higher centralities i.e. more asymmetric overlap regions.

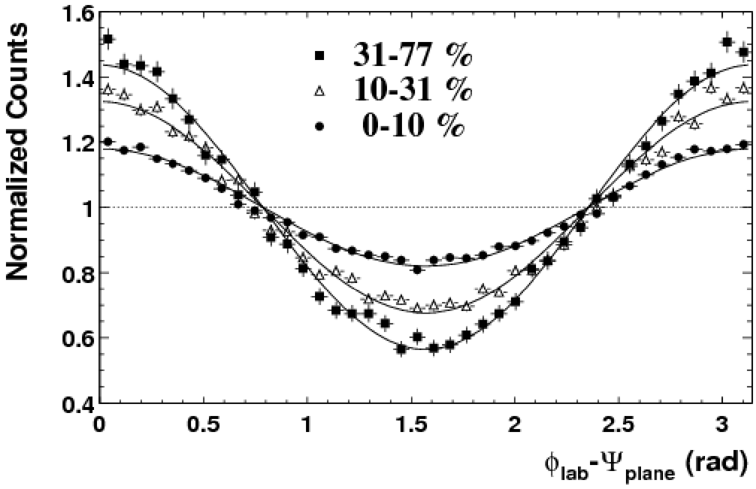

Figure 1.10: Distribution of charged particles with respect to the event plane for different centralities [8].

The distribution of particles relative to the event plane can be described by a Fourier expansion

$$\frac{\mathrm{d}N}{\mathrm{d}(\phi-\Psi_n)} \propto 1+\sum_{n=1}^{\infty} 2v_n\cos(n(\phi-\Psi_n)), \tag{1.2}$$

where ϕ is the azimuthal angle of the measured particles and Ψ_n is the n^{th} order event plane with n being the order of the anisotropy. v_n are called the flow coefficients. Even v_n are connected to the symmetry of the overlap region, while odd v_n emerge due to fluctuations in the nucleon positions [29]. The dominant contribution to the particle distribution is v_2, with higher order harmonics decreasing in strength [30].

1.4 OUTLINE

In this thesis, measurements probing the properties of the QGP will be presented. In the next section, the measurement tools used in this work, jets and correlation functions, are discussed. The experimental apparatus (the LHC and ALICE) and the basic data and track selection will be described in sections 3 and 4, respectively. The analysis procedure is explained in section 5, followed by a discussion of the results in section 6. The findings of this thesis are summarized in section 7.

2 JETS AND CORRELATION FUNCTIONS

The QGP, described in the previous chapter, has a plethora of interesting features that can be explored. In this chapter, one probe of these features is introduced, the jet. The access to this measurand via correlation functions as well as some analysis tools for the evaluation of jets in hadronic collisions are described.

2.1 JET PRODUCTION

Early in the hadronic collision, a fraction of the partons scatter with a high momentum transfer Q^2 [9]. These so called hard scatterings produce two partons that are emitted back-to-back from the collision point with a high transverse momentum. The hard partons undergo a fragmentation and subsequent hadronization process, resulting in sprays of particles that can be detected and are called jets. Following the factorization theorem, the jet production calculation can be divided into three parts [9]. They are shown schematically in Fig. 2.1. The parton distribution functions (PDFs) $f_A(x_1, Q^2)$ and $f_B(x_2, Q^2)$ describe the momentum distributions of the partons of the colliding nuclei A and B, where $x_{1/2}$ are the momentum fractions of the total momentum. $\sigma(x_1, x_2, Q^2)$ is the scattering cross section of the two partons. The fragmentation process is described by the fragmentation function $D_{i \to h}(z, Q^2)$ which describes the probability that a parton

i fragments into a hadron h that carries the momentum fraction z of its mother parton. The production cross section for a high momentum particle h can then be calculated as

$$d\sigma^{\text{hard}}_{AB\rightarrow h} = f_A(x_1,Q^2) \otimes f_B(x_2,Q^2) \otimes d\sigma(x_1,x_2,Q^2) \otimes D_{c\rightarrow h}(z,Q^2). \qquad (2.1)$$

The terms ISR and FSR in Fig. 2.1 denote initial and final state radiation, respectively. This is radiation emitted by the partons entering or leaving the hard scattering.

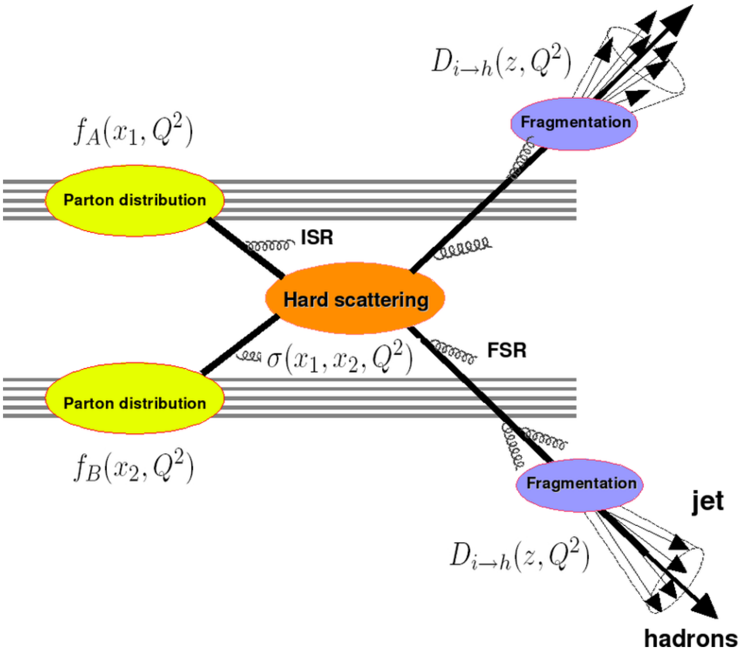

Figure 2.1: Schematic representation of the jet production process [9]

While both the inital momentum distribution for the scattering partons and the fragmentation process lie in the non-perturbative regime of QCD, they can be described universally and measured in deep inelastic scatterings and e^+e^- collisions, respectively. The production rates of jets themselves, i.e. their cross section, however, can be calculated pertubatively since the high momentum transfer results in a small strong coupling constant, see Chapter 1. The prediction of jet production describes the measured data in pp collisions very well, as can be seen for example in a measurement by ALICE in Fig. 2.2. The leading order (LO) MC calculations describe the measured spectra over several orders of magnitude. Since jets are well understood in pp collisions, they make for an excellent tool to use in heavy-ion collisions. However, it has to be noted that the presence of effects like FSR leads to an ambiguity in what is defined as a jet. Radiation emitted at a large angle will usually not be included in the final object, while radiation emitted close to the partons axis will. In order to facilitate comparability between different experiments and theory, it was agreed upon in the 1990 Snowmass accords [31] to standardize the used jet reconstruction algorithms, see also Ch. 5.2.

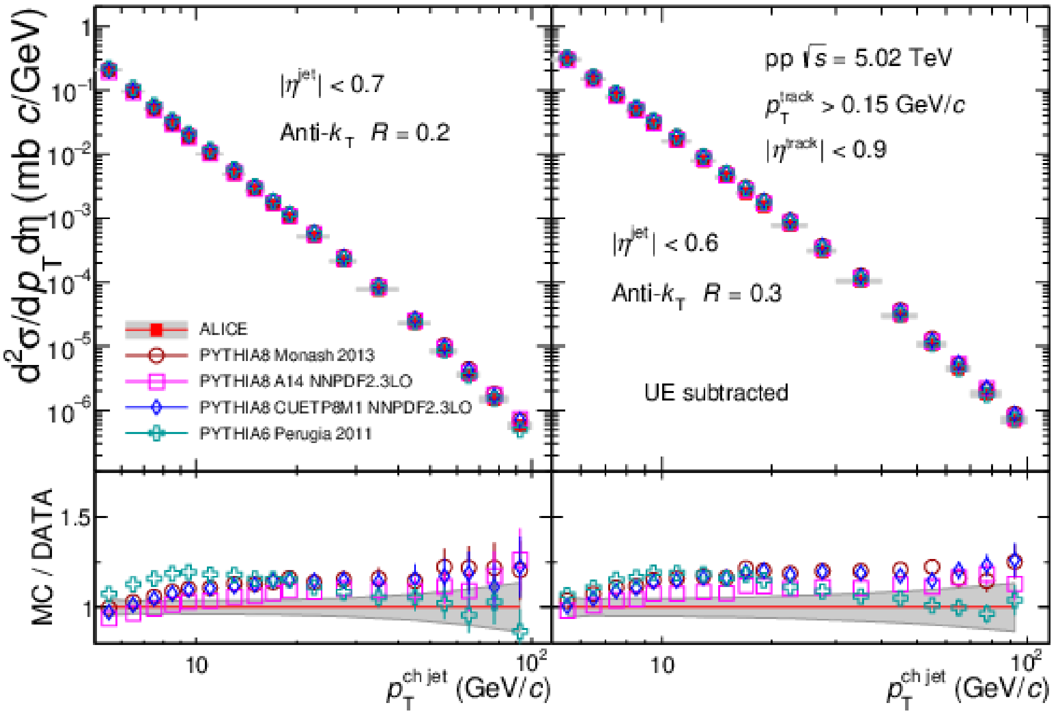

Figure 2.2: Measured jet cross section in pp collisions, compared to LO MC calculations [10].

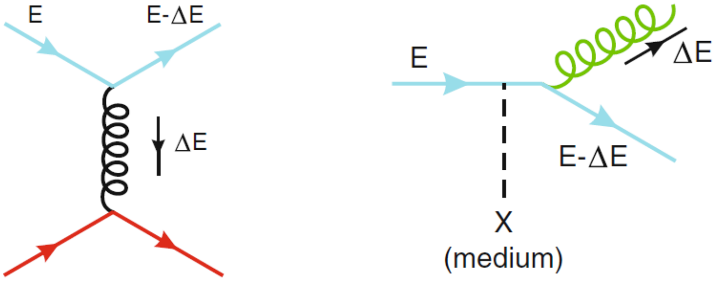

Figure 2.3: Collisional (left) and radiative (right) energy loss [9]

2.2 Energy loss mechanisms

The jet production described in the previous section occurs on a relatively short timescale $\tau \sim 0.1\,\mathrm{fm/c}$ [9], while the QGP forms on a timescale $\tau \sim 1 - 2\,\mathrm{fm/c}$. This means that the jets travel through the QGP as it evolves, and the interaction between the hard scattered partons and the quarks and gluons in the medium leads to a momentum transfer between the two. This modification of the jet's momentum leads to a suppression of high p_T objects when comparing heavy-ion collisions to pp collisions, where no QGP is formed. This can also be seen in previous measurements, shown further down in this chapter. In the context of this thesis, the process of hard scattered partons transferring a fraction of their momentum to the mediums constituents in interactions is also more shortly referred to as "energy loss", "momentum loss" or "jet energy modification". The main mechanisms by which the jet loses energy to the medium are collisions with the particles of the QGP and radiative energy loss, shown schematically in Fig. 2.3.

At low particle momenta, energy is mainly transferred through elastic collisions between particles and scales linearly with the particles path length L in the medium [9]. Radiative energy loss occurs via inelastic scatterings between particles, where the traversing particles emit gluon bremsstrahlung. This is the main loss mechanism for high momentum particles and therefore expected to be the prevalent process for jets [9]. Radiative energy loss theoretically scales with L^2 [32]. However, for thick media where L is much larger than the mean free path, the Landau-Pomeranchuk-Migdal (LPM) [33–35] effect takes hold. This effect describes the destructive interference between radiated gluons, resulting in a reduction of radiative energy losses.

The study of jet energy loss in a medium, specifically its dependence on the path length of the jet in the medium, is very informative about the interaction properties of the QGP and therefore some of the fundamental properties of the strong force. One example for this is the transport coefficient $\hat{q}$ [9], which connects the properties of the medium, like energy density and the cross section for parton-medium interactions, to the average transverse momentum transferred by the parton per unit path length.

Energy loss of high momentum particles has been measured both at RHIC [11] and the LHC [12]. Fig. 2.4 shows measurements of the nuclear modification factor

$$R_{\mathrm{AA}} = \frac{\mathrm{d}N_{\mathrm{AA}}/\mathrm{d}p_{\mathrm{T}}}{\langle N_{\mathrm{coll}}\rangle \mathrm{d}N_{\mathrm{pp}}/\mathrm{d}p_{\mathrm{T}}}, \tag{2.2}$$

which compares the number of (high momentum) particles in pp and nucleus-nucleus collisions, normalized by the average number of nucleon-nucleon collisions. In both cases, a clear suppression (R_{AA}<1) of the number of particles is visible in central collisions. The ALICE measurement (bottom plot) additionally shows the measurement for peripheral collisions. Due to the higher impact parameter and less participating nucleons in these collisions, the energy density is lower, resulting in less suppression. In p-Pb collisions, where no QGP is expected to be formed, no significant suppression can be observed. Similarly, the PHENIX measurement shows the result for direct photons, which are not suppressed in heavy-ion collisions compared to pp collisions. This is expected, since photons do not carry a color charge and therefore do not interact strongly with the medium.

A further observable that demonstrates energy loss of particles in a QGP medium is the softening of jet fragmentation patterns. This is explored further in the following.

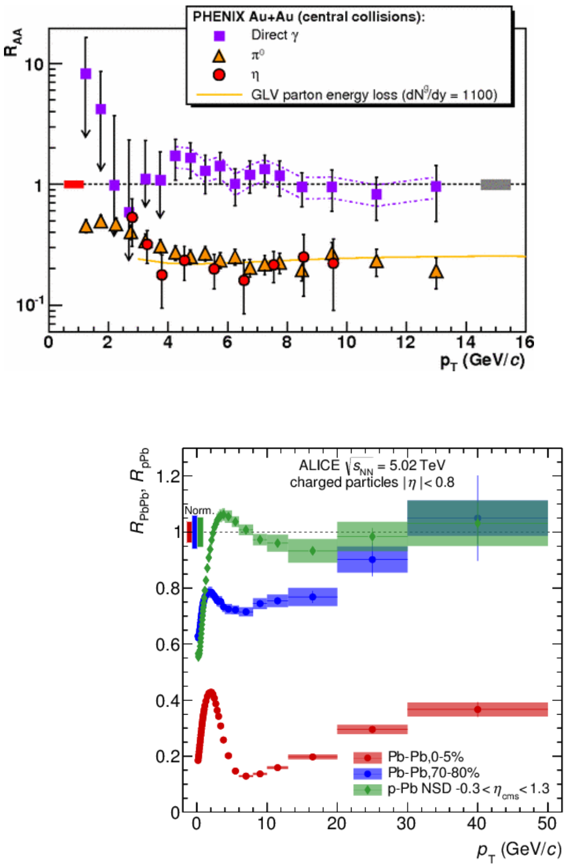

Figure 2.4: Top: Nuclear modification factor R_{AA} for η,π^0 and direct γ, measured by the PHENIX collaboration [11]. Bottom: R_{AA} measurements of charged particles in PbPb and p-Pb collisions by the ALICE experiment [12].

2.3 JET-HADRON CORRELATIONS

The measurement of jet energy modifications in heavy-ion collisions is a complicated task. As has been shown in the previous chapter, high energy collisions of heavy nuclei do not only yield jets, but also a bulk of underlying particles. Since the exact origin of each single measured particle is not known, an assignment to "jet" or "background" is not possible. Instead, a clustering algorithm (see Sec. 5.2) has to be applied. This produces both real jets that actually do stem from hard scatterings, as well as fake jets that are reconstructed from soft background particles. The discrimination between fake and real jets is not obvious and impossible on an jet-by-jet basis. This is especially true for low jet momenta, where the medium modifications are expected to be most prevalent and where there are a lot of combinatoric jets. Furthermore, in the case of real jets, the background particles get clustered together with jet particles and distort the energy and momentum measurements. This distortion is heightened by detector resolution effects.

The use of jet-hadron correlations circumvents some of these complications by looking at jets on a statistical basis over many events. For the correlation functions, jets are reconstructed with a clustering algorithm to provide a first estimate of the jet axis and momentum. Then, the relative position of selected particles in the event, the associated particles, to this jet axis are calculated:

$$\Delta\varphi = \varphi_{\text{jet}} - \varphi_{\text{assoc. particle}} \tag{2.3}$$

$$\Delta\eta = \eta_{\text{jet}} - \eta_{\text{assoc. particle}} \tag{2.4}$$

where φ is the angle in azimuth and η is the pseudorapidity. The relative angles for all pairs are filled into a histogram. An example for such a 2D correlation function, produced with a toy event generator, can be seen in Fig. 2.5. The peak at $\Delta\varphi = \Delta\eta = 0$ corresponds to the particles that are emitted as part of the jet. This is called the near-side

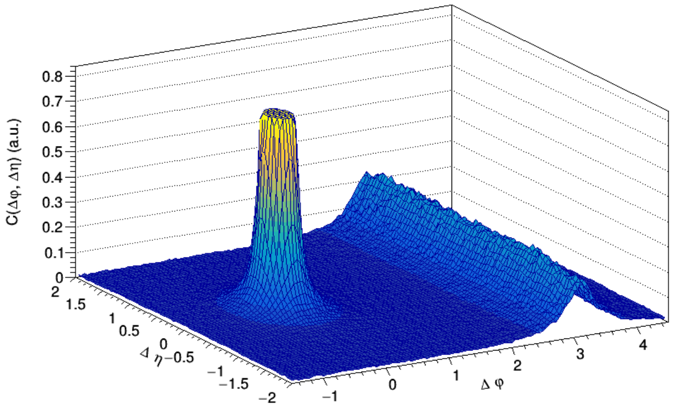

Figure 2.5: 2D correlation function from a toy event generator. Visible are the near-side peak at $\Delta\varphi = \Delta\eta = 0$ and the away-side ridge at $\Delta\varphi = \pi$. The near-side peak is cut off by the z-axis scale.

peak. On the away-side at $\Delta\varphi = \pi$, the particles of the back-to-back emitted jet are visible. They form a ridge extended in $\Delta\eta$ rather than a peak, since the separation of the two jets in (lab) pseudorapidity depends on the momenta of the hard scattering partons.

When comparing the the associated particle yields per jet Y_{AA} from correlation functions in heavy-ion collisions to those from pp collisions Y_{pp}, one gains access to the momentum modifications imposed by the medium:

$$I_{AA} = \frac{Y_{AA}}{Y_{pp}} \tag{2.5}$$

Typically, I_{AA} is measured as a function of p_{T} , where the associated particles are selected in different p_{T} bins. When the I_{AA} is below 1, the associated particles of the corresponding momentum are suppressed compared to pp, while $I_{AA} > 1$ significates an enhancement. With this, one can see how the presence of a medium influences the fragmentation pattern of jets. Some previous measurements of the yields and I_{AA} are shown in the following section.

Since the correlations are calculated for all particles in an event, the background contributions are as well measured on a statistical basis and can be removed as an average over many events. The complete procedure is described in detail in Chapter 5.

In order to evaluate the I_{AA}, it is important to match the jet energies in pp and PbPb to allow for comparisons that give information about the jet energy loss. This is a complicated task, that was in earlier measurements (see below) solved by for example embedding the pp data into PbPb. One goal of this thesis, beside measuring the path length dependence of the I_{AA} itself, is to improve upon the matching between jet energies in pp and PbPb. The goal is to make a comparison possible on the particle level before distortions through the detector occur, also allowing for direct comparison to theory. For this purpose, an unfolding technique was developed, which is described in detail in section 5.4.

Intuitively, the path length of the jets in the QGP can be accessed by utilizing the geometry of the collision and the position of the jet in this geometry. As has been described in Chapter 1, the overlap region of the colliding nuclei is asymmetric, especially in peripheral collisions. This means that jets that are emitted close to the symmetry plane of the event (in-plane) have a shorter path length than jets emitted perpendicular to the event plane. An illustration of this principle can be seen in Fig. 2.6. By separating the correlation functions by the relative angle of the trigger jet to the event plane, one can obtain the path length dependent momentum modifications. It should, however, be noted that some theoretical studies [36, 37] suggest that fluctuations in the jet fragmentation impose a more significant contribution on observables like the di-jet momentum asymmetry or the azimuthal anisotropies than variations in path length. With a measurement of correlation functions one can therefore also assess the significance of path length vs. fluctuations in the I_{AA} observable.

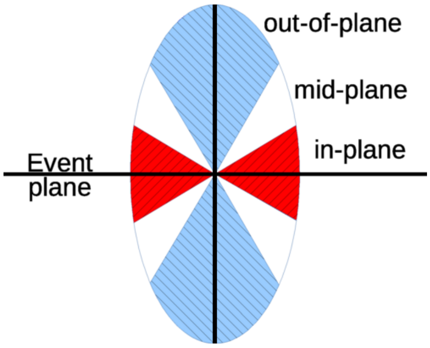

Figure 2.6: Illustration of the overlap region of a heavy-ion collision, with the symmetry plane of the event labelled as Event plane. Three regions relative to this event plane are indicated: in-plane (red), mid-plane (white) and out-of-plane (blue). Figure adapted from [13].

2.4 PREVIOUS MEASUREMENTS

Previous measurements of the I_{AA}, eg. [14], fulfilled the expectations for a sensitivity of the per-trigger yield to medium modification, cf. also Fig. 2.7. The I_{AA} is presented for the near- and away-side, for both central collisions (0-5 %) and ultra-peripheral (60-90 %) collisions. In the peripheral case, where particle densities are much lower compared to central collisions and hence less medium is produced, no significant medium modifications are observed. For the central collisions, the away-side shows substantial suppression of associated particles coinciding with energy loss in the medium. On the near-side, though, an enhancement is observed. This is still an indicator for medium modifications, though they are more involved than for the away-side. One possible explanation is a selection bias in the parton p_{T} spectrum through the trigger. By improving the matching between jet energies in pp and PbPb this issue of the trigger selection bias could be avoided. Recent model studies [38] however show that the surface bias resulting in a harder selected p_{T} spectrum on the near-side is smaller than usually expected and that trigger jet still experience a significant amount of quenching. It seems therefore more likely that the enhancement stems from a softening of the fragmentation function, where hard jet constituents are modified by the medium, leading to more jet particles that carry a smaller momentum of the hard scattered parton.

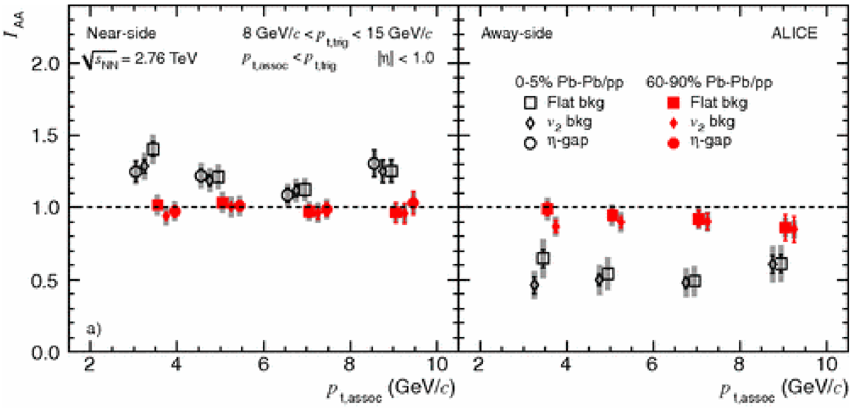

Figure 2.7: Measurement of the I_{AA} in central (0-5 %) and ultra-peripheral (60-90 %) PbPb collisions [14].

Measurements at RHIC of correlations with respect to the event plane [15, 39] show in peripheral collisions a modulation of the I_{AA} on the away-side with varying orientation of the trigger to the event plane. [15] also shows a comparison between the I_{AA} for in-plane and out-of-plane jets, Figure 2.8. A weak dependence of the ratio on the associated p_{T} is visible, though a interpretation is difficult due to the large statistical uncertainties. An ALICE measurement [13] found no significant difference of the per-trigger yields for in-plane, mid-plane and out-of-plane jets within the uncertainties. It should be noted that in all three cases the chosen centrality range is very large, likely to enhance the statistical precision. However, the shape of the overlap region is different in a collision with 20 % centrality as compared to 60 % or even 50 % centrality, leading to very different in-medium path lengths especially for in-plane jets. An effect could be obscured if it is smaller than the resolution of path lengths between those centralities.

From the previous measurements, two main conclusions can be drawn: First, the away-side can be expected to be the more interesting region to observe medium modifications and its path length dependence. And second, fine bins in centrality might be necessary to observe an effect. Furthermore, the centrality region of main interest will be the slightly peripheral ones (10-50 %), since for the most central collisions the overlap region is still quite symmetrical, i.e. little difference in path length between in-plane and out-of-plane,

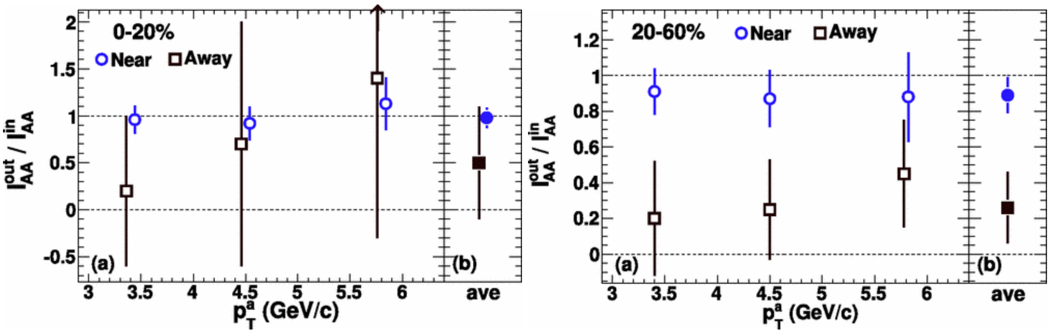

Figure 2.8: Ratios of the I_{AA} between in-plane jets and out-of plane jets for central (left) and peripheral (right) collisions [15].

and ultra peripheral collisions likely do not produce enough medium to see significant momentum modifications.

3 The Experimental Setup

3.1 Large Hadron Collider

The present analysis is done with data recorded by the ALICE experiment at the Large Hadron Collider or LHC. The LHC [40] is a circular particle collider, designed and built to collide protons and lead ions at super-relativistic energies. It is part of the European Center for Nuclear Research or CERN, situated near Geneva, Switzerland, and extending beyond the French border. With its circumference of 27 km, the LHC is able to accelerate protons and lead ions to near the velocity of light and collide them at center of mass energies of 13 TeV and 5.02 TeV for protons and lead ions respectively. After an upgrade during the long shutdown 2, even higher energies were achieved in the current run that started in 2022.

A schematic layout of the accelerator complex at CERN is shown in Fig. 3.1. The protons and lead ions are accelerated in different stages [16, 41]: The protons and lead ions are accelerated in bunches, with each bunch containing $\sim 10^{11}$ and $\sim 10^{8}$ particles of each species [42]. For the protons, negative hydrogen ions are accelerated by the linear accelerator Linac4 to 160 MeV and are then injected into the Proton Synchrotron Booster (PSB), the electrons are stripped away during this process yielding the desired protons. After acceleration in the PSB, the protons enter the Proton Synchrotron (PS), which increases the beam energy to 26 GeV. At the last pre-acceleration stage in the Super Proton Synchrotron (SPS), the protons are pushed up to 450 GeV. When the beam

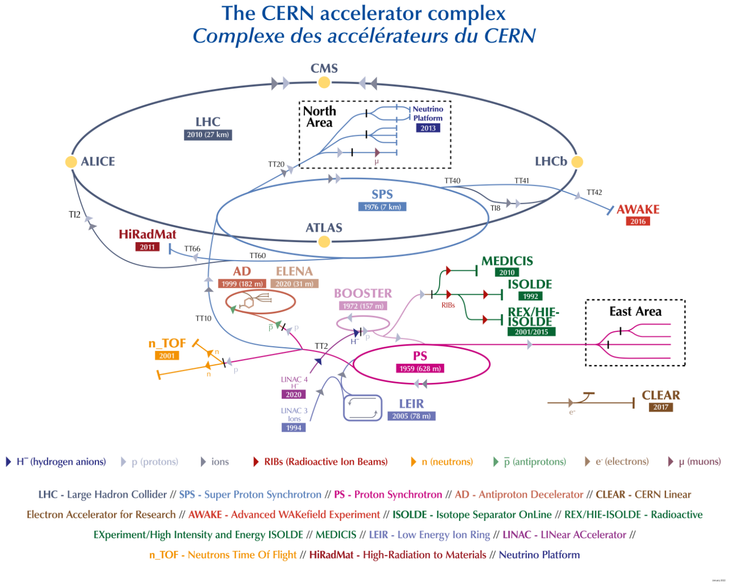

Figure 3.1: Schematic layout of the accelerator complex at CERN [16]

has reached this energy, it is injected into the LHC. The beam is split into two, one circulating clockwise and the other counter-clockwise. When it has reached top energy the beams are brought to collision in four main points where the experiments are located.

The four different experiments that take data with the LHC are ATLAS, CMS, LHCb and ALICE. ALICE, described in further detail in the following, is the dedicated heavy-ion experiment, that was designed specifically to measure the collisions of lead ions and explore the physics of the QGP.

3.2 THE ALICE DETECTOR

As mentioned before, ALICE (A Large Ion Collider Experiment) [43, 44] is the dedicated heavy-ion detector of the LHC, situated at P2 in France. The detector is operated and its data evaluated by a large collaboration consisting of over 2000 members in 41 member states [45].

The detector volume of $16 \times 16 \times 26$ m^3 contains 18 subsystems inside a solenoid magnet, depicted in Fig. 3.2. The coordinate system consists of the beam direction (z), and the transverse plane xy. The origin is located at the interaction point. Positive z values are labeled as A side, negative values as C side. ALICE consists of a collection of subdetectors with the purposes of tracking, identifiying and assigning energy and momentum measurements to the particles that emerge from the collisions.

Generally, the purposes of the subdetectors can be categorized as tracking, triggering, particle identification and energy and momentum measurement. The tracking detectors are the ITS (Inner Tracking System), the TPC (Time Projection Chamber, the main tracking detector) and TRD (Transition Radiation Detector). The TRD is also used to provide electron identification. For particle identification the TOF (Time Of Flight), HMPID and TRD were implemented. Outside of the central barrel on the C side, the muon arm (consisting of several detectors) is located, providing particle identification for muons. The Electromagnetic calorimeter (Emcal) and photon spectrometer (PHOS) provide energy measurements of various particles. The input for the trigger system is provided by different detectors like the ZDC (Zero Degree Calorimeter), V0 and TRD.

In the following, the subdetectors used in this analysis are described in further detail. As mentioned before, an upgrade was performed on several of the detectors to be able to handle the increased luminosity and rate beginning in Run3. However, since the data used in this analysis was recorded in Run2, the previous setup will be described.

3.2.1 V0

The V0 system [19] consists of two plastic scintillator arrays that are positioned close to the beam pipe on both sides of the interaction point (V0A and V0C). Both arrays are segmented into 32 parts, 8 azimuthally divided $45°$-sectors in 4 rings, shown schematically in Fig. 3.3. Due to the very fast readout time, its main purpose is to provide a trigger

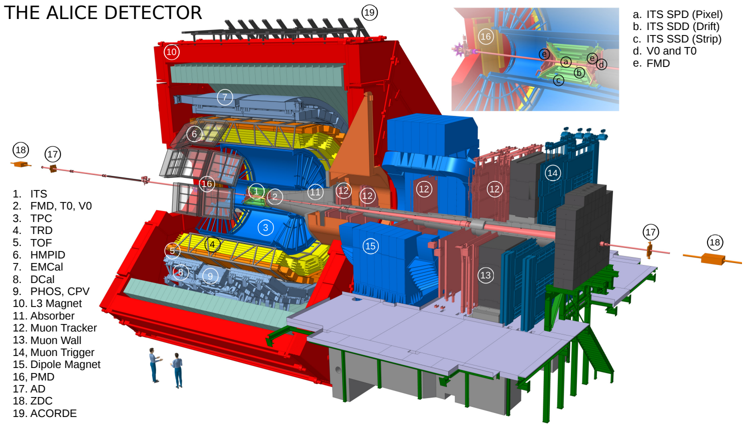

Figure 3.2: Schematic overview of the ALICE detector during Run2. Figure taken from [17]

for the central barrel detectors. Furthermore, it is used to characterize the events through measurement of the multiplicity and centrality.

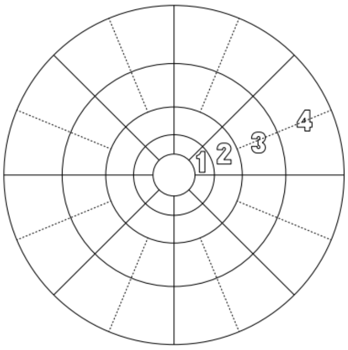

Figure 3.3: Segmentation of the V0-A/C arrays [18]

When signals in both V0A and V0C coincide, a Minimum Bias (MB) trigger is sent out to the other detectors for further evaluation. Since the number of particles registered in the V0 is proportional to the centrality of an event, explained in further detail in chapter 1.3, the V0 is also used for classified triggers in PbPb collisions. Depending on the thresholds depicted in 3.4 and the signal registered in the V0 arrays, a Central trigger or semi-Central trigger is sent out for collisions with 0-10 % and 30-50 % centrality respectively. This trigger is used to enhance the statistics of our sample of central and semi-central events.

In this analysis, the difference in readout time between the V0 and TPC is exploited to remove pileup events by comparing the measured multiplicities in both detectors (see chapter 4.2). Furthermore, the detector is used to reconstruct the event plane of each event, using the multiplicity measurement and azimuthal segmentation of the arrays. This is explained in further detail in chapter 5.1.

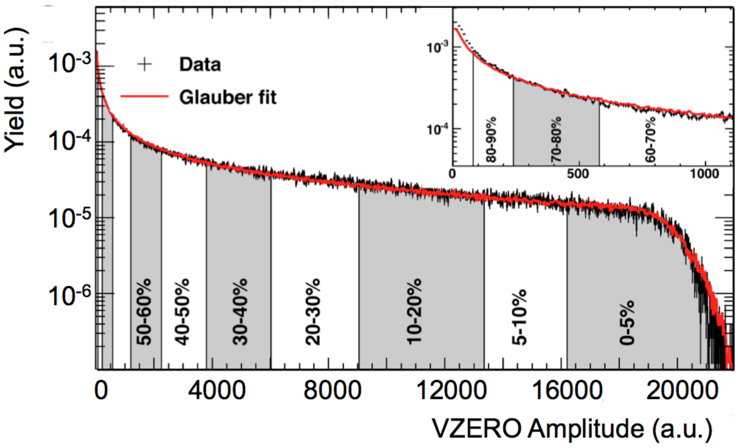

Figure 3.4: Sum of amplitudes in the V0 arrays [19]

3.2.2 TPC

The Time Projection Chamber (TPC) [20, 46] is the main tracking detector of ALICE and also provides momentum measurements and particle identification. As visible in Fig. 3.5, it is cylindrical in shape, leading to full azimuthal coverage and and an acceptance in pseudorapidity of $|\eta| < 0.9$. With an inner radius of 80 cm, an outer radius of 250 cm and a length of 5 m, the TPC has an active detection volume of 90 m^3. It is filled with a gas mixture of Ne-CO_2-$N_2$$[85.7 - 9.5 - 4.8]$. When a charged particle emerges from the collision and traverses the detection volume of the TPC, it ionizes the gas particles along its way. Due to the field cage that produces an electric field between the dividing

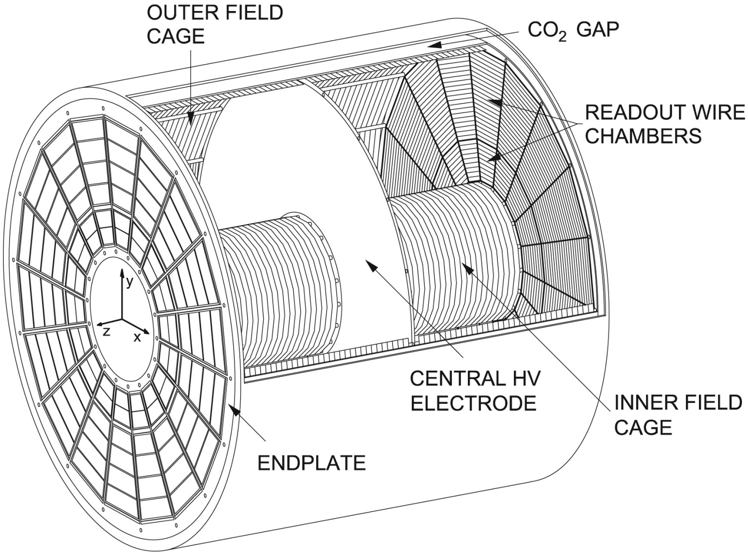

Figure 3.5: Schematic view of the ALICE TPC [20].

plate in the middle of the TPC and the two end plates, the ionization electrons drift to the Multi-Wire-Proportional-Chambers (MWPC) at the end plates and are registered at the readout electronics. In the upgrade, the MWPCs were replaced by Gas Electron Multipliers (GEMs) to allow for a continuous readout to process the higher collision rates [47].

The readout signal for each particle provides the xy location of the particle. Temporal evaluation and knowledge of the drift time from the place of ionization to the readout gives the z position. This information are used by the track reconstruction to determine the path of the particle. Due to the present magnetic field, charged particles get deflected from a straight path onto a circular one. The curvature of the track gives information about the momentum of the particle. Additionally to tracking and momentum information, the readout signal informs about the energy deposit of the particle in the detector volume, making species identification possible via the Bethe-Bloch formula. The specific energy loss for several particles as measured by the TPC is shown in Fig. 3.6.

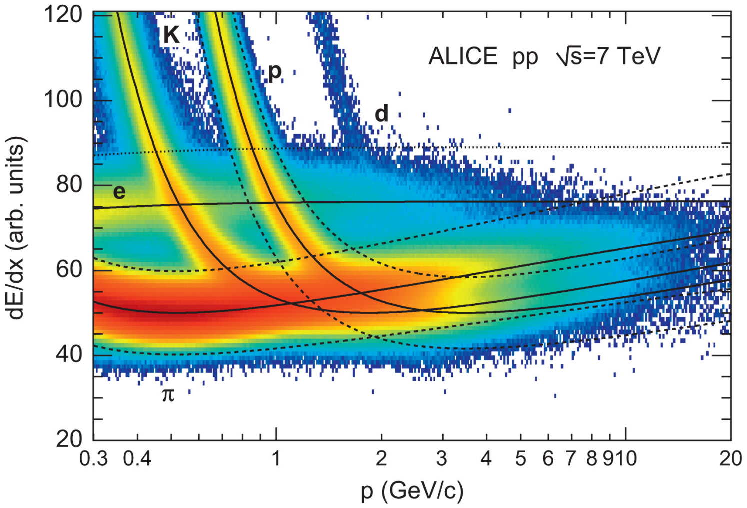

Figure 3.6: Specific energy loss in the TPC with Bethe-Bloch lines for different particles [21]

3.2.3 TRD

The Transition Radiation Detector (TRD) [22, 48] is a gaseous detector as well, installed adjacent to the TPC. It was designed to provide excellent electron identification and triggering, especially at higher (p_T >1 GeV) momenta, where the distinction of electrons from pions with the TPC is insufficient. Furthermore, the TRD is used to aid in the tracking and calibration of the central barrel detectors. The TRD consists of 18 supermodules, where each supermodule is built from 30 single chambers that are organized in 6 layers and 5 stacks. To reduce the material in front of the PHOS, the middle stacks of three chambers have not been installed, resulting in 522 usable readout chambers.

Fig. 3.7 shows on the left-hand side a schematic layout of a TRD readout chamber. To provide electron identification, the TRD makes use of transition radiation (TR) [49], which is produced when a particle traverses the boundary between two materials with different dielectric constants. To increase the probablity of radiation photons being emitted, a radiator consisting of a sandwich of fibers and foam is installed at the beginning of the chamber. This is followed by a drift region, where traversing particles ionize the xenon-based gas mixture. The ions then drift, due to the applied electric field, towards

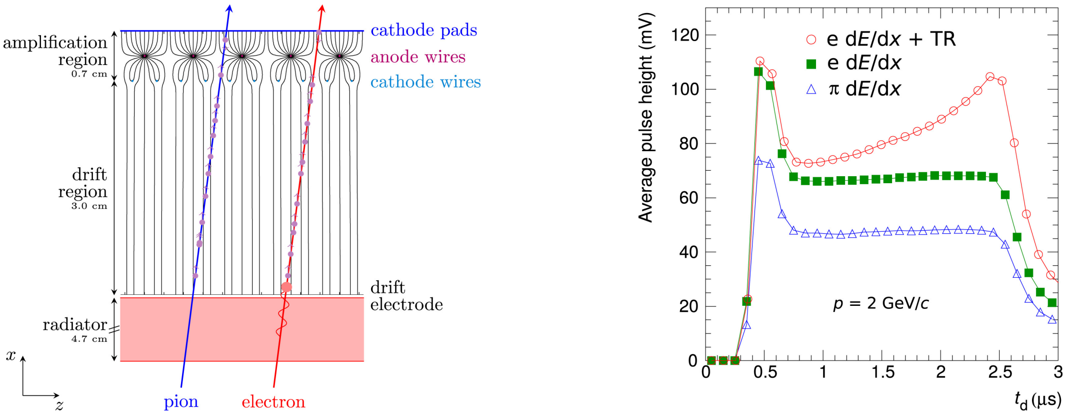

Figure 3.7: Schematic view of a TRD readout chamber (left) and a pulse-height diagram for electrons and pions (right) [22].

the amplification region, where the signal is amplified and read out. Transition radiation is proportional to the Lorentz factor γ of a particle, which means that for typical particle momenta present in collisions at the LHC, electrons will produce transition radiation but pions will not. This leads to different signals of the two particle species in the TRD, which can be used to distinguish them. Typical pulse-height spectra for electrons and pions are shown on the right-hand side of Fig. 3.7. The measured signal is plotted against time. The peak at the beginning of the spectra corresponds to the signal registered from the ions that are produced directly in the amplification region. The plateau that follows is produced by the ions that travel through the drift region. Thus, the width of the plateau is proportional to the length of the drift chamber. If an electron produces TR, the photons as well are absorbed into the gas at the beginning of the gaseous part of the chamber, leading to an increasing signal towards larger drift times.

As mentioned above, the TRD is used in the tracking for charged particles. For this, the spatial information of a traversing particle in each chamber, called tracklet, is added to the global tracking procedure. The tracking is described with more detail in ch. 4. Since the signal position in the temporal dimension is directly correlated to the radial position of a tracklet, it has to be calibrated in order to avoid a radial bias in the tracking. As part of this thesis, a study for the t_0 calibration of the TRD was done. t_0 is defined as the time

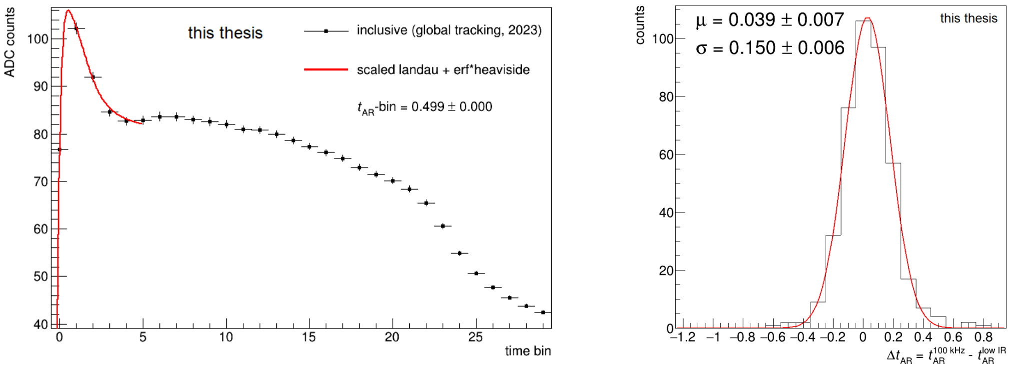

Figure 3.8: Left: Pulse-height distribution in the TRD for run3 data, including a fit to the amplification region. Right: Difference of the extracted t_{AR} between runs from July 2022 to November 2022.

offset between the central trigger and the measured signal in the TRD. For this study, the maximum of the amplification peak was used as the reference point. The exact peak position (t_{AR}) was extracted via a fit, using a scaled Landau function to describe the left-hand side flank of the spectrum and an error function multiplied by a heaviside function to describe the beginning plateau. The pulse-height spectrum for Run 3 data recorded in 2022 as well as the fit is depicted on the left in Fig. 3.8. The position of the spectrum was monitored over an extended period of time. The difference in t_{AR} between runs from July 2022 to November 2022 is shown on the right of the figure. The difference in time bins over several months is ~ 0.04, which is negligible for tracking purposes, making a monitoring of the t_0 position sufficient at present. For this, an automated fitting and monitoring procedure was developed.

3.2.4 ITS

Inside of the TPC, closest to the beampipe, lies the ITS (Inner Tracking System) [43]. It is used for primary and secondary vertex reconstruction. Furthermore, it tracks particles with low momentum and improves the resolution of the TPC. Its tracking capabilities are also used in the general tracking procedure.

The ITS consists of six layers, two each for the Silicon Pixel Detectors (SPD), Silicon Drift Detectors (SDD) and Silicon micro-Strip Detectors (SSD). The SPD and SDD layers were chosen to satisfy the needs for a high granularity due to the large track density close to the collision. In the two outmost layers, the particle density is expected to be smaller, making the SSD sufficient for tracking purposes.

3.2.5 TOF

The TOF (Time-Of-Flight) detector [50] is a detector of Multigap Resistive Plate Chambers (MRPC) located in the central barrel outside of the TPC. By comparing the signal obtained in its detector volume to the time measured for the primary collision, it measures the time-of-flight of particles with a time resolution of 56 ns. Together with momentum measurements, TOF provides particle identification in the intermediate momentum range. Similar to the V0, the fast readout time of the TOF is used in this analysis to remove pileup events.

3.2.6 Track reconstruction

The particles from the collision leave a trace while traversing the detectors. With the tracking procedure, this trace can be reconstructed and its properties used for particle identification and momentum determination. In the following, the tracking procedure in ALICE will be described briefly. A detailed description can be found in [44].

First, clusterization is done in each detector individually. Then, the clusters are used as input for the tracking. Due to the high multiplicity in heavy ion collisions, the expected occupancy closer to the interaction vertex is expected to be very high. For better separation, the tracking is therefore started at the outer layer of the TPC. The found clusters are propagated inwards using the Kalman filter technique [51], its properties updated along the way depending on the surrounding clusters. When the track reaches the ITS, it is used as a seed to start the tracking procedure there. The track is propagated further inwards through the ITS until it reaches the point of closest approach to the preliminary vertex.

In the second step of the track reconstruction, the track is refitted from inside to the outside to the found clusters. If possible, clusters from the TRD and TOF are included in this step as well. In the last step, the track is propagated inwards again and a final refit is performed.

3.3 SIMULATIONS

While the data recorded with the ALICE detector forms the basis of this analysis, simulations are also necessary to control variables like detector efficiency, proof of method for the unfolding, and to give context to the measurement result by comparison to theory predictions. In the following, the Monte Carlo (MC) event generators that are used in this thesis, either directly or by extension through official ALICE productions, are listed.

3.3.1 PYTHIA AND HIJING

PYTHIA [52] and HIJING [53, 54] are the most commonly used event generators in ALICE physics analyses. PYTHIA is a general-purpose MC event generator, that models pp collisions on three different levels, describing the hard scatterings, initial and final state radiation and multiparton interactions, and third the QCD color confinement, which is part of the hadronization process. Information important for several different processes, like parton distribution functions (PDFs), are shared between the levels. The hadronization is handled via a string fragmentation model. HIJING on the other hand is more targeted towards the study of (mini)jet production and the simulation of heavy ion collisions. It consists of two components, one based on perturbative QCD to model multiple jet productions, for soft processes a Lund-type model is employed.

For the determination of the tracking efficiency (Section 4.3.1) in PbPb and pp collisions, official HIJING and PYTHIA productions were used, respectively. To test the unfolding procedure (Section 5.4), PYTHIA was used to provide a fast event simulation. Details on the production can be found in [55].

3.3.2 JEWEL

JEWEL [56–58] is an event generator that models the evolution of jets in a medium using perturbative QCD. Evolution in a vacuum is also possible, to provide a baseline for comparison between heavy-ion and pp collisions. The initial hard scattering of a di-jet and the hadronization are done by PYTHIA. The PDFs to produce the matrix element for the jet production are provided by LHAPDF [59], here CT14nlo is used, with the nuclear modification EPPS16nlo for the simulation of heavy-ion collisions. After the initial hard scattering, the event is handed over to JEWEL to simulate the evolution in a medium or in vacuum. By default, in the first case a variation of the 1D Bjorken model [60] is used, where the medium expands only in longitudinal direction and is modeled as a collection of partons forming an ideal gas. More details on the medium model can be found in [57].

In JEWEL, not the complete collision is modelled, but only the jet particles themselves and the medium particles that interact with them. By default only the jet particles are kept in the event record. However, the medium response influences the substructure and shape of the jet, so for a more realistic description it is preferable to keep the recoils in the event. After the hadronization has been done there is no way to distinguish between original jet particles and recoils. The momentum of the recoiling particles contains their original momentum and the exchanged momentum from the interaction with the jet particle. Since in real collisions, this first part gets subtracted with the general background subtraction, the initial (thermal) momentum of the recoils has to be subtracted as well. This is done by implementing the suggested algorithm in [61] on the event level before jet reconstruction. The results can be seen in Ch. 6.

4 DATA SAMPLE AND SELECTION

For this analysis, data that was recorded in 2018 with the ALICE detector is used. The lead nuclei were collided at a center of mass energy of 5.02 TeV per nucleon pair with an interaction rate of 7.5 kHz. The pp reference samples were recorded in 2015 and 2017 at the same energy. In this chapter, the event and track selection are described. Also, an explanation for the determination of the tracking efficiency is given.

4.1 EVENT SELECTION

In total, 890M and 1519M events were collected in PbPb and pp respectively. This number is reduced by the application of some quality cuts both on the event and track level to ensure a clean data sample. On the event level, different triggers were applied. A trigger is a set of rules for the physics processes in an event in order for that event to be stored. In PbPb and pp, a minimum bias trigger and required hits in the V0 detector (kINT7) was used. In PbPb the statistics were enhanced by also using the triggers for central and semi-central events. The data was evaluated in bins of the centrality: 10-20%, 20-30%, 30-40%, 40-50%, 50-70% and 70-90%. The position of the z-vertex was restricted to 6 cm in positive and negative direction to ensure a more or less uniform acceptance. Furthermore, an event was skipped, when too few particles (<0.3 of the total number of particles in the event) pass the track selection criteria described in section 4.3. A further cut, the pileup rejections are discussed in the following.

4.2 PILEUP REJECTION

As described before, the collisions are done by accelerating bunches of ions or protons, with one bunch containing $\sim 2 \times 10^8 - 11 \times 10^{10}$ particles and bunches being spaced at 25 ns. This huge number of particles results in several collisions occuring very close to each other, both spatially and temporally. Since the readout time of the detectors is finite, a later ocurring collision can show up in the data of another collision. This is called pileup. To remove the pileup contribution, cuts have to be applied here as well. There are two types of pileup, the one occurring from crossings in the same bunch and out-of bunch pileup. In the first kind, two or more collisions occur in the same bunch. This results in particles that originate from different primary vertices and are therefore removed by applying a cut at the level of event selection to remove events with multiple reconstructed primary vertices. Out of bunch pile up stems from collisions that occur in bunch crossing different from the one that triggered the readout. Since the different detectors have varying readout times, they are affected differently by out of bunch pileup. The extra events can be removed by comparing the spatial positions of reconstructed points in drift detectors, since the different readout times leave to shifts in the spatial position.

Any remaining pile up events, that have not been removed with the cuts above – for example due to inseperable reconstructed vertices –, are cut out in the analysis itself. For this, the number of particles measured with the TOF and V0 detectors are compared to the number obtained using the TPC. The TPC has a much higher integration time ($\sim$100 μs) than the other detectors (TOF $\sim$0.5 μs), therefore pileup events will show up with a higher multiplicity in TOF and V0A/C than in the TPC. For the cuts, the 2D distributions of particle multiplicities are collected in a first run. To have the cuts ready for the actual analysis, the distributions are first fitted, and the fit result loaded into the analysis framework. Examples for distributions in one centrality bin, including the cut graphs, can be seen in Fig. 4.1 (a)-(c). The 2D distributions for the pileup cuts for all centralities and the pp collisions can be found in appendix A.1. For the fits, each bin in

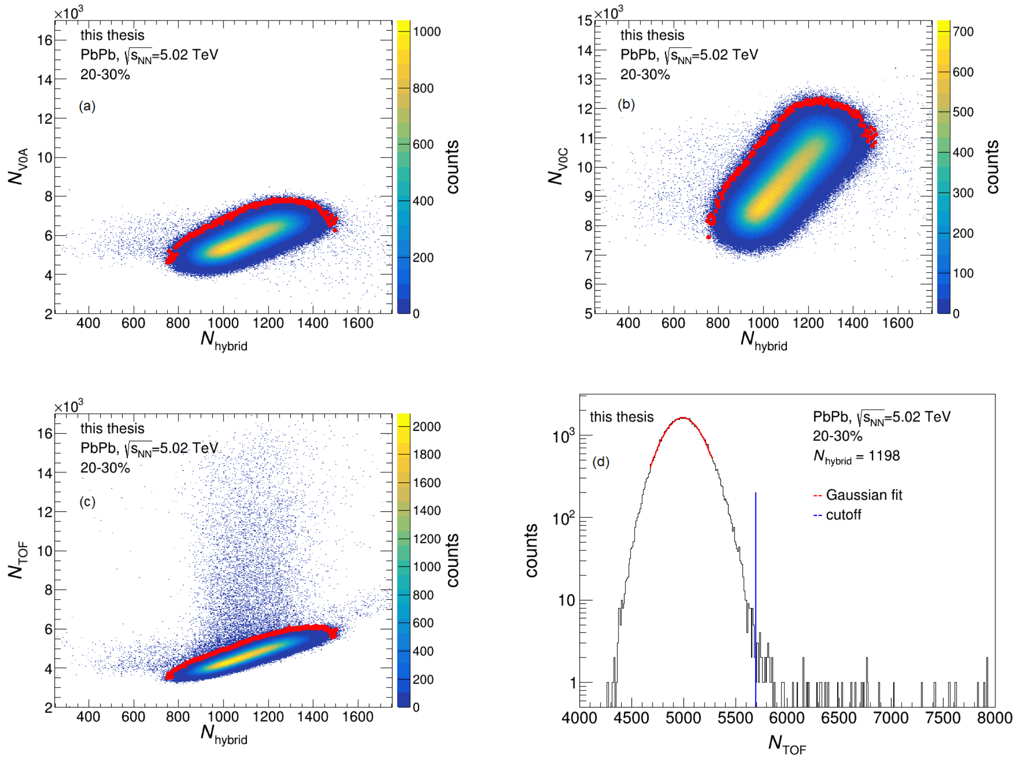

Figure 4.1: (a)-(c): 2D distributions of number of tracs in V0A,V0C and TOF vs. the measured number of hybrid tracks in the TPC. The cut graph for the pileup rejection is depicted in red. (d): Example of a projection of a 2D pileup distribution onto the N_{TOF} axis, including the Gaussian fit (red) and the cutoff value (blue).

hybrid number of tracks (x-axis) is projected onto the y-axis, which corresponds to the multiplicity measured by the TOF and V0s for this bin. The projected distributions are then fitted by a Gaussian to determine the maximums position. Any event, that yields a TOF or V0 multiplicity higher than what corresponds to 0.1% of the peak will get cut out. An example for the projection of the 2D distribution in one hybrid track bin and the corresponding fit and cut-off can be seen as well in Fig. 4.1.

4.3 TRACK SELECTION

Additionally to the basic event selection, cuts are made on the selection of tracks as well. The goal is to achieve on the one hand a clean data sample, and on the other hand an even distribution of tracks in azimuth to ensure also an even distribution of jets after reconstruction.

For this analysis, charged tracks that are reconstructed with the TPC and ITS are used. A basic selection include cuts on the momentum of the particles ($p_{\mathrm{T}} > 0.15$ GeV/c) as well as the pseudorapidity ($|\eta| < 0.9$), which correspond to a selecting a momentum range with sufficient precision and the acceptance of the TPC respectively. The basic cuts also include further restrictions on the TPC as main tracking device. A successful TPC refit (a parameter of the track reconstruction) is required, as well as a minimum amount of clusters per track (N_clus> 50) and a TPC $\chi^2 < 300$. To reduce the amount of secondary particles, the Distance of Closest Approach (DCA), i.e. the distance of the track to the primary vertex is constrained to 0.5 cm both in z and the xy plane.

Additional to the basic cuts, hybrid track cuts are applied. Those are a list of conditions on both the TPC and ITS that are commonly used in ALICE analyses and can be set with filter bits (512 and 256). Filter bit 256 are the so called global hybrid tracks, and require the track to pass standard TPC and ITS cuts, as well as hits in the SPD. Due to a missing detector area, the global hybrid cuts loose some tracks. Those can be recovered by combining filter bit 256 with filter bit 512, the complementary tracks. Those tracks also have to pass standard TPC and ITS cuts, but do not require hits in the SPD. By combining both filter bits, a uniform distribution in azimuth is achieved, as can be seen in Figure 4.2. The individual cuts that are part of the hybrid track cuts are summarized in Table 4.1.

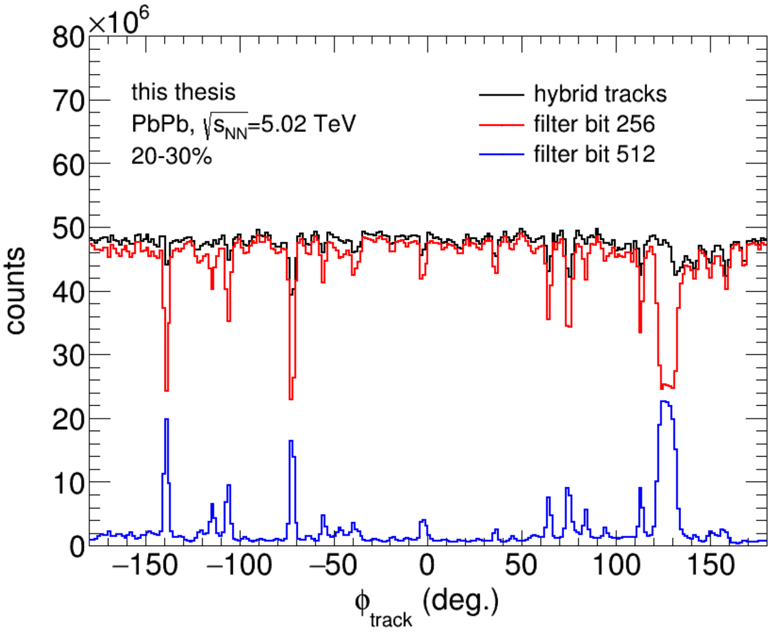

Figure 4.2: Azimuthal distribution of charged tracks after different cuts are applied

Hybrid track cuts (filter bits 256+512)
SetMinNCrossedRowsTPC(70)
SetMinRatioCrossedRowsOverFindableClustersTPC(0.8)
SetMaxChi2PerClusterTPC(4)
SetAcceptKinkDaughters(kFALSE)
SetRequireTPCRefit(kTRUE)
SetRequireITSRefit(kTRUE)
SetClusterRequirementITS(kSPD, kAny)
SetRequireSigmaToVertex(kFALSE)
SetMaxChi2PerClusterITS(36)
SetMaxChi2TPCConstrainedGlobal(36)
SetMaxDCAToVertexXY(2.4)
SetMaxDCAToVertexZ(3.2)
SetMaxFractionSharedTPCClusters(0.4)
additionally for 512
SetClusterRequirementITS(kSPD, kOff)

Table 4.1: Hybrid tracks cuts

4.3.1 Tracking efficiency

The information we gain on the particles is dependent on the detector performance. Since those are not perfect but operate with a limited efficiency, tracks that are used for entries to the correlation functions have to be corrected for this efficiency.

To get an estimate, MC simulations are utilized. For a more details, see Section 3.3 In the MC production, particles are generated according to our understanding of the physics in collisions. These particles are then propagated through a detector simulation and reconstructed using the same conditions that are applied to real data. The efficiency is then determined by the number of reconstructed particles that pass the track selection, compared to the number of originally generated particles:

$$\epsilon = \frac{\text{number of reconstructed tracks}}{\text{number of generated tracks}} \tag{4.1}$$

Since the acceptance of the detector and the p_{T} of the particle play a roll in how well a track can be reconstructed, the efficiency is collected as a function of η and p_{T} . The efficiencies for different centrality bins as well as for pp collisions can be seen in Fig. 4.3. As expected, the reconstruction efficiency is lower at the edges of the detector and drops towards $|\eta| > 0.8$. In p_{T} , the efficiency rises steeply at low momenta and stays then relatively constant at $\sim$ 80 %.

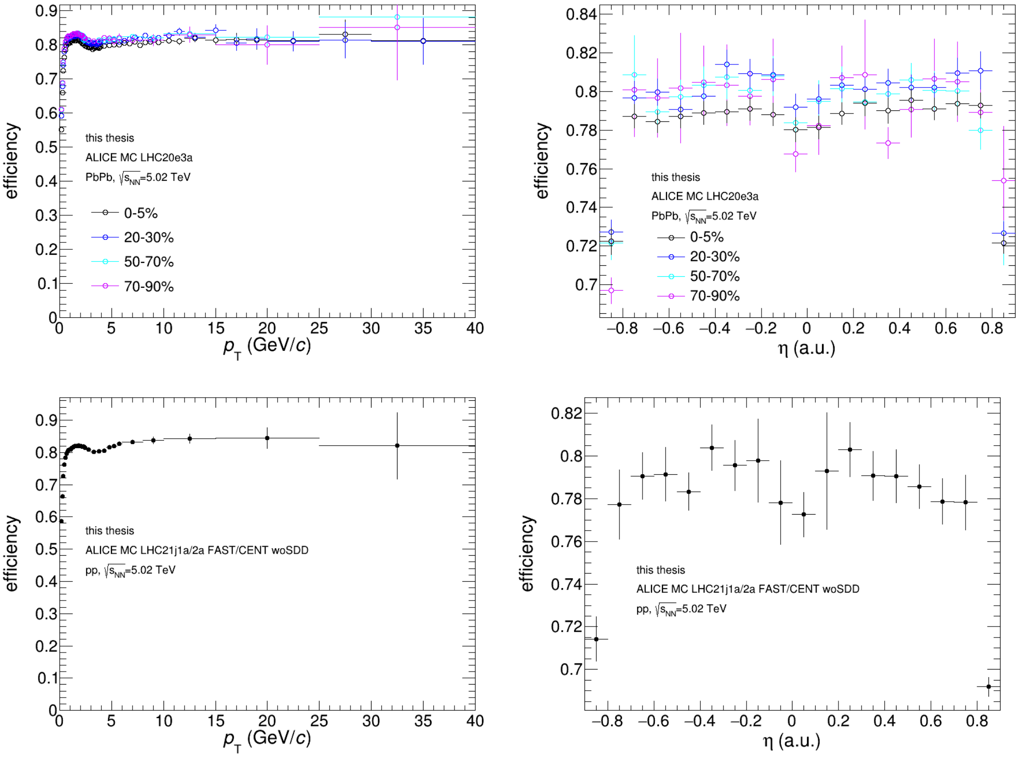

Figure 4.3: Projections of the 2D tracking efficiency on the p_T and η axes, for different centralities in PbPb (upper row) and pp (lower row).

5 ANALYSIS

The selected data sample recorded with the ALICE detector, both described in previous chapters, is used to perform the analysis aimed to determine the path-length dependence of jet-quenching in a strongly coupled medium.

As introduced in Sec. 2.3, the measurement is done by analysing jet-hadron correlations with respect to the event plane for different centralities and jet momenta. The analysis procedure consists of several steps:

1. Since the correlations are measured relative to the symmetry plane of the events, in a first step the **event plane** has to be **reconstructed**.

2. Before jet-hadron correlations can be calculated, **jets** have to be **reconstructed** and their momentum is corrected for the background energy density. Furthermore a **mixed event procedure** is used to determine the contribution of **background jets**.

3. When the jets are reconstructed, the **correlation functions** are **calculated** both in PbPb and pp collisions and **corrected** for different effects
    - acceptance correction
    - correction for uncorrelated background (ME technique)
    - subtraction of correlated background

4. To enable a direct comparison between PbPb and pp, the jet spectra are **unfolded** and the **correlations re-weighted** accordingly.

5. After all correlations have been constructed and corrected, the **observables**, the per-trigger yields of the trigger jets, are **extracted**.

The steps are explained in more detail in the following sections and the results will be discussed in Ch. 6.

5.1 EVENT PLANE DETERMINATION

Since the whole analysis is conducted with respect to the event plane as an access to the path-length of the jets in the medium, the first important step is to determine said event plane with sufficient precision.

The symmetry plane of the collision cannot be determined directly, but has to be estimated with the information available, i.e. from the final state particles. Usually, this estimation is done by comparing the distribution of particles in the x and y direction by constructing the flow vectors:

$$Q_{n,x} = \sum_i w_i \cos(n\phi_i) = Q_n \cos(n\Psi_n) \tag{5.1}$$

$$Q_{n,y} = \sum_i w_i \sin(n\phi_i) = Q_n \sin(n\Psi_n) \tag{5.2}$$

for the nth order event plane, with w_i being segment-(track-)wise weights and ϕ_i being the angle of the segment(particle) in the transverse plane with index i. With these two equations, the event plane angle can be determined:

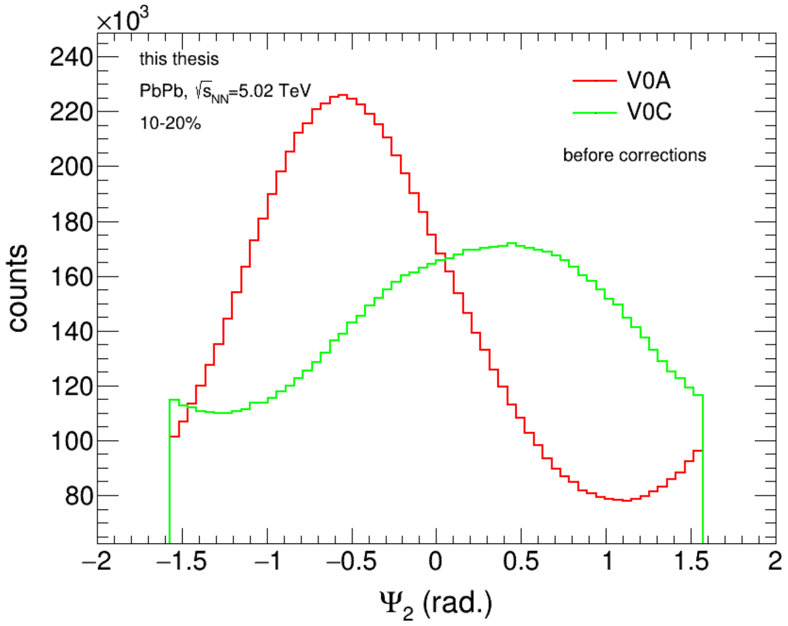

Figure 5.1: Raw event plane distribution before any corrections are applied.

$$\Psi_n = \frac{1}{n} \tan^{-1}\left(\frac{Q_{n,y}}{Q_{n,x}}\right) \tag{5.3}$$

In this analysis, the second order event plane is used, i.e. $n = 2$. In order to avoid possible self-correlations that would arise if the TPC is used both for the calculation of the event plane and the correlations, the V0 detector is used for the reconstruction. From the arrangement of segments shown in Fig. 3.3 the azimuthal position of a cell is extracted as ϕ_i, with the multiplicity in each cell as weight w_i.

The raw event plane distributions (before any corrections are applied) for the V0A and V0C separately are shown in Fig. 5.1. Due to the non-uniform acceptance of the detectors, the particles are not isotropically distributed in azimuth. Therefore, also the measured event plane is not evenly distributed among all the angles. Since there is no preferred orientation of the nucleus-nucleus collision, the distribution of event plane an-

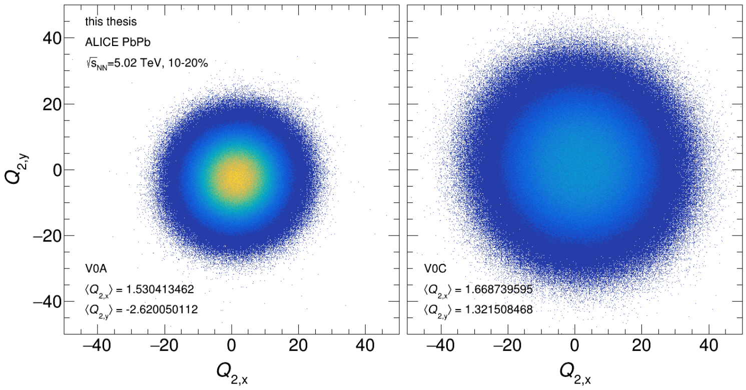

Figure 5.2: Distribution of the Q_2 vectors in the positive (left) and negative (right) pseudorapidity range.

gles should be flat. Therefore, the event plane has to be corrected before it can be used. The first correction is the recentering of the Q_n vectors. The distribution of second order event flow vectors for one centrality bin is depicted in Fig. 5.2. The distributions for the other centrality bins can be found in appendix A.2. For the correction the average values of Q_x, Q_y are determined over all events and then subtracted. The resulting distributions for V0A and V0C are shown in Fig. 5.3. As can be seen, the resulting distributions are more isotropic than before, but still not to the desired level. Before a second correction step is applied, V0A and V0C are combined to a total V0 event plane.

To combine V0A/C for a total event plane, the Q_n vectors are added up before Ψ_2 is calculated [62]:

$$Q_{n,i,\mathrm{V0}} = \chi^2_{n,\mathrm{V0A}} Q_{n,i,\mathrm{V0A}} + \chi^2_{n,\mathrm{V0C}} Q_{n,i,\mathrm{V0C}}, \tag{5.4}$$

where the χ_n [63] are weighting coefficients that are calculated using the event plane resolution (see Sec. 5.1.1 for more details). The resulting combined V0 event plane angle distribution is as well displayed in Fig. 5.3. On this distribution, the second correction step is applied.

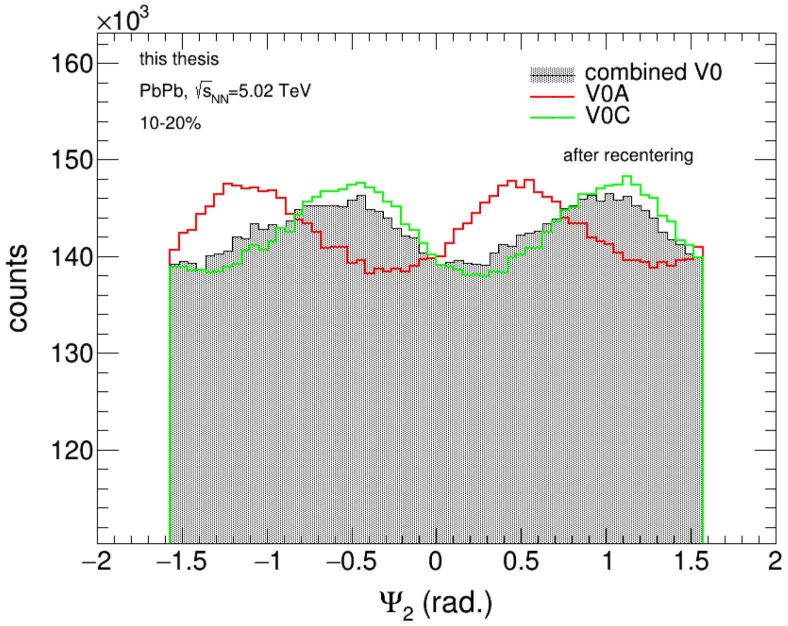

Figure 5.3: Ψ_2 distribution after the recentering correction for the V0A, V0C and combined V0 detector.

The distribution of event plane angles can be described by a Fourier expansion. To flatten the event plane, a shift correction is applied, where the coefficients of the Fourier expansion are used to determine the magnitude of the shift. The shift is calculated as [63]

$$n\Delta\Psi_n = \sum_{i=1}^{i_{max}} \frac{2}{i}(-\langle\sin(in\Psi_n)\rangle\cos(in\Psi_n) + \langle\cos(in\Psi_n)\rangle\sin(in\Psi_n)), \tag{5.5}$$

where the coefficients $\langle\sin(in\Psi_n)\rangle$ and $\langle\cos(in\Psi_n)\rangle$ are calculated as an average over events in a first iteration. The event plane distribution is then flattened by adding $\Delta\Psi_n$ as a correction to each event plane angle:

$$\Psi_2' = \Psi_2 + \Delta\Psi_2 \tag{5.6}$$

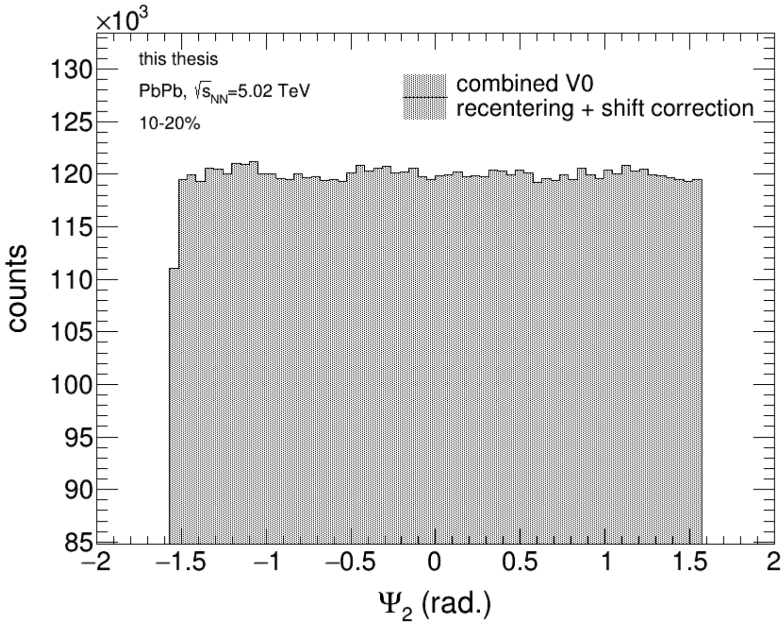

Figure 5.4: Ψ_2 distribution for the combined V0 detector after recentering and shift correction.

The result of this correction is displayed in Fig. 5.4. The raw event plane distributions, as well as the distributions after each correction step, for all centralities are shown in appendix A.2.

5.1.1 Event plane resolution

Due to finite multiplicity in the events, the event plane cannot be reconstructed perfectly but will deviate from the true symmetry plane of the collision [62]. The event plane resolution is a measure of how well the event plane can be reconstructed and is defined as

$$\mathcal{R} = \langle \cos(n[\Psi_{EP,n} - \Psi_n]) \rangle, \tag{5.7}$$

where n is the order of the event plane. However, as already discussed in Ch. 1 the true Ψ_n is not available to be measured experimentally. Therefore, $\mathcal{R}$ has to be approximated by using multiple sub-events [62, 63]:

$$\mathcal{R}_n^a = \left\langle \cos(n[\Psi_{EP,n}^a - \Psi_n]) \right\rangle \tag{5.8}$$

$$= \sqrt{\frac{\left\langle \cos(n[\Psi_{EP,n}^a - \Psi_{EP,n}^b]) \right\rangle \left\langle \cos(n[\Psi_{EP,n}^a - \Psi_{EP,n}^c]) \right\rangle}{\left\langle \cos(n[\Psi_{EP,n}^b - \Psi_{EP,n}^c]) \right\rangle}} \tag{5.9}$$

a, b and c denote the different sub-events. To determine the resolution for the V0A event plane for example, the sub-events b = V0C and c = TPC are used. The TPC event plane is reconstructed using the same Q_n vectors as before, and using the azimuthal angle and the track p_{T} as weights. The event plane resolution for V0A and V0C are shown in Fig. 5.5. Since the event plane angles in V0A and V0C are not further flattened individually, these are the event plane resolutions after the recentering step. They are used to combine the two arrays for the combined V0 event plane angle in Eq. 5.4. The event plane resolution for the combined V0 after all corrections is as well displayed in Fig. 5.5.

5.2 JET RECONSTRUCTION

With the event plane being reconstructed, the next important step are the jets. They are the trigger object with respect to which each correlation function is built.

To get the jet axis, i.e. φ and η of the jet, first the jets have to be reconstructed. In addition to the requirement that the algorithm reliably reconstructs jets in the event, it also has to be infrared and collinear safe. This means that the addition of a soft particle ($p_{\mathrm{T}} \to 0$) or the splitting of a parton cannot change the properties of the reconstruced jets. Two algorithms that fulfill these requirements and are most commonly used in the evaluation of high energy hadronic collisions are the anti-k_{T} [23] and k_{T} [64] algorithms.

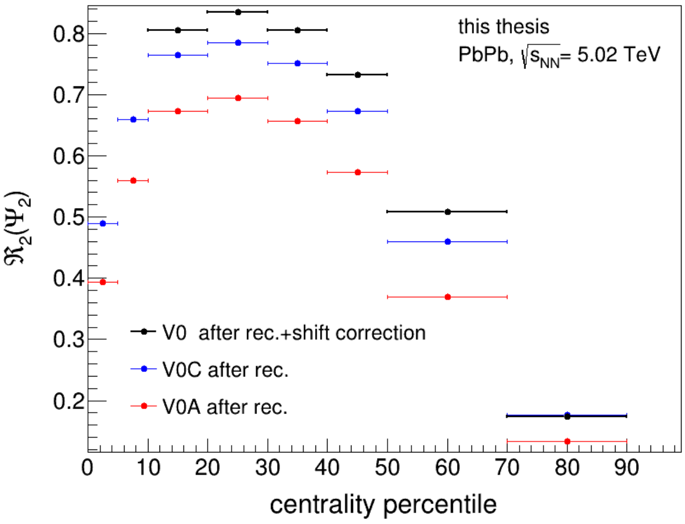

Figure 5.5: Event plane resolution for the V0A and V0C in the different centrality bins.

The algorithms use a distance measure calculated between all particle pairs (i, j) in the event. For anti-k_T

$$d_{ij} = \min\left(1/p_{ti}^2, 1/p_{tj}^2\right)\frac{\Delta_{ij}^2}{R^2} \tag{5.10}$$

$$d_{iB} = 1/p_{ti}^2 \tag{5.11}$$

and for k_T

$$d_{ij} = \min\left(p_{ti}^2, p_{tj}^2\right)\frac{\Delta_{ij}^2}{R^2} \tag{5.12}$$

$$d_{iB} = p_{ti}^2 \tag{5.13}$$

with $\Delta_{ij}^2 = (y_i - y_j)^2 + (\varphi_i - \varphi_j)^2$, where p_i, φ_i, y_i are the transverse momentum, azimuthal angle and rapidity of the particle, although in practice for the latter mostly η is used. d_{iB} represents the distance of the particle to the beam (z direction). R is called

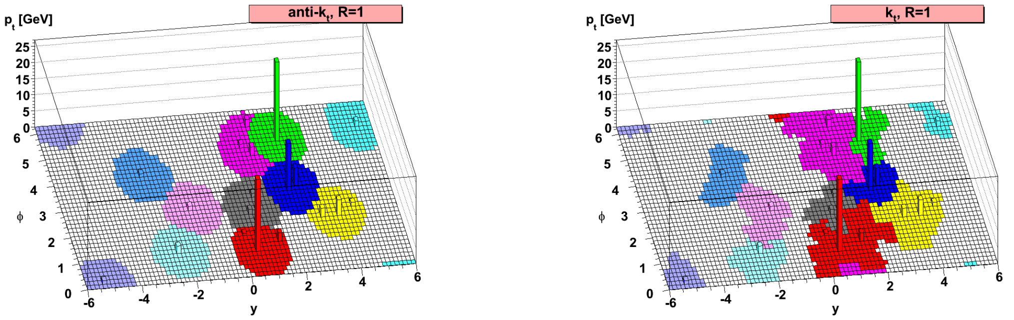

Figure 5.6: Illustration of the area of reconstructed jets clusteres with the anti-k_T (left) and k_T (right) algorithms. Fig. taken from [23].

the jet radius. The radius is chosen in each measurement or calculation as part of the jet definition. In the sequence, particles are clustered together that satisfy $d_{ij} < d_{iB}$ to form a new object added to the list. When no more entries can be merged, the algorithm converges.

The behavior of both algorithms can be seen in Fig. 5.6. Due to the inverse dependence on the transverse momentum, in anti-k_T the distance measure is dominated by hard particles. For similarly spatially separated particles, d_{ij} will be much smaller for a hard particle paired with a soft particle than for two soft particles. Therefore, soft particles will cluster with a hard particle before they cluster among themselves, leading to perfectly conical jets for the hardest particles. In case of a high particle density, the available area is distributed among the jets due to a momentum hierarchy. In contrast, the k_T algorithm leads to more variable jet areas. It is much more sensitive to soft particles in the clustering.

In analyses, anti-k_T reconstructed objects are used for the jet properties, while k_T is used to get a measure for the background energy density that the jets sit on top of. FastJet [65, 66] is a software package that implements those two and also other clustering algorithms and is used in this thesis.

5.2.1 JET SELECTION AND BACKGROUND ENERGY CORRECTION

The jets are reconstructed from TPC hybrid tracks, the track selection is described in section 4.3. All tracks that pass the track selection get fed into FastJet and reconstructed with the anti-k_T algorithm. The jets from this collection will be called "SE jets" (as in jets reconstructed from particles from the same event) in the following. On the resulting collection of jets, a series of fiducial cuts was applied to ensure full acceptance and minimize background contributions. A jet radius of $R = 0.2$ was chosen, resulting in an pseudorapidity acceptance of $|\eta| < \eta_\text{tracks} - R = 0.7$ for the jets. The azimuthal axis of each jet is used to calculate the orientation of the jet with respect to the event plane. The relative angle

$$\Delta\phi_\mathrm{EP} = \phi_\text{jet} - \Psi_2 \tag{5.14}$$

can take on values between 0 and 2π. However, as becomes clear from Fig. 2.6, the path-length of the jet through the medium is the same in the same colored regions. Therefore, the different bins for relative orientation are combined and result in the bins used in this thesis:

- in-plane: $0 \leq |\Delta\phi_\mathrm{EP}| < \pi/6$
- mid-plane: $\pi/6 \leq |\Delta\phi_\mathrm{EP}| < \pi/3$
- out-of-plane: $\pi/3 \leq |\Delta\phi_\mathrm{EP}| \leq \pi/2$

While the general track p_T has a lower cutoff of 0.15 GeV/c, an additional leading track cut was applied to the jets. That means that only jets with a leading constituent track with p_T >5 GeV/c are selected for further analysis.

Since the collection of particles used to reconstruct the jets does not only consist of the jet particles, but also particles from the underlying event, the reconstructed jet energy varies from the true one. Depending on their area A, jets accumulate different amounts of background particles. It is impossible to distinguish jet particles from background particles, but the contribution can be subtracted by using information of the event's energy density. The average energy density is defined as

$$\langle\rho\rangle = \text{median}\left\{\frac{p_{Ti}}{A_i}\right\} \quad (k_T \text{ jets}), \tag{5.15}$$

the median over all k_T jets i, where p_Ti and A_i are the transverse momentum and area of the ith jet, respectively. The raw jet momentum of the anti-k_T jets is then corrected by subtracting this average background energy density, scaled with the area of the jet:

$$p_T^{\text{jet}} = p_T^{\text{raw}} - \langle\rho\rangle \times A_{\text{jet}} \tag{5.16}$$

Since the particles of the underlying event are modulated by flow, introduced in section 1.3, the background energy density is as well. Accordingly, by using the average energy density for every jet, regardless of its orientation in the event, $\langle\rho\rangle$ will underestimate the contribution to jet energies in regions with maximum v_n and overestimate it in regions with minimum v_n. This will result, for the same jet momentum, in an amplified difference in jet yield for the different $\Delta\phi_\mathrm{EP}$ which is not signal but only introduced by the background. To circumvent this, instead the local energy density is used [62]. For this, the particles of the event that lie outside of the leading jets region and have p_T smaller than 5 GeV/c are filled into a histogram. The entries are binned by the track's azimuthal angles and weighted with the particles p_T . The distribution is then fitted with the Fourier expansion

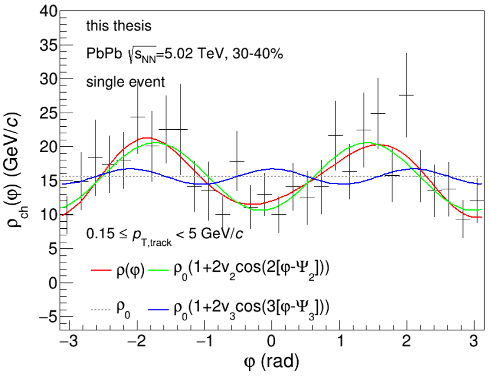

Figure 5.7: Example from a single of the φ dependent background energy density. The complete fit for $\rho(\varphi)$ is depicted in red, the different harmonics in other colours.

$$\rho(\varphi) = \rho_0 \times \left(1 + 2\left\{v_2^{\text{obs}} \cos(2[\varphi - \Psi_2]) + v_3^{\text{obs}} \cos(3[\varphi - \Psi_3])\right\}\right) \tag{5.17}$$

Ψ_2 and Φ_3 are the event plane angles of second and third order respectively, measured with the V0 detector. v_2^{obs} and v_3^{obs} are free fit parameters and are the flow contributions of the background. It is assumed that higher order harmonics can be neglected for the fit. ρ_0 is a normalization parameter. Its initial value is set the to $\langle\rho\rangle$, but it is left as a free parameter. An example for an events background energy density distribution is shown in Fig. 5.7. The fit function, as well as the split into the different harmonics are depicted also.

Since there exist events where only few particles pass the track cut criteria, two quality assurances are checked before the fit result is used to subtract the background energy. First, the fit has to return a valid fit result. Second, the global minimum of the fit function has to be equal or larger than zero, to exclude unphysical cases of negative background energy density. In case either of the checks fail, the average energy density $\langle\rho\rangle$ (Eq. 5.15) is used for the subtraction. When the fit succeeds, the local energy density is calculated by integrating around the jets axis:

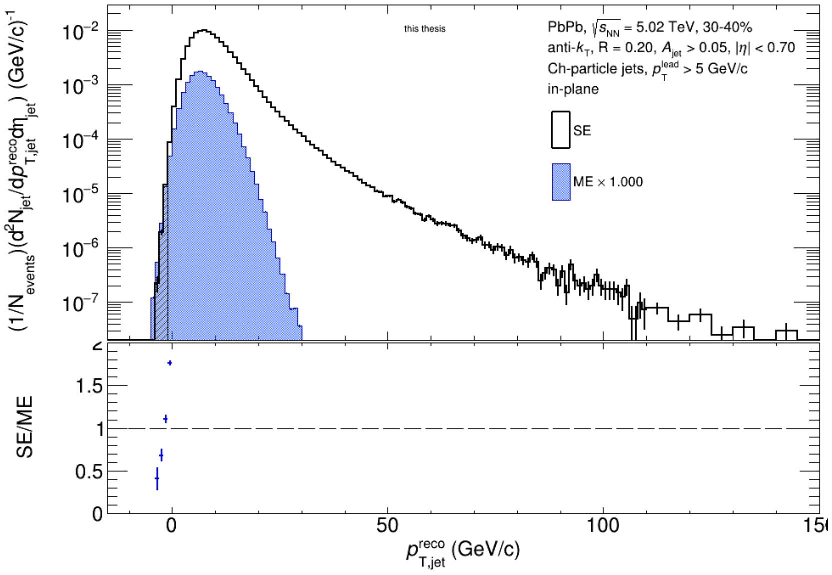

Figure 5.8: SE and ME jet p_T distribution for in-plane jets.

$$\rho_{\text{local}} = \frac{\langle\rho\rangle}{2R\rho_0} \int\limits_{\varphi-R}^{\varphi+R} \rho(\varphi)\,\mathrm{d}\varphi, \tag{5.18}$$

ρ_{local} is then used in eq. 5.16. An example for the background subtracted jet spectrum can be seen in Fig. 5.8 in black. The p_T distributions for all event plane orientations and centrality bins are given in appendix A.3. The construction of the blue distribution, which is a measure for the uncorrelated background jets, is described in the next section.

5.2.2 Combinatorial jets – Mixed Events

As described in the introductory chapters to this thesis, heavy-ion collisions yield events with a large number of particles. While some of those particles are parts of jets and are correctly reconstructed as such, especially at lower momenta uncorrelated particles of the background will be clustered together to fake jets. Those get picked up in the construction of the correlation functions and skew the signal.

Mixing category	**Number of bins**
multiplicity	10
z-vertex position	6
event plane angle Ψ_2	12
p_{T} sum	4

Table 5.1: Event mixing categories for hadron-hadron mixed events

First employed by STAR [67] and later adapted for ALICE data [55, 68], a mixed event technique is used to remove fake jets on a statistical level. The details and systematic studies of the mixed events can be found in [55]. Here, the most important principles are explained. The mixed event technique described in this section and resulting jets thereof will from here on be termed ME or hadron-hadron mixed events.

The aim of the hadron-hadron mixed events is to artificially create events that resemble real events in terms of acceptance, particle momentum distribution and general quantities like the event plane angle distributions and particle multiplicity as closely as possible, but where any physical correlations between the particles are removed. This is done by first categorizing the real events into bins of the particle multiplicity, z-vertex position, Ψ_2 and the summed p_{T} of all particles in the event. A summary of the categories and the number of bins per category is given in Table 5.1. In a second step, new events are created by randomly selecting tracks from each real event and combining them into a new event. The schematics of this procedure are shown on the left in Fig. 5.9. The number of tracks that is picked for each ME is sampled from the real event multiplicity distributions, shown on the right of Fig. 5.9. The mixing is done in each combination of categories individually, resulting in 2,880 cases. On each ME, the jet reconstruction is performed with the same parameters as in the SE case (Section 5.2). In the mixing, tracks of all p_{T} are included. However, since the aim is to exclude any real-jet-like objects, jets that are reconstructed containing a track with $p_{\mathrm{T,track}} > 10$ GeV/c are excluded from further analysis.

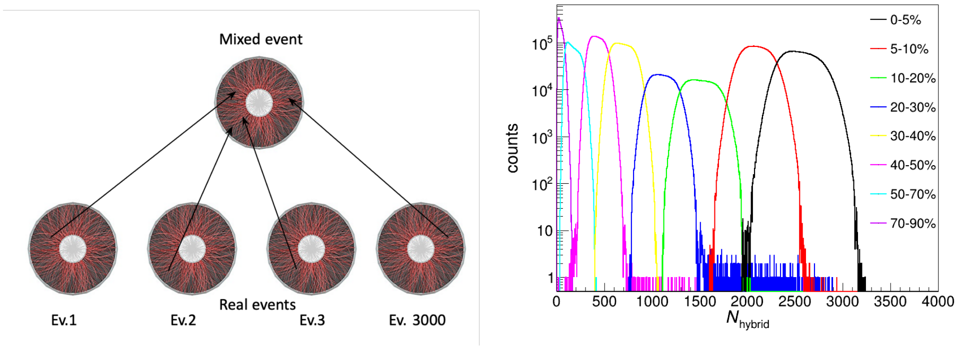

Figure 5.9: Left: Schematic of ME construction [?]. Right: Multiplicity distributions in the different centrality bins.

The $p_{\rm T}$ distribution of the reconstructed ME jets is collected in a similar way to the SE jets. An examplary distribution is shown in Fig. 5.8 in blue. The distributions for other event plane orientations and centralities are shown in appendix A.3.

The fake jet contributions can now be removed from the real jets by subtracting the two spectra (SE-ME). However, to obtain the exact number of ME jets that should be subtracted from the spectrum of SE jets, the $p_{\rm T}$ distribution has to be normalized. First, the spectra are normalized in each combination of categories individually. For this, the $p_{\rm T}$ distributions for SE and ME are integrated, resulting in the number of entries n_{SE} and n_{ME}, respectively. The ME distribution is then scaled by n_{SE}/n_{ME}. After this, the distributions of all categories are added up and normalized by the total number of events.

While the used mixing categories classify the events to a mostly satisfactory level, there are remaining effects that cannot be caught by the procedure. However, due to limited statistics it is not feasible to introduce further mixing categories. Instead, the remaining differences in shape between the SE and ME distribution are absorbed into a scaling factor for the ME distribution. For the determination of the scaling factor, values between 1 and 1.2, corresponding to a width scaling of 20 %, in steps of 0.001 are applied to scale the ME distribution. The best scaling factor is determined with three conditions: First, the χ^2 for the difference of the ratio between SE and ME on the left hand side to unity is minimized.

Second, the ratio in the peak region must not fall below 1, since this would result in a negative number of jets after the ME subtraction, a nonphysical result. And third, since the contribution of fake jets is expected to decrease with increasing jet momentum, the ratio is required to increase monotonously.

As a last step, the ME distribution has to be scaled again to the number of SE. The scaling factor is determined in a region where no real jets are present, namely the left flank of the spectrum. The scaling factor is again calculated by dividing the integrals of the SE and ME distribution, where here the integral is calculated to an upper limit. The upper limit is identified by sufficient statistics, where the relative error of the scaling factor falls below 10 %.

With the reconstructed SE and ME jets, now the jet-hadron correlations can be constructed. The procedure as well as the several corrections are described in the following.

5.3 JET-HADRON CORRELATIONS

In each event, the collection of charged hadrons and the subsequently reconstructed jets are used to construct the correlation functions. For each triggered jet, the angular differences of the jet axis to all particles (the associated particles) are calculated. Therefore, one obtains a 2-dimensional distribution in $\Delta\varphi = \varphi_{\text{jet}} - \varphi_{\text{assoc.}}$ and $\Delta\eta = \eta_{\text{jet}} - \eta_{\text{assoc.}}$, where φ is the azimuthal angle of jet and particles and η is the pseudorapidity.

$$S_{\text{SE}}(\Delta\varphi, \Delta\eta) = \frac{1}{N_{\text{trig,same}}} \left.\frac{\mathrm{d}^2 N}{\mathrm{d}\Delta\varphi \mathrm{d}\Delta\eta}\right|_{\substack{\text{same}\\ \text{event}\\ \text{pairs}}} \equiv \frac{N_{\text{pair,same}}}{N_{\text{trig,same}}} \tag{5.19}$$

S is the per-trigger yield, the number of jet-hadron pairs per trigger jet. An exemplary depiction of the number of same-event pairs in the 2D space can be seen in Fig. 5.10. At

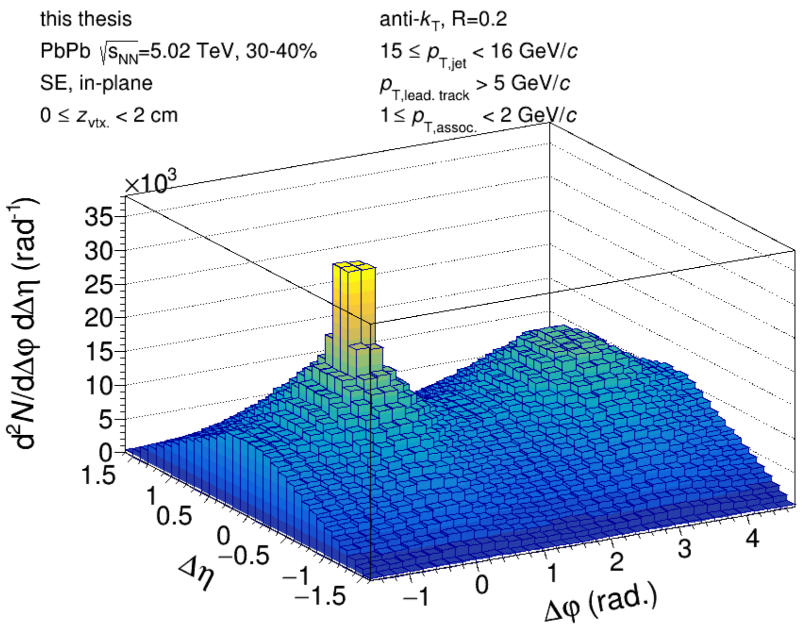

Figure 5.10: An example for $S_{\text{SE}}(\Delta\varphi, \Delta\eta)$ in one z-vertex bin, before the normalization by the number of triggers.

$(\Delta\varphi, \Delta\eta) = (0, 0)$ and $\Delta\varphi = \pi$ the near-side peak and away-side peak (see also chapter 2) can be seen, respectively.

As described in the previous section, the correlations are subdivided according to the orientation of the jet with respect to the event plane, in the following called relative event plane (EP) bins. Furthermore, the correlations are evaluated in bins of the jet momentum $p_{\text{T,jet}}$ and associated particles $p_{\text{T,assoc.}}$.

5.3.1 Pair acceptance and efficiency correction

Since we work with real, limited size detectors, effects of both the acceptance and tracking efficiency will show up in the correlation functions. How well a particle (and subsequently a jet) can be reconstructed, depends on the position (φ,η) and momentum of the particles. With the chosen track cuts (see 4.3), the acceptance and efficiency are uniform in azimuth and will not be specially corrected for in this coordinate. The single-particle tracking efficiency in η and p_{T} , which can also be seen in ch. 4.3 for PbPb and pp collisions, is accounted for by weighting the entries to the correlation functions with the inverse of the efficiency that is extracted for each respective particle's η and p_{T} .

The limited size of the detector in η leads to a different acceptance of the pairs (jet and associated particle), depending on their separation in this coordinate ($\Delta\eta$). If they are close together ($\Delta\eta$ = 0), the probability to detect both of them is high, regardless where in the detector they are actually located. However, the higher their separation is, the higher is the probablity that one lies within the acceptance range of the detector and the other does not. This leads to a triangular shape in $\Delta\eta$ in the correlation function. An example for this shape can be seen in Figure 5.11. Since this shape is not a physical signal but only a detector effect, it has to be corrected for. This is done by removing any physical correlation from the data by mixing jets from one event with associated particles from another event:

$$\Delta\varphi|_{\text{acceptance}} = \varphi_{\text{jet}}^{\text{event 1}} - \varphi_{\text{assoc.}}^{\text{event 2}}, \tag{5.20}$$

$$\Delta\eta|_{\text{acceptance}} = \eta_{\text{jet}}^{\text{event 1}} - \eta_{\text{assoc.}}^{\text{event 2}}, \tag{5.21}$$

$$A(\Delta\varphi, \Delta\eta) = \frac{1}{N_{\text{norm}}} \frac{\mathrm{d}^2 N}{\mathrm{d}\Delta\varphi \mathrm{d}\Delta\eta}\bigg|_{\substack{\text{jet-hadron}\\ \text{mixed event}\\ \text{pairs}}} \equiv \frac{N_{\text{pairs,jet-hadron mix}}}{N_{\text{norm}}}. \tag{5.22}$$

N_{norm} is the value at $A(\Delta\varphi = 0, \Delta\eta = 0)$, since it is expected that the pair acceptance of objects going in the same direction is 1.

In principle every jet can be correlated with every set of tracks from other events. However, due to the structure of the code, that is also setup to prepare the subtraction of fake jets (cf. next section), and the fact that the correlation of all jet-track pairs takes up running time unreasonable for the available resources, a different approach to this was taken. All required information (p_{T} ,η,φ,z-vertex bin and EP angle) of both jets and tracks are saved while looping over all events, and the mixing is performed at the end. Since the data

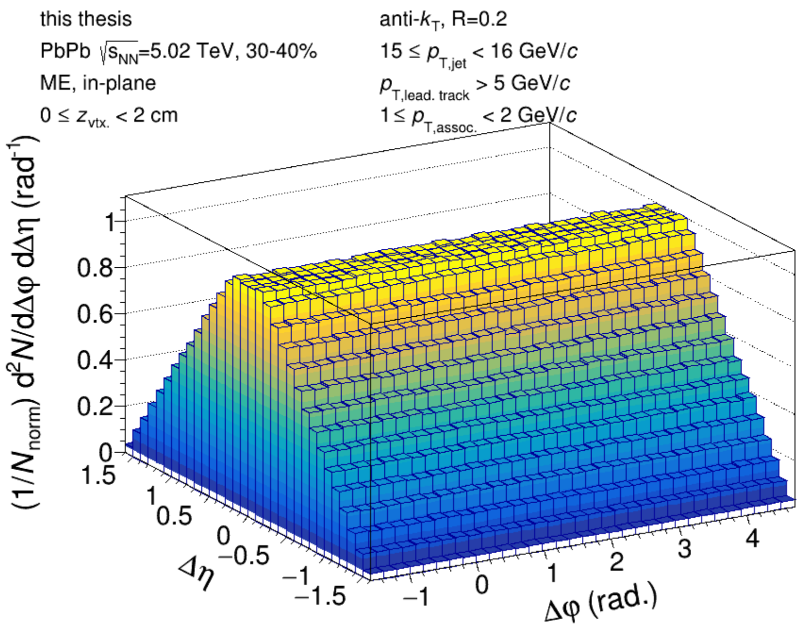

Figure 5.11: Jet-hadron mixed event correlation, normalized to 1 at $(\Delta\varphi, \Delta\eta) = (0, 0)$.

set is divided into bins of the event plane angle, a loop is done for each jet over all event plane bins. In a loop over all jets, for each jet randomly 5 sets of tracks are chosen from the same z-vertex bin to calculated the acceptance correlations. Measures are taken to ensure that a set of particles is not used twice for the same jet.

In order to avoid confusion with the hadron-hadron mixed events introduced in the previous section, the sort of event mixing described here to determine the underlying acceptance distribution, will be called jet-hadron mixed event or acceptance event.

To ensure that the acceptance events used have similar underlying parameters, they are constructed in bins of the z-vertex (2 cm). The signal correlation function is constructed in these bins as well and divided by the acceptance correlation in each bin before the bins are merged. To statistically enhance z-vertex bins with a large number of entries, the correlations are weighted by the number of trigger jets. The formula for this procedure is

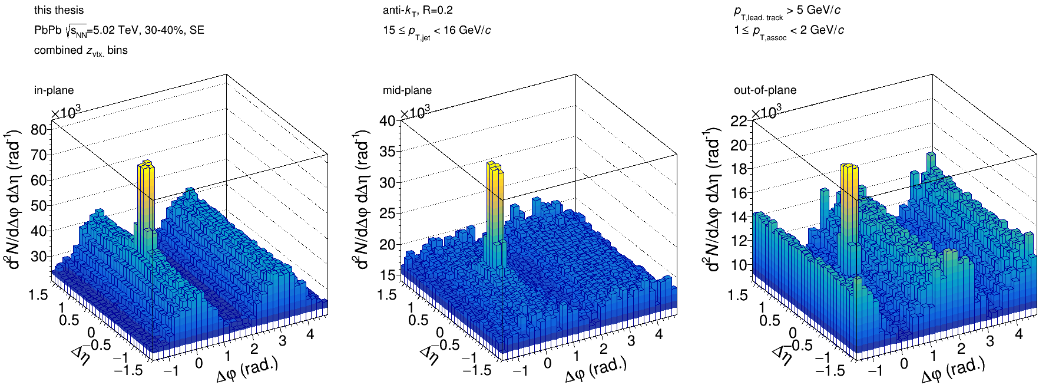

Figure 5.12: SE correlation function after correction for the pair-acceptance and merging of the z-vertex bins in all event plane bins. The number of pairs is not yet normalized y the number of trigger jets.

$$C_{\mathrm{SE}}(\Delta\varphi, \Delta\eta) = \frac{\sum\limits_{z} \left(\frac{S(\Delta\varphi,\Delta\eta)}{A(\Delta\varphi,\Delta\eta)} \right)_i (N_{\mathrm{trig,same}})_i}{\sum\limits_{z} (N_{\mathrm{trig,same}})_i} \tag{5.23}$$

$$= \frac{\sum\limits_{z} \left(\frac{N_{\mathrm{pairs,same}}/N_{\mathrm{trig,same}}}{N_{\mathrm{pairs,jet\text{-}hadron\ mix}}/N_{\mathrm{norm}}} \right)_i (N_{\mathrm{trig,same}})_i}{\sum\limits_{z} (N_{\mathrm{trig,same}})_i} \tag{5.24}$$

$$\equiv \frac{N_{\mathrm{pairs,SE}}}{N_{\mathrm{trig,SE}}} \tag{5.25}$$

where the definitions for $S(\Delta\varphi, \Delta\eta)$ (Eq. 5.19) and $A(\Delta\varphi, \Delta\eta)$ (Eq. 5.20) are used. An example for $C_{\mathrm{SE}}(\Delta\varphi, \Delta\eta)$, the correlation function after it has been corrected for the pair-acceptance and subsequent merging of the z-vertex bins, is shown in 5.12. When comparing to the uncorrected correlation in Fig. 5.10, it is apparent that the triangular shape has been removed.

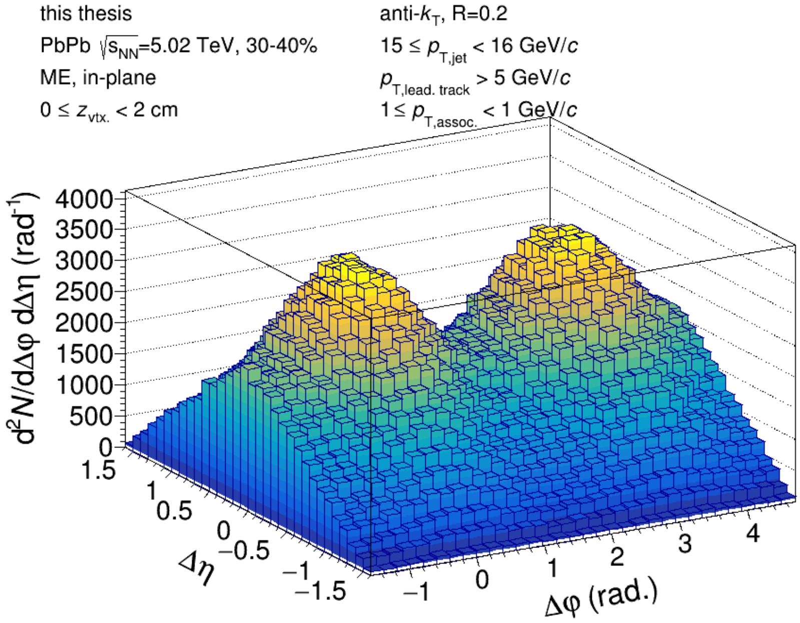

Figure 5.13: Example for uncorrected ME jet correlation function.

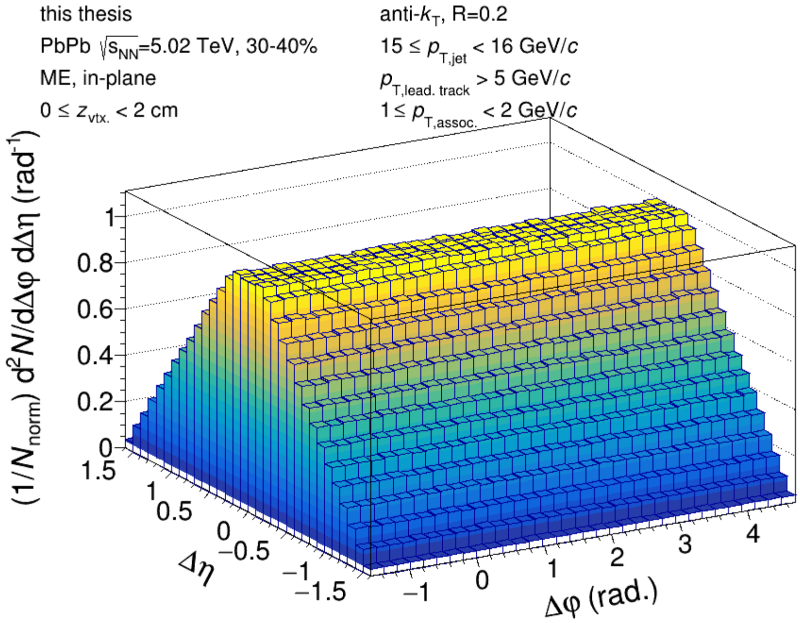

Figure 5.14: Example for ME jet acceptance correlation.

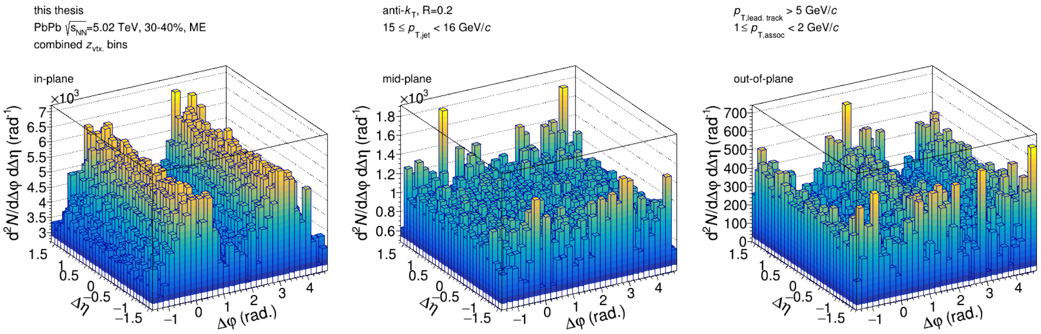

Figure 5.15: ME correlation function after correction for the pair-acceptance and merging of the z-vertex bins in all event plane bins. The number of pairs is not yet normalized y the number of trigger jets.

5.3.2 ME SUBTRACTION

The ME jets, introduced in sec. 5.2.2, are now used to construct ME correlation functions. They are calculated in the same way as the SE correlations: The angular differences between ME jets and SE tracks are calculated, resulting in the correlations shown in Figure 5.13. The SE tracks – all particles from the same event chosen randomly from the collection of real events – are chosen, because while the fake jets themselves are reconstructed from uncorrelated background, the tracks they are correlated with are part of a real event and therefore modulated by flow. So the contributions of fake jets in the SE correlation functions also show up with this flow component and thus it has to be recreated in the ME correlation functions. Those correlations as well are corrected for tracking efficiency and pair-acceptance. For the acceptance distributions, ME jets are correlated with ME tracks. In order to avoid any sort of self correlation between tracks and reconstructed jets from ME, half of the ME are used to reconstruct the fake jets, and the other half is used to serve as associated particles for the acceptance events. The resulting acceptance correlation for the ME can be seen in Figure 5.14. Like in the SE case, the ME correlations in z-vertex bins are merged before performing SE-ME. The result can be seen in Fig. 5.15.

For the derivations down below, the merged ME correlations are termed

$$C_{\mathrm{ME}}(\Delta\varphi, \Delta\eta) = \frac{N_{\text{pairs,ME}}}{N_{\text{trig,ME}}}. \tag{5.26}$$

Now, the scaling and subtraction of ME from SE are explained. As mentioned before, the SE correlations contain contributions from both real and fake jets:

$$N_{\text{pairs,SE}} = N_{\text{pairs,real}} + N_{\text{pairs,fake}} \tag{5.27}$$

$$N_{\text{trig,SE}} = N_{\text{trig,real}} + N_{\text{trig,fake}}. \tag{5.28}$$

In the end, only the correlations from real jets are interesting, so the contributions from fake jets have to be removed. In this analysis this is done by modeling the fake jet contributions with the ME jets. From the p_{T} distributions of SE and ME jets, the ratio

$$r = \frac{N_{\text{trig,fake}}}{N_{\text{trig,SE}}} \tag{5.29}$$

can be extracted. With this, the per-trigger yield from ME correlations can be scaled to the level that would be expected from fake jets for the present number of SE yields:

$$N_{\text{pairs,fake}} = N_{\text{trig,fake}} \frac{N_{\text{pairs,ME}}}{N_{\text{trig,ME}}} = r \frac{N_{\text{trig,SE}}}{N_{\text{trig,ME}}} N_{\text{pairs,ME}} \tag{5.30}$$

From Eq. 5.27:

$$N_{\text{pairs,real}} = N_{\text{pairs,SE}} - N_{\text{pairs,fake}} = N_{\text{pairs,SE}} - r \frac{N_{\text{trig,SE}}}{N_{\text{trig,ME}}} N_{\text{pairs,ME}} \tag{5.31}$$

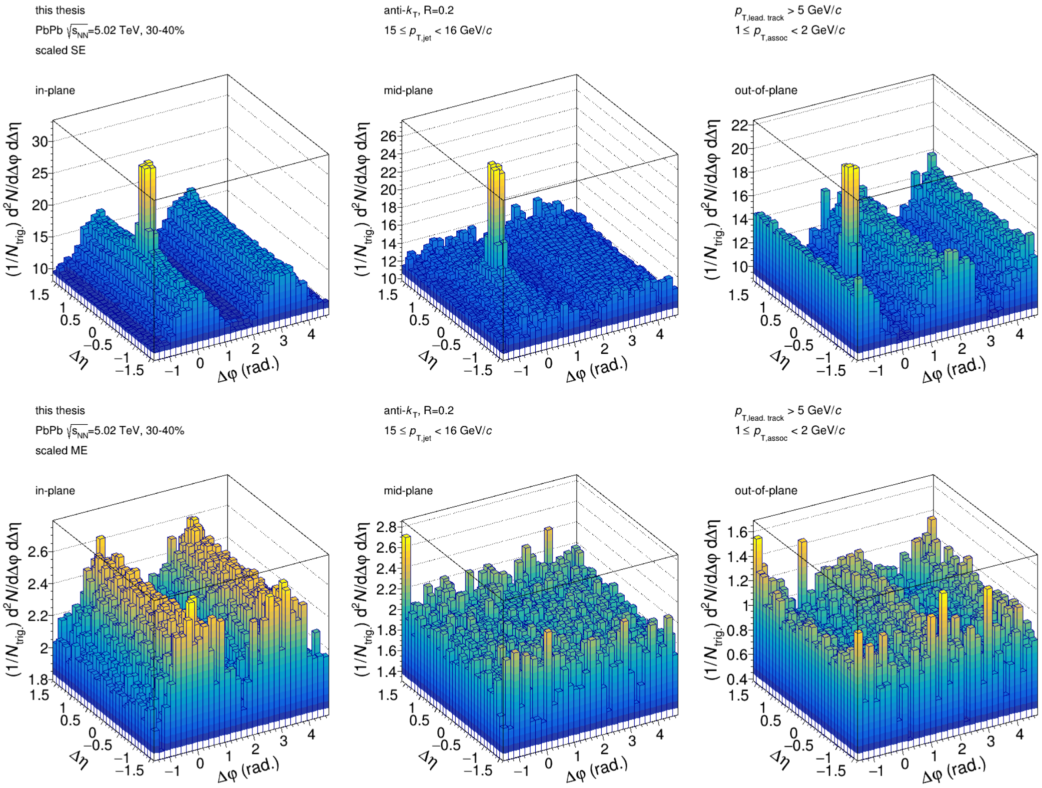

Figure 5.16: Top row: SE jet correlations, scaled according to Equation 5.33 in the jet p_T range $15 < p_{T,jet} < 16$ GeV
Bottom row: ME jet correlations, scaled according to Equation 5.33 in the jet p_T range $15 < p_{T,jet} < 16$ GeV

To get the desired per-trigger yield for real jets, Eq. 5.31 has to divided by the number of real jets $N_{\text{trig,real}} = (1 - r)N_{\text{trig,SE}}$:

$$C(\Delta\varphi, \Delta\eta) = \frac{N_{\text{pairs,real}}}{N_{\text{trig,real}}} = \frac{N_{\text{pairs,SE}} - r\frac{N_{\text{trig,SE}}}{N_{\text{trig,ME}}} N_{\text{pairs,ME}}}{(1-r)N_{\text{trig,SE}}} \tag{5.32}$$

$$= \frac{1}{(1-r)N_{\text{trig,SE}}} N_{\text{pairs,SE}} - \frac{r}{(1-r)N_{\text{trig,ME}}} N_{\text{pairs,ME}} \tag{5.33}$$

The scaled SE and ME correlations for a selected p_T bin, as well as the final corrected correlation function in the same p_T bin, are depicted in Figures 5.16 and 5.17.

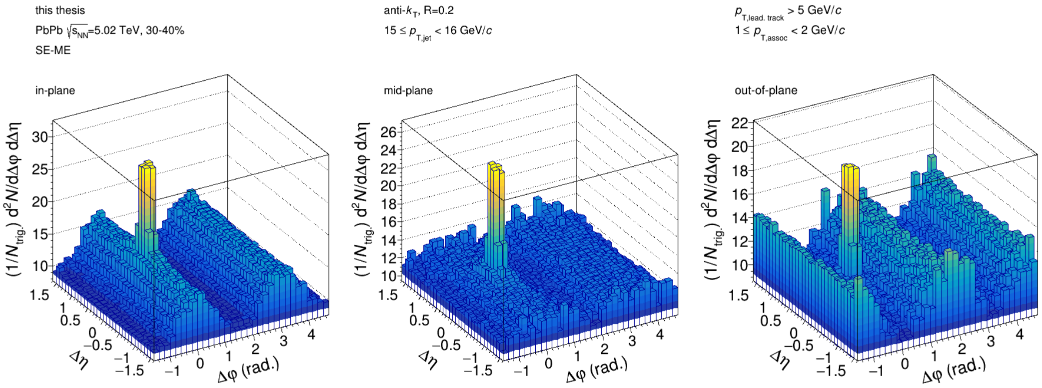

Figure 5.17: SE-ME correlation in the jet p_T range $15 < p_\mathrm{T,jet} < 16$ GeV

5.3.3 Correlated background subtraction

After correcting for the background contributions consisting of the detector pair acceptance and fake jets, the correlations still contain correlated background. This stems from particles of the bulk of the collision that lie within the selected associated p_T range and therefore add contributions to the correlation function.

Since these contributions are not part of the signal that is the aim of this analysis, they have to be removed. This can be done utilizing both the structure of the correlation function and the shape of the background. An example for correlation functions before the background subtraction is performed can be seen in Fig. 5.18. As has been described in Section 2.3, on the near-side the jet forms a (narrow) peak around $\Delta\varphi = 0$ and $\Delta\eta = 0$. Therefore, entries at large $|\Delta\eta|$ are not part of the jet peak and consist only of background contributions. In the distribution along $\Delta\varphi$, the shape of the background is visible. The particle distribution of the bulk in φ is modulated by the pressure gradients in the collision region, as has been explained in Ch. 1. This translates to a modulation of the distribution of particles when calculating their relative position to the trigger jet. The combination of these information can now be used to subtract the background.

First, the 2D correlations are projected onto $\Delta\varphi$ for $0.8 < |\Delta\eta| < 1.4$. The lower bound is chosen to safely exclude the signal peak, the upper bound to exclude bins with

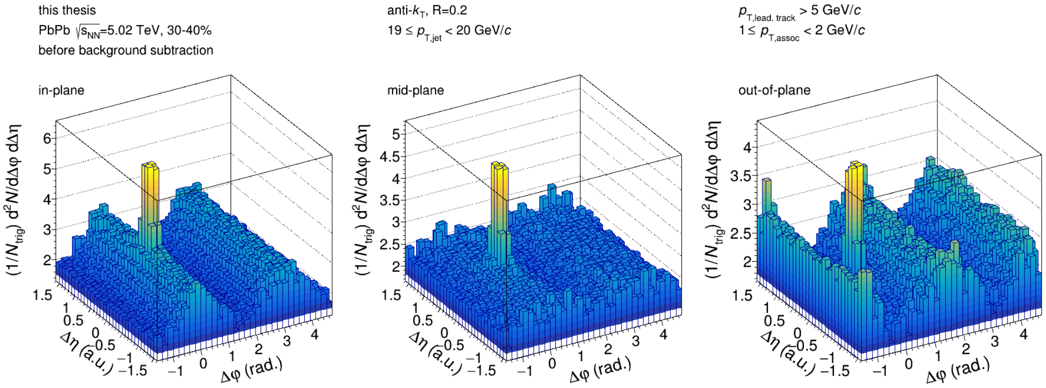

Figure 5.18: Examples for correlation functions in-plane, mid-plane and out-of-plane, in one jet p_T , assoc. p_T and centrality bin. The background subtraction is performed as an example on these correlations.

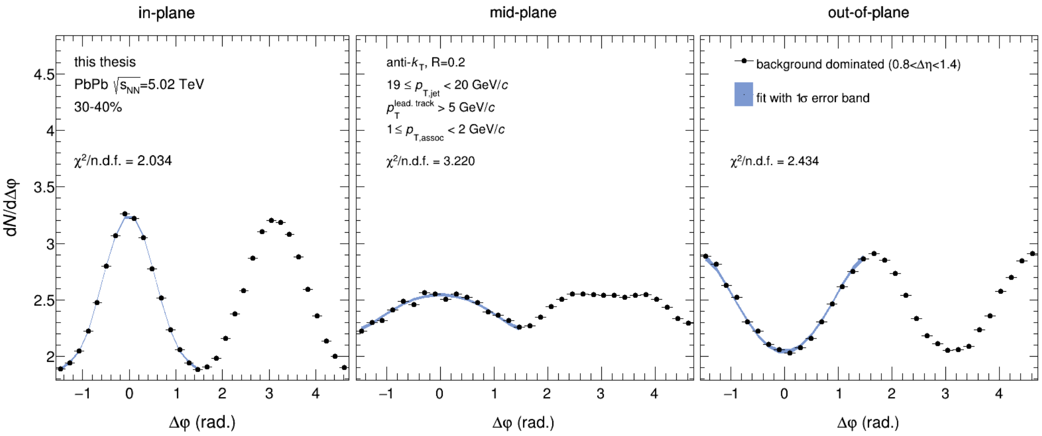

Figure 5.19: Projection of 2D correlation functions onto the $\Delta\varphi$ axis including fits to the distributions

a low number of entries and therefore higher statistical fluctuations. The projection for the same exemplary bins as in Fig. 5.18 can be seen in Fig. 5.19. For the shape of the background, the background level is decomposed into Fourier components, similar to Eq. 1.2:

$$b(\Delta\varphi) = B(1 + \sum_{n=1}^{\infty} 2v_n \cos(n\Delta\varphi)). \tag{5.34}$$

Theoretically, one can fit $b(\Delta\varphi)$ to all different event plane orientations simultaneously, using the information of effective flow coefficients in each bin as constraint on the fit. This is called the Reaction Plane Fit (RPF) method, [69, 70]. The application of this method for this analysis has been tested, but unfortunately did not provide stable results across the needed range in centrality and jet p_{T} . Therefore, Eq. 5.34 is fit individually to each relative event plane bin. Since the away-side peak is extended in $\Delta\eta$, the background fit is only performed on the near-side $\Delta\varphi < \pi/2$. Fitting up to order $n = 3$ provided stable and satisfactory fit results for the majority of jet p_{T} bins. In the cases where this failed, due to a too low number of data points to be fit, the order was reduced to $n = 2$. This then resulted in sufficient background fits for all bins. An example for the fit result is depicted in Fig. 5.19 as blue band.

For the background removal, the fit function is extrapolated to the away-side ($\Delta\varphi > \pi/2$) and $b(\Delta\varphi)$ is subtracted for all $\Delta\eta$ bins. The result of the background subtraction for the chosen example bin can be seen in Fig. 5.20. Other examples for the background fits for different centralities, jet p_{T} and associated p_{T} are shown in App. A.4. Since for increasing jet p_{T} the number of measured jets decreases, the statistical fluctuations and therefore statistical uncertainties of the background fits increase with increasing jet p_{T} . This is combined with increasing statistical uncertainties on the fit for increasing associated p_{T} .

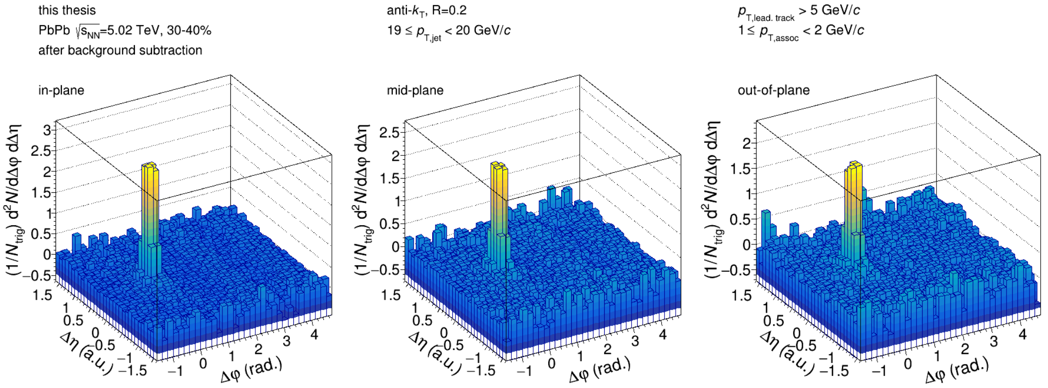

Figure 5.20: 2D correlations after the background subtraction

5.3.4 Correlations in pp

The correlation functions for pp collisions are created similar to the correlations in PbPb: The tracks that pass the tracks cuts enter into the jet reconstruction, with the same parameters as for PbPb. However, since no QGP is created and the multiplicity is much lower in pp collisions, the further processing is simpler.

Due to the lower multiplicity, the contribution from fake jets is assumed to be minimal in pp collisions. Therefore, no ME subtraction is done in this case. Furthermore, since no QGP is created, the background particles do not exhibit the flow modulation present in PbPb collisions. Accordingly, the background level of the correlation functions is not subtracted with a fit of a Fourier expansion, but instead by simply averaging the long range ($1.1 < |\Delta\eta| < 1.5$) region on the near-side ($|\Delta\varphi| < \pi/2$) and subtracting this value from the whole correlation function.

Before the correlations in PbPb collisions can be compared to the correlations in pp, it has to be assured that the underlying jet selection is the same. For this, the jet spectra are unfolded and the correlations re-weighted. The procedure is described in detail in the next section.

5.4 UNFOLDING

The jets that are reconstructed from the remnants of a hadronic collision suffer from a distortion of their momentum due to background particles and a limited detector resolution, that cannot be removed completely by subtracting the average background density. In addition, the background fluctuates significantly. This leads to different jet selections in pp and PbPb, a certain jet momentum selected in pp does not necessarily stem from the same original parton energy as the same momentum selection in PbPb collisions. However, since a quantitative comparison between the two is the goal of this thesis, it has to be assured that the original jet energies are matched between the two systems. In practice, this is done with an unfolding procedure.

The deconvolution of the original signal from detector effects and background is a complicated task, since it requires precise knowledge of the effects and is sensitive to statistical fluctuations [71]. In a discretized space, one can formulate the problem as

$$d_i = \sum_j T_{ij} \theta_j, \tag{5.35}$$

where d_i and θ_j are the measured and true distribution of data points, respectively. T_{ij}, commonly called the response matrix, is the probability for a true jet j to migrate to the observed bin i and contains the knowledge of effects that smear the datapoints θ_j. The intuitive solution of this equation to obtain the true distribution θ would be to just invert T_{ij}. However, it is not given that the inverse matrix exists. Furthermore, by convoluting the true distribution with smearing effects, information is lost about features in the signal that are smaller than the resolution of those smearing effects. Hence, there is no guarantee for a unique solution to exist. Additionally, due to this, a small statistical fluctuation in the response matrix can lead to large statistical fluctuations in the solution. To mitigate this, additional quality measures need to be put in place, in literature called regularization.

One regularized method to solve the above equation is based on Bayes theorem and consequently called Bayesian unfolding [72, 73]. Bayes theorem for the problem at hand

$$P(C_i|E) = \frac{P(E|C_i)P(C_i)}{\sum\limits_{l=1}^{n_C} P(E|C_l)P(C_l)}, \tag{5.36}$$

describes the probability that the measurement of a jet (effect) E is due to the ith cause, i.e. true data point. This is equal to the normalized probability that an effect is produced by this cause, times the probablity for C_i to occur. When a number of effects $n(E)$ is measured (in the case of this analysis this is the number of entries in each jet p_{T} bin), the expected number of true events can be expressed as

$$\hat{n}(C_i) = \frac{1}{\epsilon_i}\sum_{j=1}^{n_E} n(E_j)P(C_i|E_j) \quad \epsilon_i \neq 0. \tag{5.37}$$

ϵ_i denotes the efficiency with which C_i causes an effect. If $\epsilon_i = 0$, $\hat{n}(C_i) = 0$ since no events are observed to lead back to this cause.

Using Eq. 5.36, Eq. 5.37 can be rewritten in terms of the unfolding matrix M_{ij}:

$$\hat{n}(C_i) = \sum_{j=1}^{n_E} M_{ij} n(E_j) \tag{5.38}$$

$$M_{ij} = \frac{P(E_j|C_i)P_0(C_i)}{[\sum_{l=1}^{n_E} P(E_l|C_i)][\sum_{l=1}^{n_C} P(E_j|C_l)P_0(C_l)]} \tag{5.39}$$

M_{ij} needs two input variables. One is the knowledge of the migration between true and measured data, i.e. the response matrix. How the response matrix is obtained is described in the next section. The second needed input is $P_0(C_i)$, which is called the prior.

This is an educated guess how the true distribution looks like, although also a uniform distribution will lead to a satisfactory result.

In practice, Bayesian unfolding is implemented as an iterative algorithm. This means that the unfolding is performed with the provided response matrix and prior, where first a distribution of true events is migrated to a "measured" one. This is then compared with the actually measured distribution. The starting distribution is modified to reflect the differences between the migrated and measured distribution. For more details cf. section 9.2.2 in [71]. With

$$P(C_i) \equiv P(C_i|n(E)) = \frac{\hat{n}(C_i)}{\hat{N}_{\text{true}}}, \quad \hat{N}_{\text{true}} = \sum_{i=1}^{n_C} \hat{n}(C_i) \tag{5.40}$$

the prior is updated after the first iteration and then used in the next iteration. Since this method relies heavily on the response matrix, statistical fluctuations will cause more pronounced fluctuations in the end result the more iterations are used. As a regularization method, the number of iterations is limited to the point when large fluctuations start to show up in the unfolded distribution.

5.4.1 Unfolding strategy for correlations

The goal of this thesis is to compare the per-trigger yields from correlation functions in PbPb to those in pp collisions. As has been mentioned above, this means that is has to be ensured that the selected jet spectra are comparable. For this purpose, an unfolding technique/re-weighting technique for correlation functions was developed, utilizing the iterative Bayesian unfolding approach described in the previous section. In this section this strategy is explained in detail.

In a first step, the response matrices for all centrality bins are determined. For this PYTHIA pp jets are embedded into PbPb events. The same PYTHIA simulations as in

[55] were used, for details on the production consult this reference. The raw PYTHIA particles are not yet smeared by the detector resolution and represent the "truth" information about the jets. First, a jet reconstruction is performed on the raw PYTHIA particles, resulting in particle level jets. The leading jet is selected and the momenta of its constituents are smeared by the tracking efficiency. This reproduces the detector effects in real events. These smeared tracks are then embedded into a real PbPb event and jet reconstruction is performed on this particle set as well. By embedding the MC tracks into PbPb events, one gains insight into the momentum distortion of jets due to the background particles. The jets from this reconstruction are called hybrid jets. In the next step, a geometrical matching is done between the hybrid and particle level jets to identify the corresponding pair. The momenta of the matched pair are then filled into a 2D histogram. This is the response matrix, which contains information on both the detector effects and the background contributions. An example for the response matrix is depicted in Fig. 5.21, the response matrices for the other centrality bins and event plane orientations are shown in appendix A.5. A majority of the entries lie on the diagonal, meaning that particle level jets and hybrid jets get reconstructed with the same momentum. The diagonal is smeared due to background contributions and the off-diagonal elements are mainly caused by the detector effects.

In the second step of the unfolding procedure, the response matrix is used to unfold the jet p_{T} spectrum. The number of iterations as regularization parameter was chosen to be 5. The prior that is used to in the unfolding according to Eq. 5.38 is the original PYTHIA p_{T} spectrum. However, to account for the shape of the spectrum in PbPb collisions, this distribution is modified with the weight function

$$weight(a,b) = \tanh((x-a)/b), \tag{5.41}$$

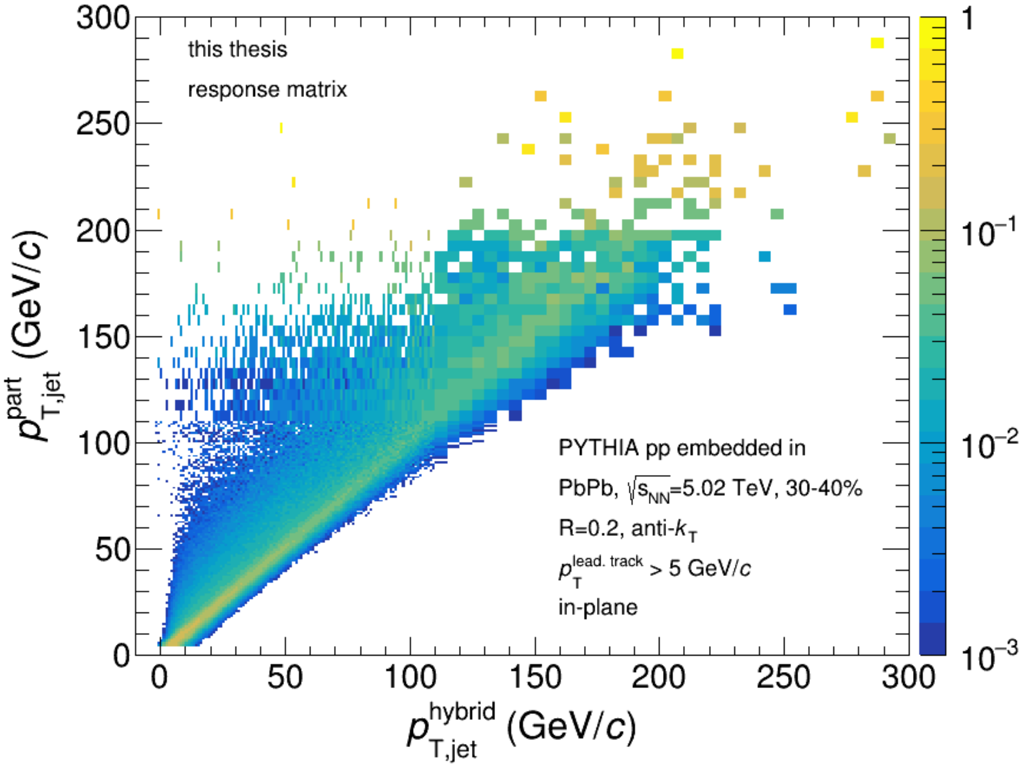

Figure 5.21: Example for the response matrix for 30-40% PbPb collisions: Correspondence between the particle level jet momentum and the reconstructed jet momentum after embedding.

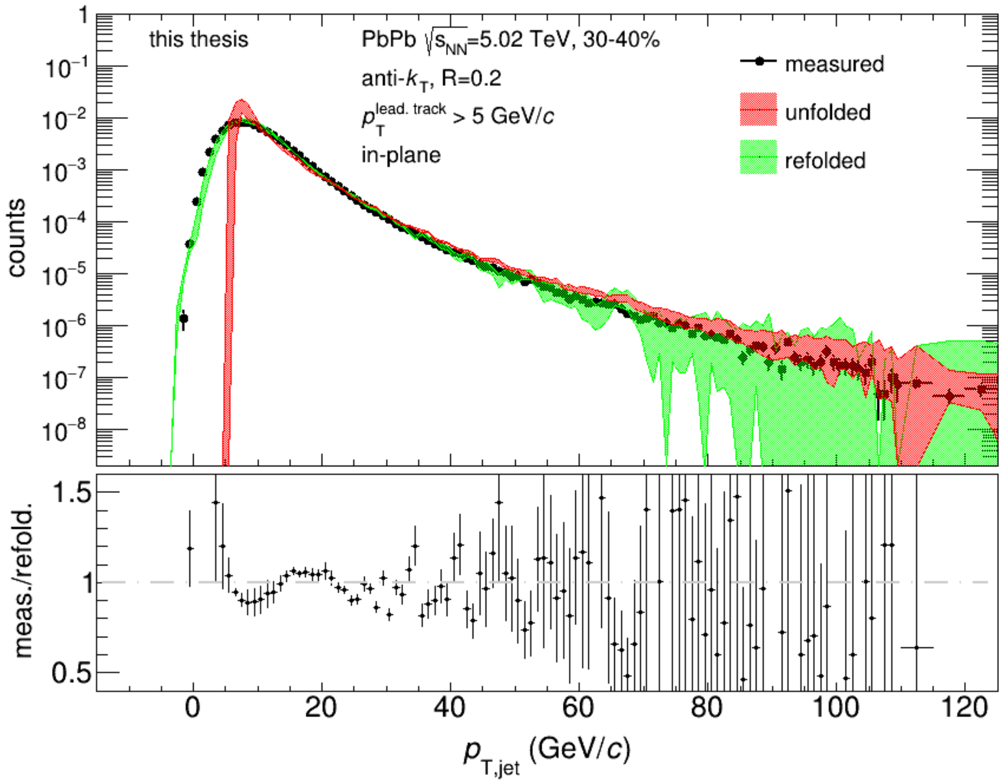

Figure 5.22: The measured jet spectrum (black) and the unfolded spectrum (red) are shown, the scaled PYTHIA p_T spectrum was used as prior. The refolded spectrum is depicted in green.

where the parameters a and b are varied between $a = \{3, 3.5, 4, 4.5, 5, 5.5, 6\}$ and $b = \{5, 6, 7\}$. For the unfolding results, all parameter variations are combined into a mean value and a RMS. The measured spectrum as well as the unfolding result for the centrality bin 30-40%, in-plane, is shown in Fig. 5.22. The spectra for the other centrality bins and event plane orientations are shown in appendix A.5. To obtain a measure how well the unfolding works, the unfolded spectrum is propagated backwards through the response matrix. This refolded distribution (depicted in green in Fig. 5.22) is compared to the measured distribution in the lower panel. While statistical fluctuations are present, the ratio starts to fluctuate around 1 for jet p_T > 15 GeV, indicating the unfolding works well for this region.

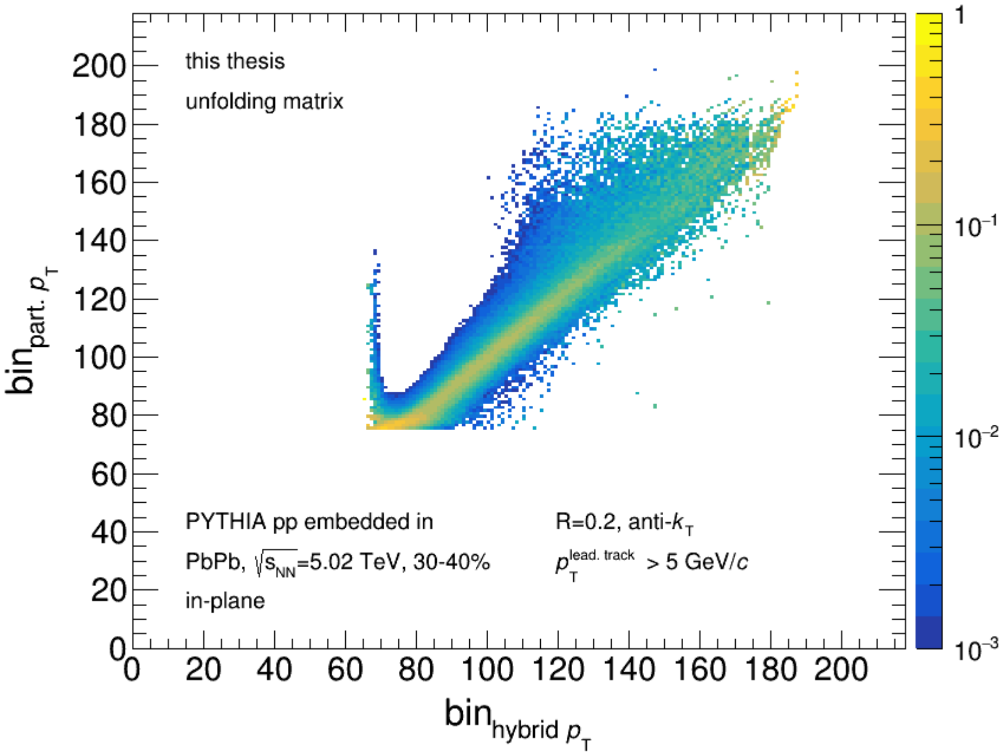

Figure 5.23: Unfolding matrix obtained from the unfolding procedure using Bayesian unfolding

From this unfolding procedure one can obtain the unfolding matrix, which is the iteratively updated response matrix. Similar to the jet spectrum, the single entries of the unfolding matrix are calculated as mean and RMS over the different parameter combinations for the prior weight function. The corresponding unfolding matrix for the response matrix in Fig. 5.21 is shown in Fig. 5.23. The x and y axes of this distribution show the bin number in hybrid p_T and particle level p_T , respectively. The histogram for the measured jet momentum starts at −70 GeV/c and goes up to 300 GeV/c. So bin 71 corresponds to a jet pT of 0 GeV. One can clearly see the diagonal contribution in the unfolding matrix, including the smearing effects. The band around $\text{bin}_{\text{hybrid}-pT} = 65$ and extended in the y direction is likely a remnant of the ME subtraction on the left-hand side of the jet p_T spectrum.

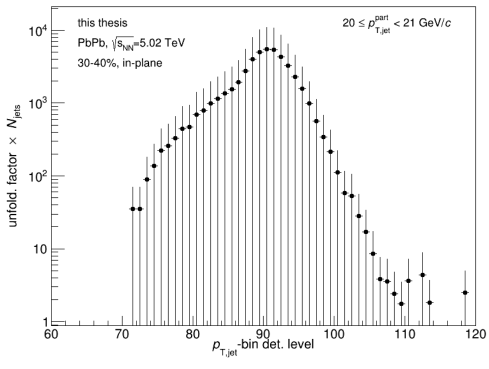

Figure 5.24: Factor from unfolding matrix times the number of trigger jets in each bin in hybrid p_T that are used as an input for a particle level p_T bin $20 \leq p_\mathrm{T}^{\mathrm{part}}$ <21 GeV/c

In the next step, the correlation functions are re-weighted. The procedure is based on the assumption that the distortion of the jet due to background particles and the limited detector resolution affects the jet energy and momentum, but not the direction (φ and η). Then, when the correlations as function of the jet's momentum are re-weighted according to the unfolding matrix, only the jet momentum contribution gets reweighted and conserving the per-trigger yield per jet momentum. The re-weighting is done as follows:

For each bin in jet $_\mathrm{T}$, a correlation function has been calculated, summed over the z_{vtx} bins and normalized by the number of trigger jets in this p_T bin. For each bin in measured ("hybrid") jet p_T , the unfolding matrix entry for each particle level p_T bin is retrieved. To ensure the correct input shape for the correlations, the number of trigger jets per p_T bin provides an additional factor. As an example, the unfolding factor times the number of trigger jets in each bin in hybrid p_T that serve as input for the particle level p_T bin $20 \leq p_\mathrm{T}^{\mathrm{part}}$ <21 GeV/c is shown in 5.24.

The entries of the measured correlation functions are now migrated to the particle level p_T bins using the described factor. Afterwards, the correlation in each particle level bin is re-normalized by the number of trigger jets in that bin. The resulting correlation function for the example in the particle level p_T bin $20 \leq p_\mathrm{T}^{\mathrm{part}}$ <21 GeV/c is shown in Fig. 5.25. The measured correlations, which have the highest weighting factor according

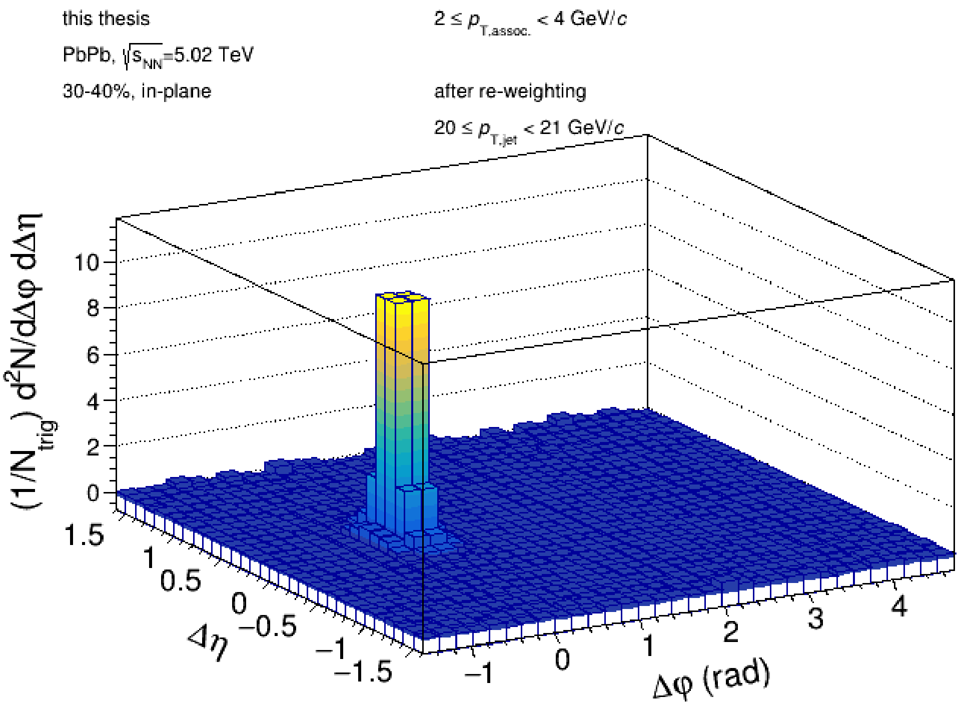

Figure 5.25: Re-weighted correlation function in the particle level p_{T} bin $20 \leq p_{\mathrm{T}}^{\mathrm{part}} < 21$ GeV/c

to Fig. 5.24, are depicted in Fig. 5.26. One can clearly see that the resulting correlation function is an weighted average of the input correlations. This procedure is done for each bin on particle level.

For the pp correlations, almost the same procedure is followed. The differences are the response matrix that is used to unfold the jet spectrum and the prior. Since for pp collisions, only the detector effects have a significant contribution, the PYTHIA pp jets are not embedded to determine the response matrix for pp. Instead, only the smeared tracks and the particle level jets are matched, resulting in the response matrix shown in Fig. 5.27. This matrix again is weighted with the PYTHIA p_{T} spectrum as prior. Since this is the expected "true" shape for pp collisions, it is not weighted with Eq. 5.41. The resulting unfolding matrix and unfolded spectrum are shown in Fig. 5.28.

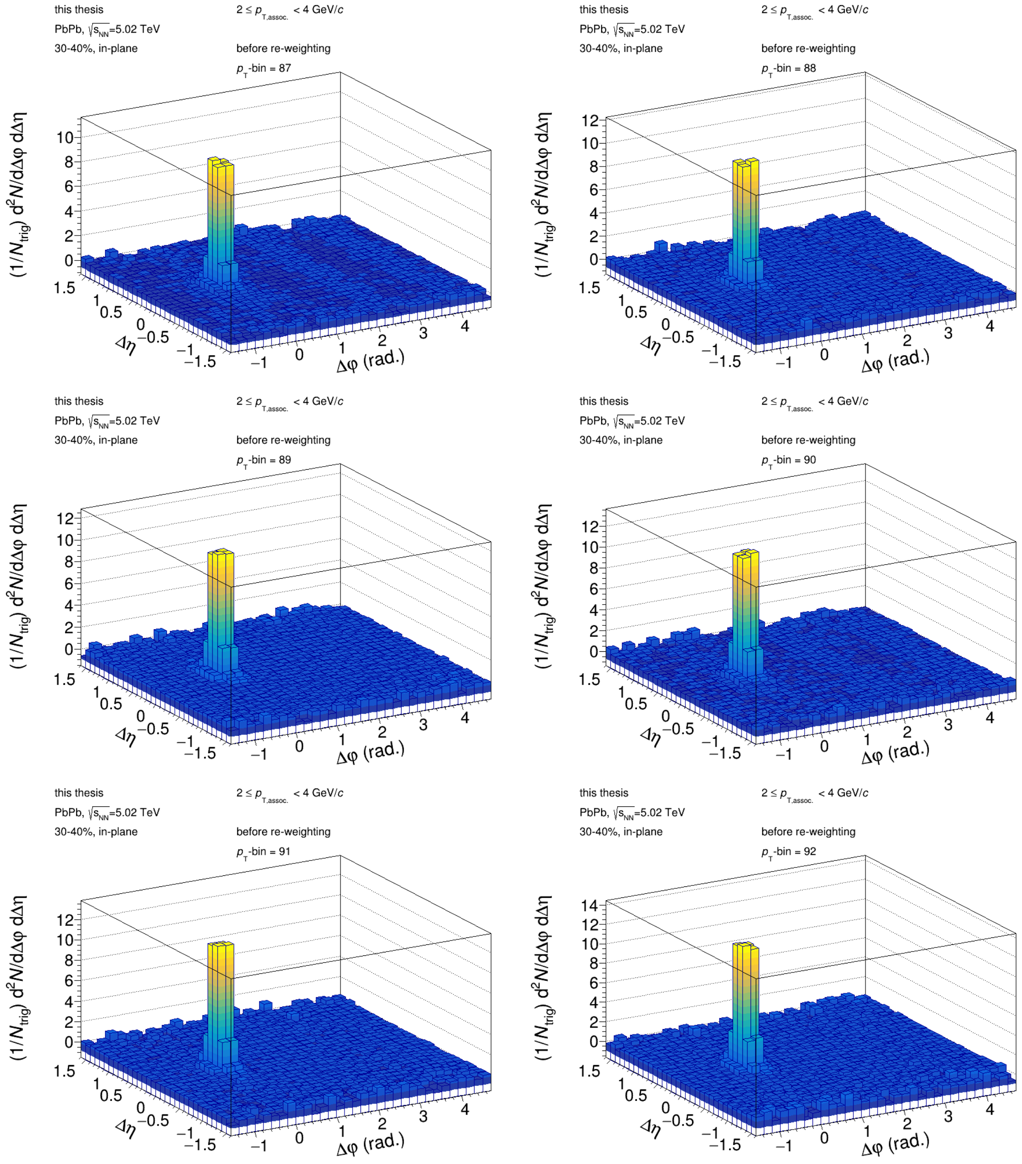

Figure 5.26: Most important input correlations on hybrid level for the particle level p_T bin $20 \le p_T^{part} < 21$ GeV/c.

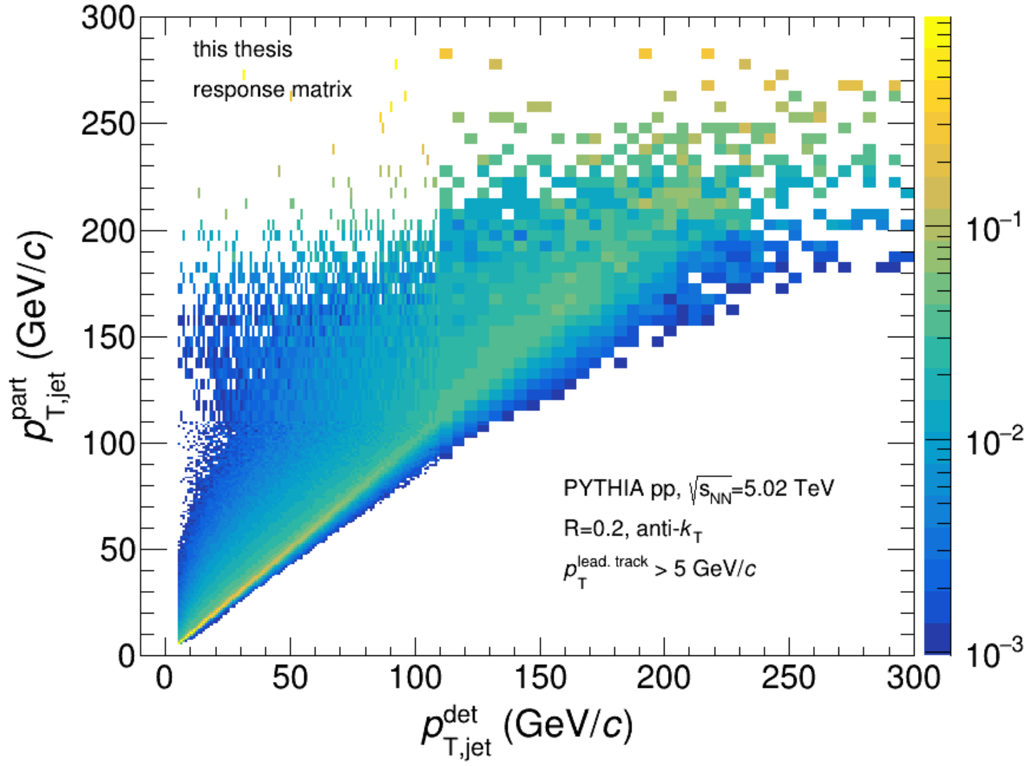

Figure 5.27: Response matrix for pp collisions.

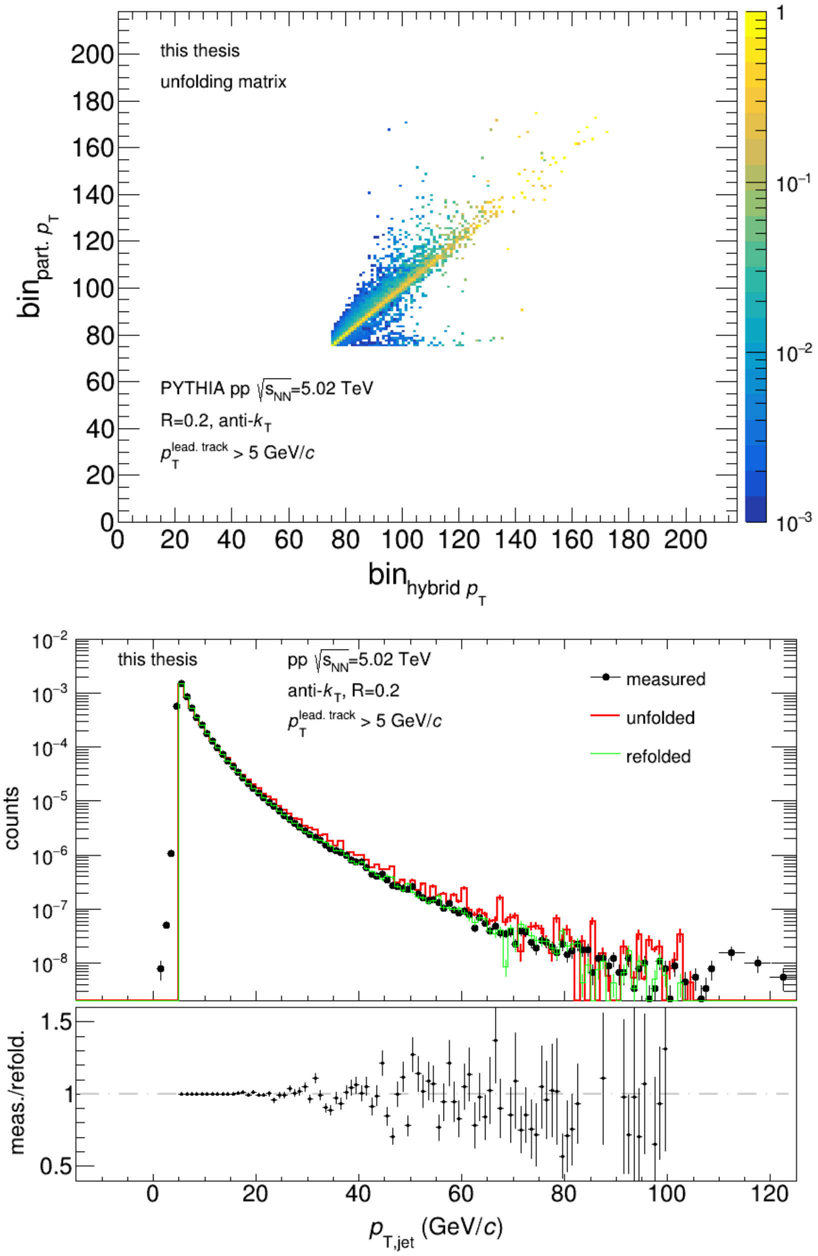

Figure 5.28: Top: Unfolding matrix from unfolding of the pp jet p_T spectrum. Bottom: Measured jet p_T spectrum (black), unfolded spectrum (red) and refolded spectrum (green) for pp collisions.

5.4.2 CLOSURE TEST

The re-weighting procedure described in the previous section was tested with a closure test, to ensure that the behavior is as expected. For the closure test, again PYTHIA jets were used. Since in this way the true distribution is known, one can compare the measured and re-weighted correlations to the truth distribution and evaluate the effectiveness of the unfolding.

For the test, both the particle level jets and the smeared tracks were embedded into PbPb events. With both sets, correlation functions were constructed. The hybrid level jet p_T spectrum (red) was unfolded, resulting in the blue distribution in Fig. 5.29. The PYTHIA truth distribution is depicted in black. Apart from statistical fluctuations the agreement is very good.

The unfolding matrix resulting from this unfolding was then used to re-weight the "measured" correlations according to the procedure described above. Fig. 5.30 shows the ratio between "re-weighted" and "true" correlation function (top left) and the ratio between the "measured" and "true" correlations (top right) in one particle level p_T bin. The bottom row shows the projection of both distributions onto the $\Delta\varphi$ axis. It is visible that the re-weighting procedure reproduces the true correlation shape within fluctuations of $\sim$5 % and shows an improvment of the shape and yield compared to the "measured distribution".

5.5 OBSERVABLES

After the correlations have been re-weighted, the observables can be extracted. For this, the collection of correlation functions is projected onto three jet p_T ranges

- $15 \leq p_\mathrm{T,jet} < 20$ GeV/c
- $20 \leq p_\mathrm{T,jet} < 30$ GeV/c

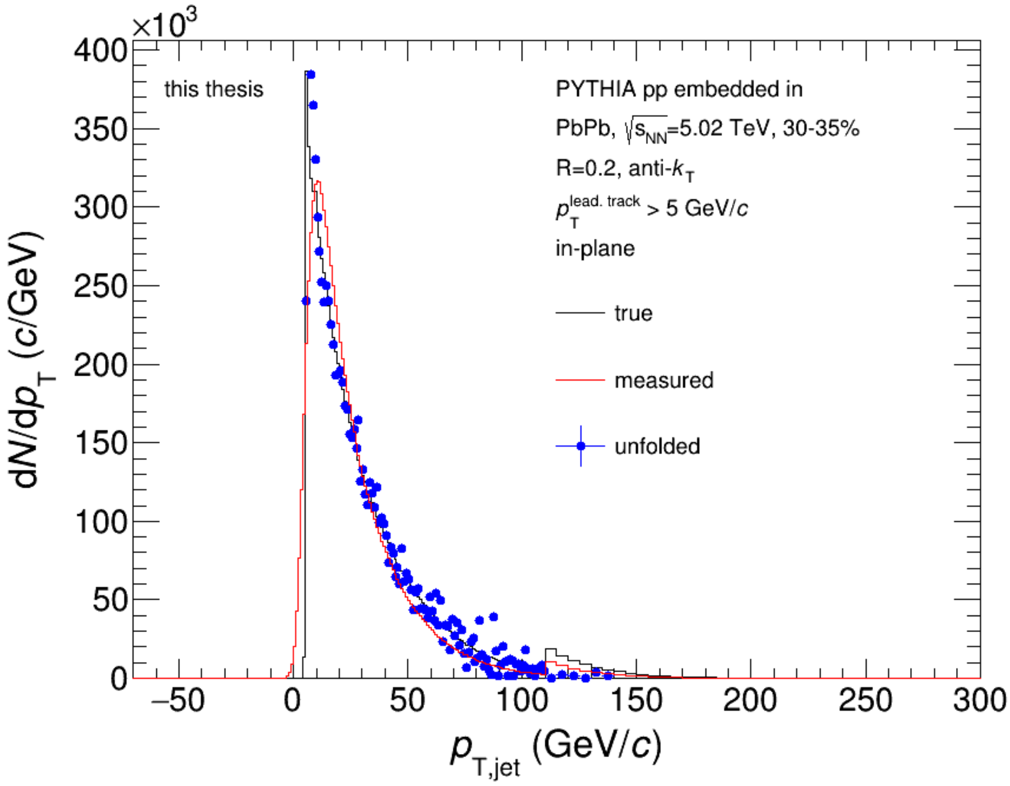

Figure 5.29: Jet p_{T} spectra for the PYTHIA truth level (black), the measured spectrum from embedded PYTHIA jets (red) and the refolded spectrum (blue).

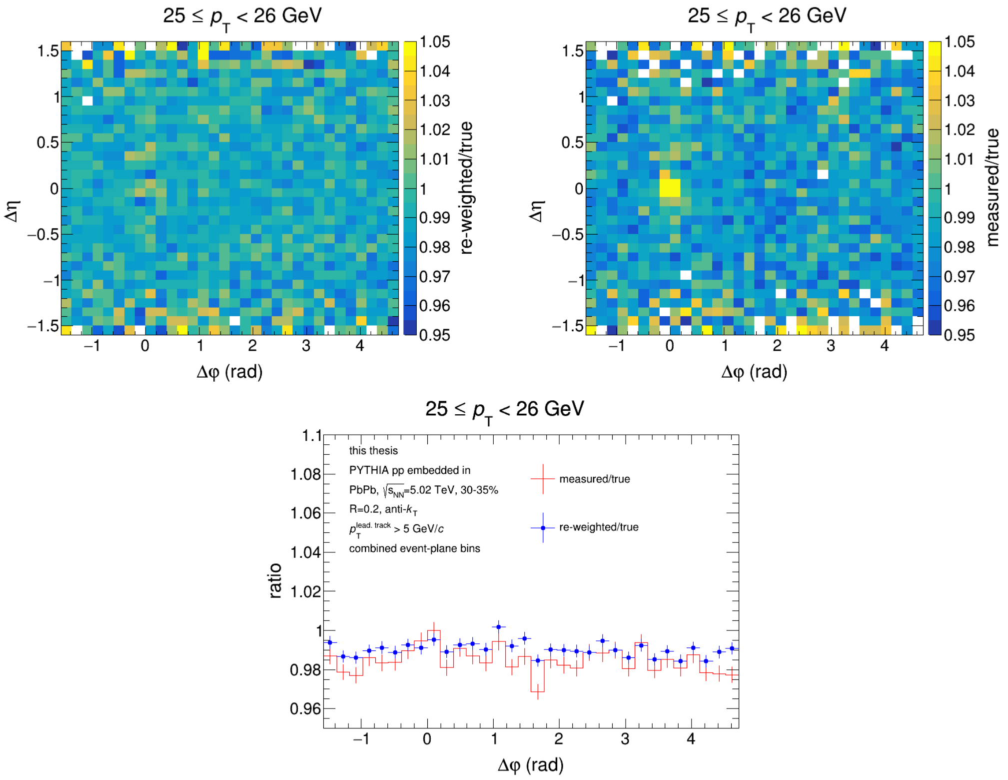

Figure 5.30: Top left: ratio between the re-weighted and true correlation functions, all event plane bins combined. Top right: ratio between the measured and true correlation function. Bottom: Projection of the ratio between re-weighted and true correlation function (blue) and the projection of the ratio between the measured and true correlation function (red).

- $30 \leq p_{\mathrm{T,jet}}$ <40 GeV/c

in all centrality bins. In the further processing, these 2D correlations are projected onto the $\Delta\varphi$ axis and scaled by the bin width in $\Delta\eta$.

To extract the near-side and away-side yields, the projections are integrated over $(-\pi/2 \leq \Delta\varphi < \pi/2)$ and $(\pi/2 \leq \Delta\varphi < 3\pi/2)$, respectively.

The projections and yields are discussed in Ch. 6.

5.6 Systematic uncertainties

For systematic uncertainties, four possible sources are considered: 1) the width scaling of the ME distribution, 2) the tracking efficiency uncertainty, 3) the prior function used for the unfolding and 4) the background subtraction for the correlation functions. The systematic uncertainties were studied by varying these factors and observing the effect on the correlation functions. The errors were determined in each bin in $\Delta\varphi$.

For the uncertainty on the scaling of the ME, the determined best scaling factor was varied by 0.1 %, which corresponds to the steps in which it is determined. The resulting variations on the correlation functions are on average $< 3\%$.

The next uncertainty is the uncertainty of the tracking efficiency. Since our understanding of the detector might be imperfect, this imposes an uncertainty on the efficiency with which we measure particles. In the ALICE TPC this tracking efficiency uncertainty is 3 %. [74] cites 4 %, however recent ALICE-internal investigations concluded a factor of 3 %. This impacts the response matrix, since it contains the information on detector effects by smearing the particle level tracks. To study this effect, an additional response matrix was created, where randomly 3 % of the tracks going into the calculation were rejected. When unfolding the jet spectrum with this response matrix and re-weighting the correlations with the resulting unfolding matrix, this resulted in a on average $< 20\%$ variation on the correlation function. The tracking efficiency uncertainty also affects the overall scale of the correlation function. To account for that, an overall factor of 3 % percent was added in each bin. These uncertainties are also considered for the pp correlations, where also for pp an additional response matrix was made and the overall factor is added.

The variation due to the different parameters in the prior weight was accounted for by utilizing the RMS of the mean. When calculating the mean in each bin of the unfolding matrix, for the systematic studies this mean was varied by the RMS and the resulting unfolding matrix used for the re-weighting. The deviations of the correlation function to the regular one for both plus the RMS and minus the RMS were averaged. This results in an average systematic error of $< 10\%$.

The last systematic uncertainty that was considered for this analysis is the variation in the background of the correlation functions. To study this, the $\Delta\eta$ projection range for the background fit was varied by one bin in each direction to $0.9 < |\Delta\eta| < 1.4$. The propagation of this cut variation resulted on average in an error of $< 20\%$

The relative errors were added in quadrature in each bin and used to determine the systematic uncertainties on the yield and the I_{AA}.

6 RESULTS AND DISCUSSION

6.1 PROJECTIONS OF THE JET-HADRON CORRELATION FUNCTIONS

In this section, the projections of the 2D jet-hadron correlations are discussed. For better visibility, only the correlations in the centrality bin 30-40% and for $15 \leq p_{\mathrm{T,jet}} < 20$ GeV/c are depicted here in Fig. 6.1. The rest can be found in appendix A.6.

All correlations show the expected near-side and away-side peaks. While the near-side peak is shaped as expected, the away-side exhibits a double peak structure for centralities <50% and associated p_{T} <4 GeV/c. This is a remnant of the background subtraction, which tends to overestimate the background on the away-side. Since the peak on the away-side is additionally broader than the near-side peak, the observed double peak structure occurs. Another feature of the over-subtraction of the background on the away-side can be possible negative entries when integrating over the peaks to determine the yields. This can on occasion result in negative yields. These are not physical, despite being based on our well-established understanding of the flow modulations and the rather simple assumption that the background can be modelled by a Fourier expansion. Recent studies [75] show that the fit to the event plane seems to break down with high-statistics data. This should be investigated more in the future.

A further feature visible in the correlations is that the peaks become smaller and narrower for increasing associated p_{T} . This shows that jets are less likely to contain a large number of high p_T constituents, but rather fragment into a larger number of constituents with lower p_T . Since the peak becomes narrower this means that the highest p_T jet fragment follows the direction of the jet, while the lower p_T components spread around the jet axis. In the next section, the yields obtained from these projections are discussed.

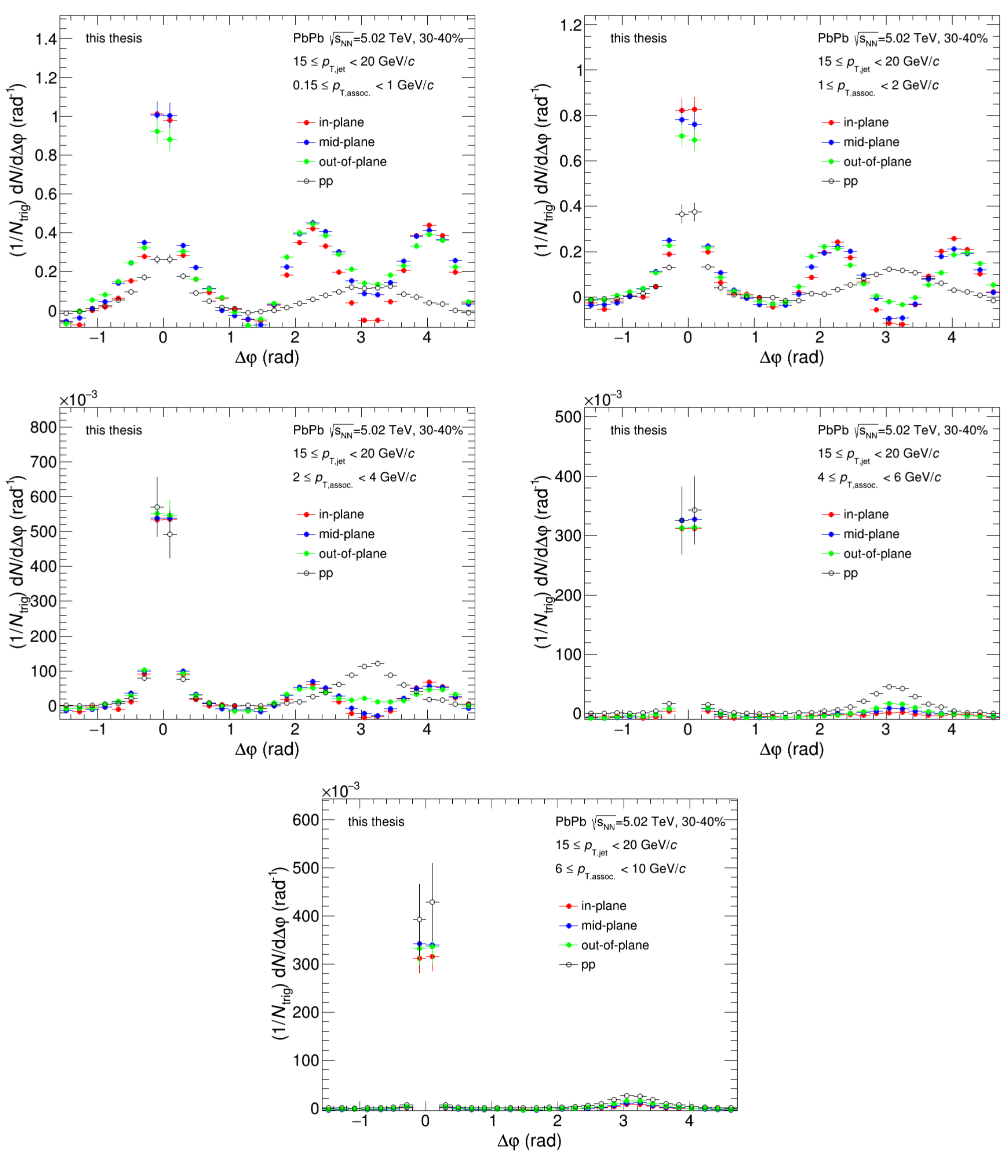

Figure 6.1: $\Delta\varphi$ projections of the jet-hadron correlations for $15 \leq p_{\mathrm{T,jet}} < 20$ GeV/c. The in-plane (red), mid-plane (blue) and out-of-plane (green) distributions for 30-40% PbPb are depicted as well as the distribution in pp.

6.2 PER-TRIGGER YIELDS

The per-trigger yields on the near and away side are shown in Fig. 6.2 for the centrality bin 30-40% and in appendix A.7 for all centrality bins. For better visibility, the points for each event plane orientation are slightly displaced within the associated p_T bin.

In general, the yields are decreasing with increasing associated p_T across all centralities, with a stronger slope on the away-side. This is consistent with the finding that the peak in the projections decreases with increasing associated p_T .

While the event plane ordering of the yields fluctuates a lot across centralities and p_T bins, an interesting ordering is visible especially for the more central and semi-central centrality bins 10-20%, 20-30% and 30-40%: The out-of-plane yield is the highest, the in-plane yield is the lowest, and the mid-plane yield fluctuating in positions. This is interesting, since intuitively the out-of-plane bin accounts for the longest path length in the medium. To further investigate this, the yields are now divided to obtain the I_{AA} and for comparison to model calculations.

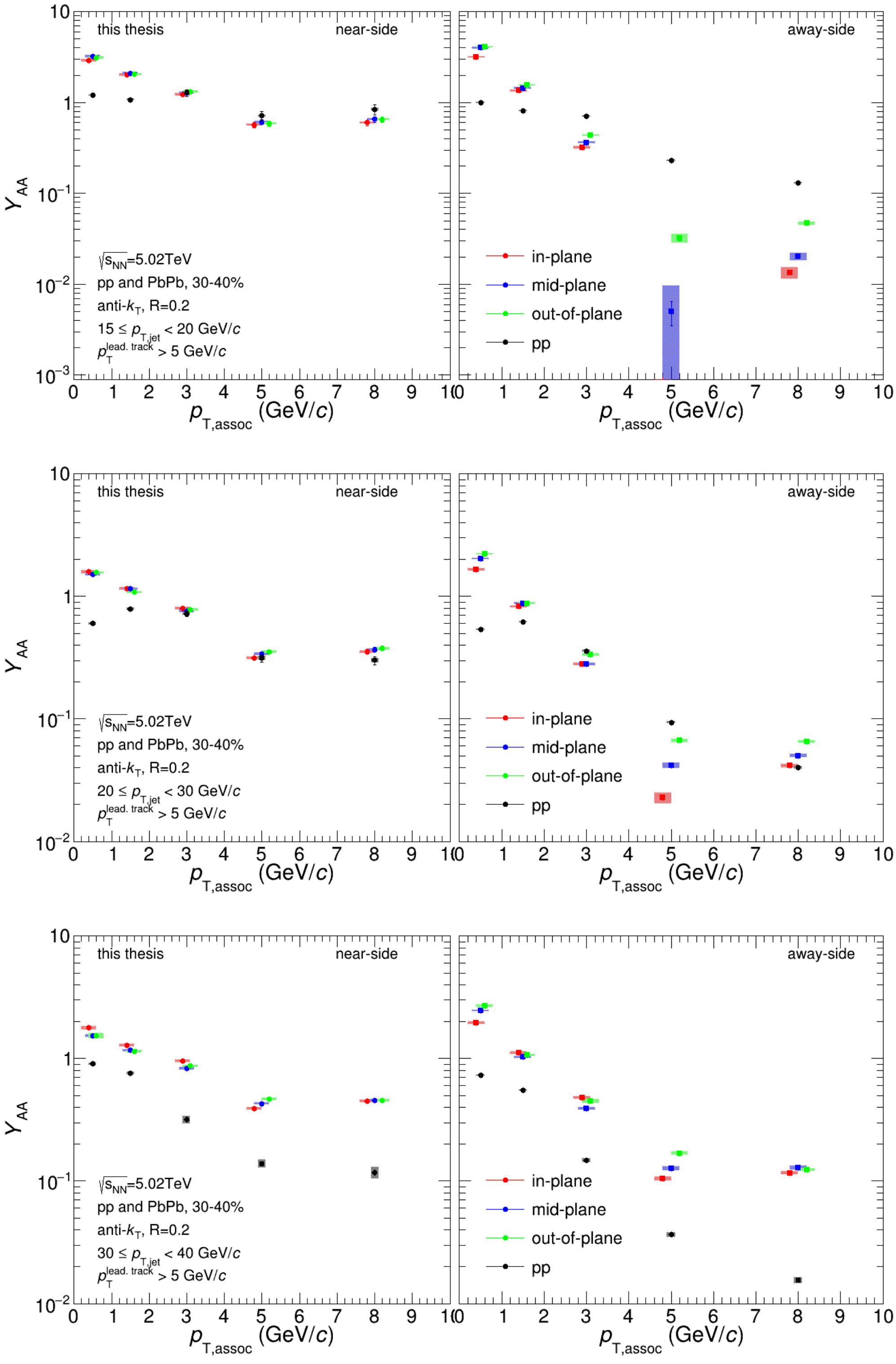

Figure 6.2: Per-trigger yields on the near-side and away side for PbPb collisions at 30-40% centrality and pp collisions in all selected jet p_T bins.

6.3 I_{AA}

Fig. 6.3 shows the I_{AA} for 30-40% centrality PbPb and pp collisions. The selected p_{T} bins are $15 \leq p_{\mathrm{T},jet} <$20 GeV/c and $20 \leq p_{\mathrm{T},jet} <$30 GeV/c. In the same plots, the calculations with JEWEL for the same centrality and jet p_{T} selection is depicted.

For $15 \leq p_{\mathrm{T},jet} <$20 GeV/c, the JEWEL calculations describe the measured yield ratios well, especially on the near-side. For associated p_{T} >2 GeV/c on the away-side JEWEL overestimates the ratio, however the reason for the discrepancy might lie in the over-subtraction of the background on the away-side. More studies on background subtraction methods are needed to clear this question. For $20 \leq p_{\mathrm{T},jet} <$30 GeV/c, JEWEL follows the trend of the measurement, but overestimates the ratio for low associated p_{T} and underestimates it for higher associated p_{T} . The over-estimation of the I_{AA} for $p_{\mathrm{T,assoc}} <$1 GeV/c might be a result of jets in PbPb that are reconstructed solely from recoil particles. Since the recoils from the medium are kept in the event record (see Sec. 3.3.2) they can be reconstructed to low p_{T} jets, resulting in an enhancement in that momentum region.

In both cases JEWEL as well as the measurement show a slight ordering of the event planes, with the out-of-plane bin showing the highest ratio.

For $15 \leq p_{\mathrm{T},jet} <$20 GeV/c, the I_{AA} shows an enhancement of $p_{\mathrm{T,assoc}} <$2 GeV/c on both the near and away-side and a ratio consistent with 1 on the near-side for $2 \leq p_{\mathrm{T,assoc}} <$4 GeV/c. The same bin is suppressed on the away-side. $p_{\mathrm{T,assoc}} >$4 GeV/c is suppressed on both the near and away-side. These observations are consistent with a softening of the jet fragmentation, where high p_{T} particles get quenched and therefore a yield enhancement of low p_{T} particles is observed. This effect is more pronounced on the away-side, indicating a longer path length through the medium.

For $20 \leq p_{\mathrm{T},jet} <$30 GeV/c, the I_{AA} shows a slight enhancement for $6 \leq p_{\mathrm{T,assoc}} <$10 GeV/c, while the bins $2 \leq p_{\mathrm{T,assoc}} <$6 GeV/c are suppressed on the away-side and consistent with 1 on the near side. $p_{\mathrm{T,assoc}} <$2 GeV/c are again enhanced. This would indicate that for higher p_{T} jets, in the presence of a medium the jet fragments into one high p_{T} particle and many low p_T particles, while in pp the jet fragments into several mid-p_T particles instead.

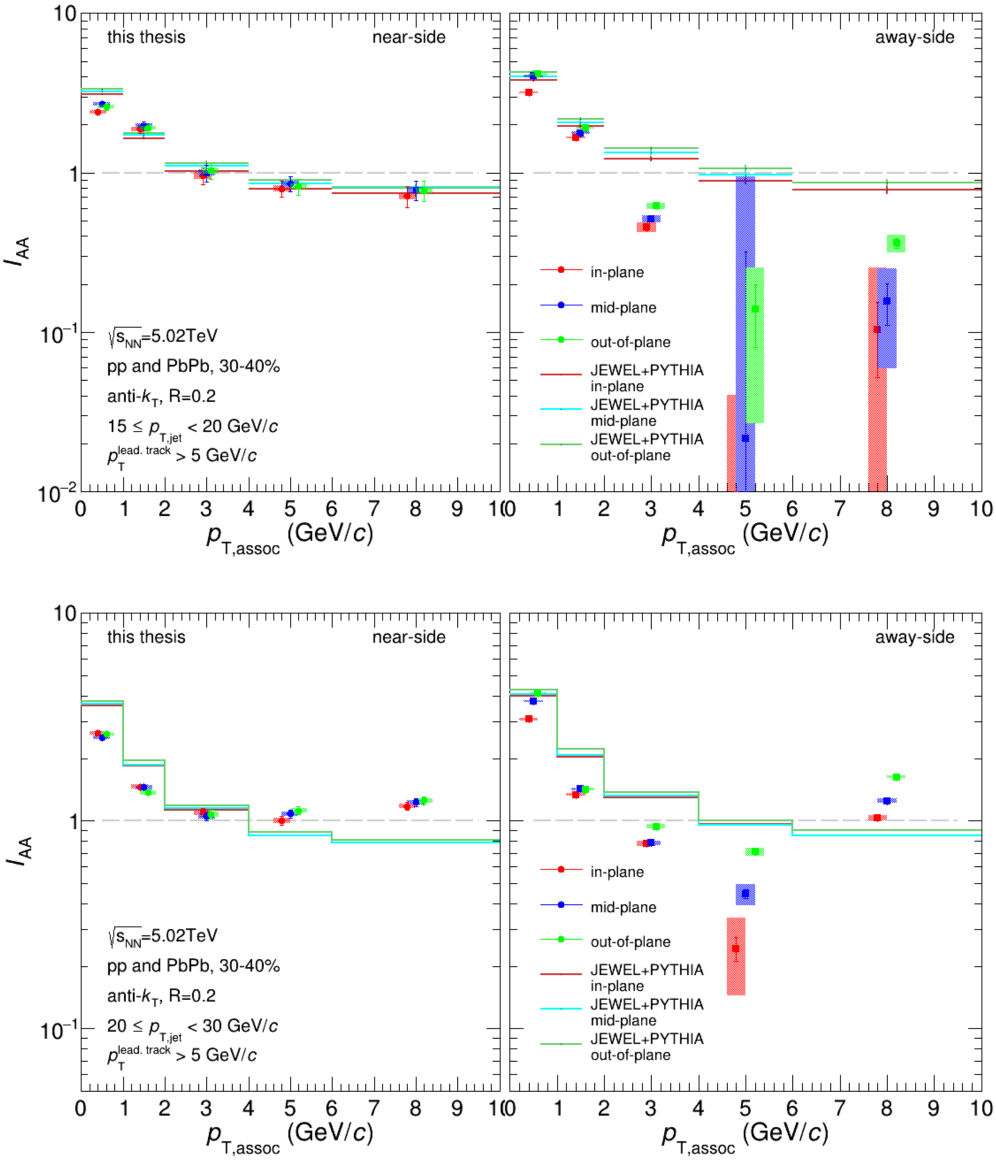

Figure 6.3: I_{AA} between 30-40% PbPb and pp collisions. JEWEL+PYTHIA calculations are depicted as solid lines.

Another way to look at the yield modification in PbPb collisions is the centrality dependence of the I_{AA}. Specifically looking at in-plane jets, the path length should vary strongly between central and peripheral collisions. Therefore, the yield modification for in-plane jets is expected to show a stronger dependence on the centrality percentile than out-of-plane jets. Fig. 6.4 shows the I_{AA} as a function of the centrality percentile for both $15 \leq p_{\mathrm{T},jet}$ <20 GeV/c and $20 \leq p_{\mathrm{T},jet}$ <30 GeV/c. No significant dependence of the I_{AA} on the centrality percentile is observed for this associated p_{T} bin. Furthermore, the difference between in-plane and out-of-plane is consistent within the systematic and statistical errors. One would expect that the difference in path-length probed by in-plane and out-of-plane jets would be more significant in peripheral events than in central events, since central events are more symmetric. However, considering the uncertainties, actually a slightly stronger variation between the in-plane and out-of-plane I_{AA} is visible. This, together with the observation of the fluctuating yield orderings might suggest that indeed fluctuation play a higher role in jet energy loss than the path length dependence, as was discussed before [36].

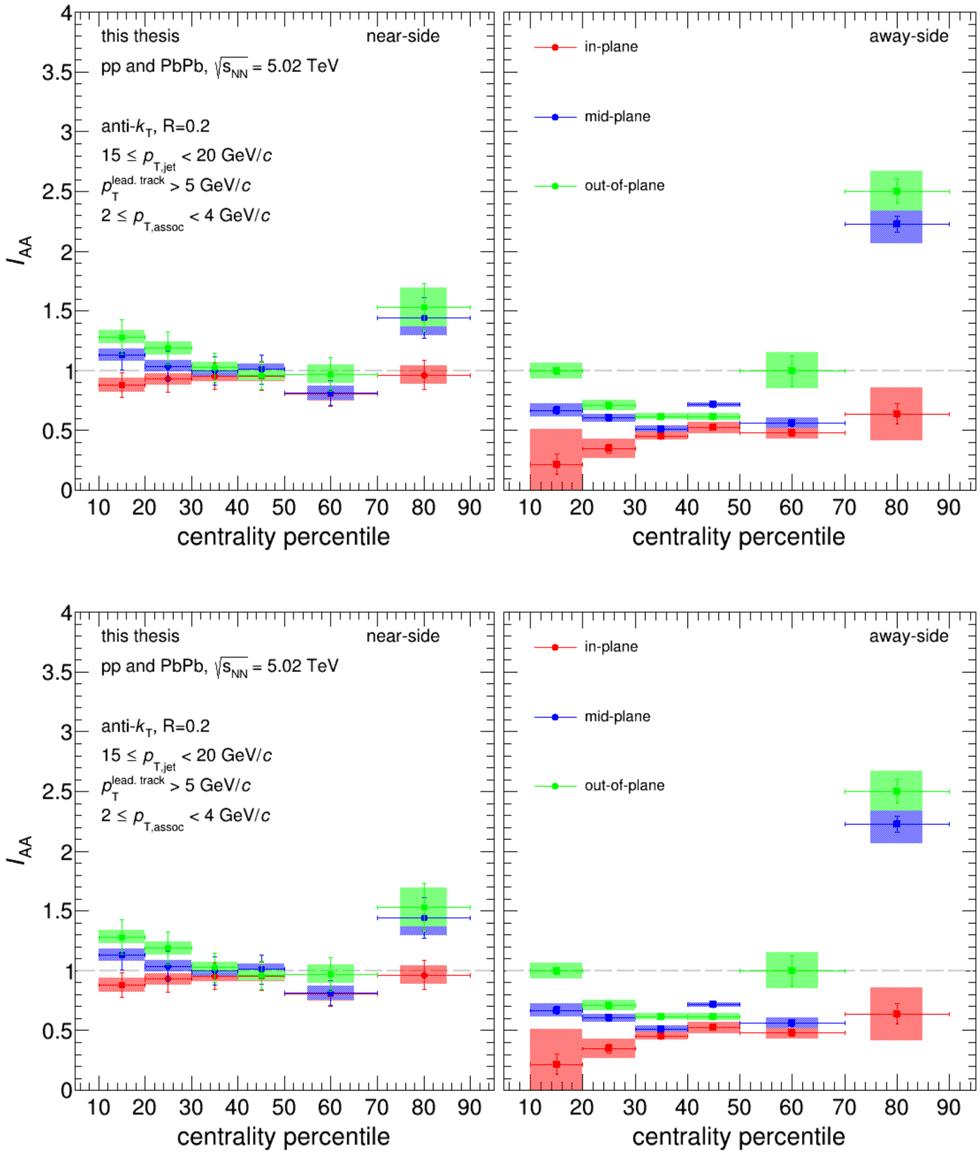

Figure 6.4: Centrality dependent I_{AA} for $15 \leq p_{T,jet} < 20$ GeV/c and $20 \leq p_{T,jet} < 30$ GeV/c and in the selected associated p_T bin $2 \leq p_{T,assoc} < 4$ GeV/c.

7 Conclusion and Outlook

Under extreme conditions, hadronic matter undergoes a phase transition. For temperatures above 156 MeV, the confinement of quarks and gluons is dissolved and a new state of matter is created, the Quark-Gluon Plasma (QGP). In heavy ion collisions at the ALICE experiment at CERN, these extreme conditions are met and the QGP is produced. Jets, sprays of particles originating from hard scatterings at early stages of the collision, travel through the QGP and interact with the mediums constituents. This leads to an energy modification of the jet, which is dependent on the path length of the jet in the medium. By comparing the jet energy modifications in PbPb to jet measurements in pp, one gains insight into the interaction properties of the QGP.

The measurement of jet energy modifications is a complicated task. Due to the large number of background particles in a heavy ion collision, a measurement of the quenching on a jet-by-jet basis is impossible. In this thesis, jet-hadron correlations are constructed to access the jet quenching on a statistical basis. The correlation functions are constructed by calculating the angular differences between trigger jets and the associated particles of the event. In order to access the path length dependence of the energy modifications, the correlations are calculated for different orientations of the jet to the symmetry plane of the event (event plane). Corrections are applied to the correlation function to remove the contribution of fake jets and the correlated background from the underlying event. The fake jets are removed by modeling their contribution using event mixing. The correlated background is removed by fitting the background region of the correlations with a Fourier expansion,accounting for the flow modulation of the background.

The detector effects and distortion of the jet momentum by background particles is accounted for by unfolding. For this thesis, a unfolding procedure was developed that not only unfolds the jet p_{T} spectrum back to particle level, but also re-weights the momentum dependent correlation functions. The unfolding matrix obtained in the unfolding of the jet p_{T} spectrum was used to migrate the entries of the correlations from the reconstructed jet momentum to the particle level p_{T} . A closure test with PYTHIA simulations shows a good agreement between the correlations constructed with the true jet momentum and the correlations that were re-weighted from the measured level back to particle level. Differences in yield are below 5 % and the shape of the peak and background was reproduced to a satisfactory level. Re-weighting of the correlations in both PbPb and pp collisions enables us to select similar underlying jet spectra for the comparison between PbPb and pp and the evaluation of the jet energy modifications. Furthermore, the unfolding back to particle level allows for a direct comparison to model calculations.

Evaluating the per-trigger yields and I_{AA}, several observations can be made. First, the yields decrease with increasing associated particle momentum across all centralities. This means that on average, a jet contains several low p_{T} particles but only few high p_{T} particles. The I_{AA} is generally larger than 1 across all centralities and jet momenta for $p_{\mathrm{T,assoc}}$ $<$2 GeV/c and for both the near-side and away-side. This indicates a quenching of the jets constituents with higher p_{T} , leading to an enhancement at low p_{T} . The momentum threshold for which a suppression takes place varies across the centrality bins. Comparing the I_{AA} for 30-40% PbPb over pp data to JEWEL calculations, a good agreement is found especially on the near-side for low p_{T} $15 \leq p_{T,jet}$ $<$20 GeV/c. The ratio tends to be overestimated on the away-side for $p_{\mathrm{T,assoc}}$ $>$2 GeV/c, which is likely an effect of the over-subtraction of the background on the away-side in the data correlations. The slight over-estimation of the I_{AA} in the lowest associated p_{T} bin might be due to low p_{T}

jets that are reconstructed only from JEWEL recoil particles. In both JEWEL and the data a slight ordering of the ratios with the event plane is visible. The out-of-plane jets have a higher ratio than in-plane jets, reversing the expectation that the out-of-plane bin should have the longest path-length. Additionally, a comparison of the I_{AA} across all centrality bins shows no significant dependence of the ratio on the centrality. If the I_{AA} observable showed a strong dependence on the path length, one would expect strong modulation of especially the in-plane jets when going from central to peripheral events, i.e. a longer path length to a shorter path length. These findings support the suggestion that fluctuations are the dominant effect in the jet energy modifications over the path length.

For future analyses, the comparison of the per-trigger yields and I_{AA} to different simulations could help clarify the interpretation of these results. The medium model in JEWEL is relatively simple, with QGP expansion only extending in longitudinal direction. It would be interesting to see if for example a model that employs more hydrodynamic calculations can explain the inverse ordering of the yields with the event plane, or if the suspicion of fluctuations being the dominant effect is confirmed. Furthermore, more studies need to be done on the background subtraction, since the over subtraction on the away-side complicate the interpretation of the yields and I_{AA}.

A APPENDICES

A.1 Pileup cuts

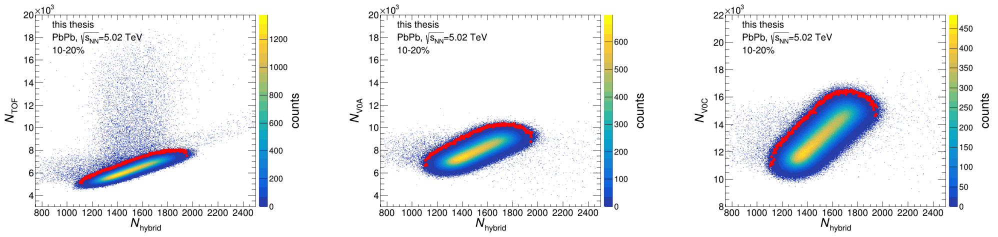

Figure A.1: Pile-up cuts for the 10-20% centrality bin

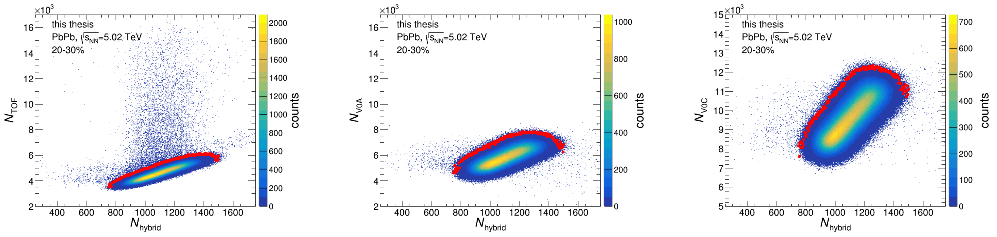

Figure A.2: Pile-up cuts for the 20-30% centrality bin

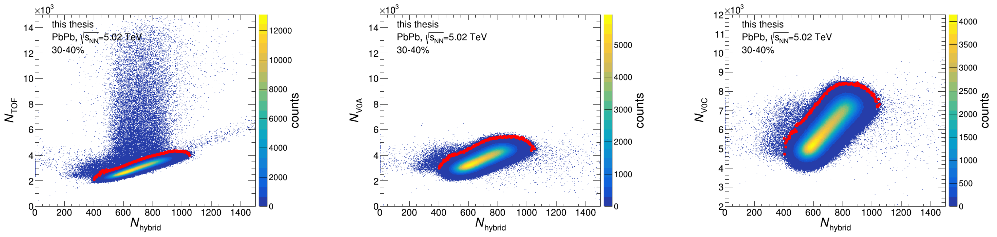

Figure A.3: Pile-up cuts for the 30-40% centrality bin

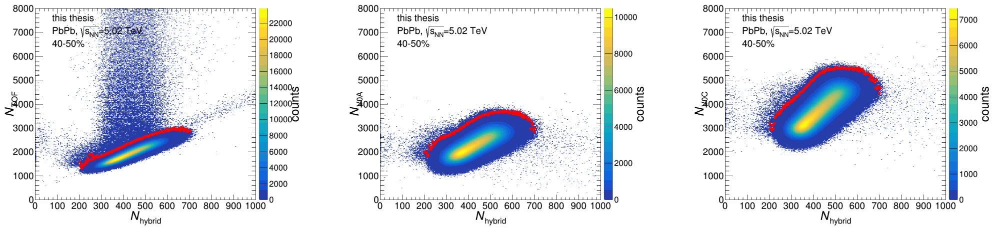

Figure A.4: Pile-up cuts for the 40-50% centrality bin

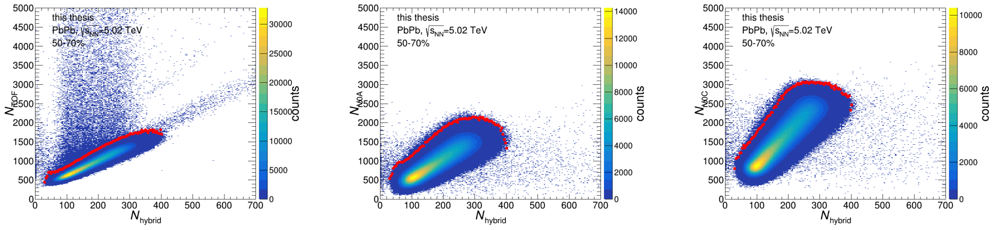

Figure A.5: Pile-up cuts for the 50-70% centrality bin

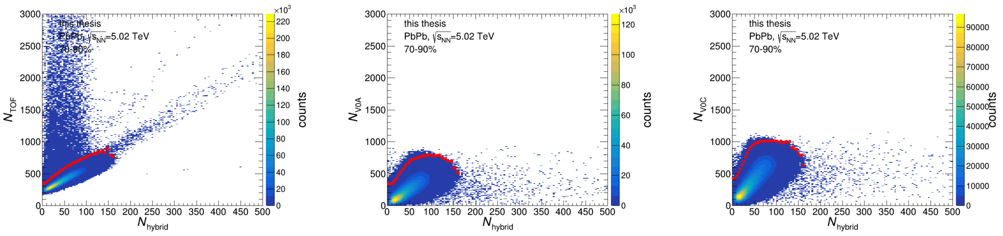

Figure A.6: Pile-up cuts for the 70-90% centrality bin

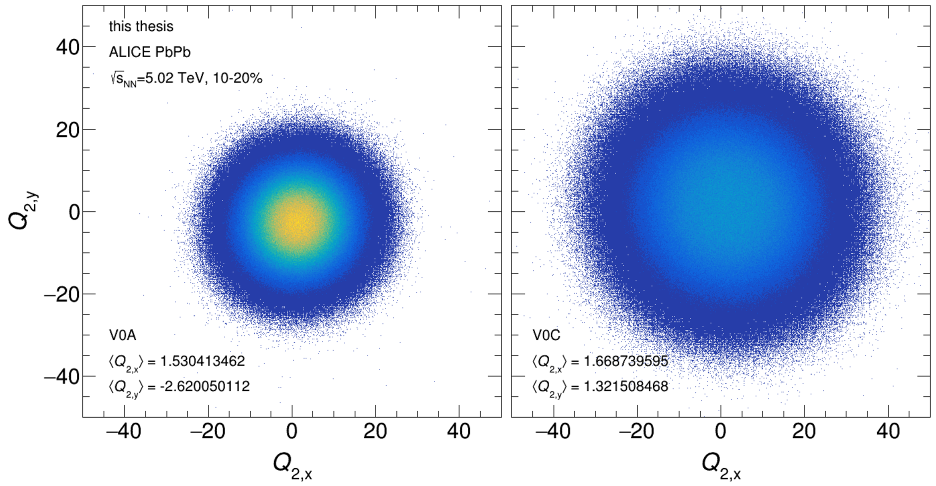

Figure A.7: Q_n vector distribution for 10-20% centrality

A.2 Q_n VECTOR AND Ψ_2 DISTRIBUTIONS FOR ALL CENTRALITIES

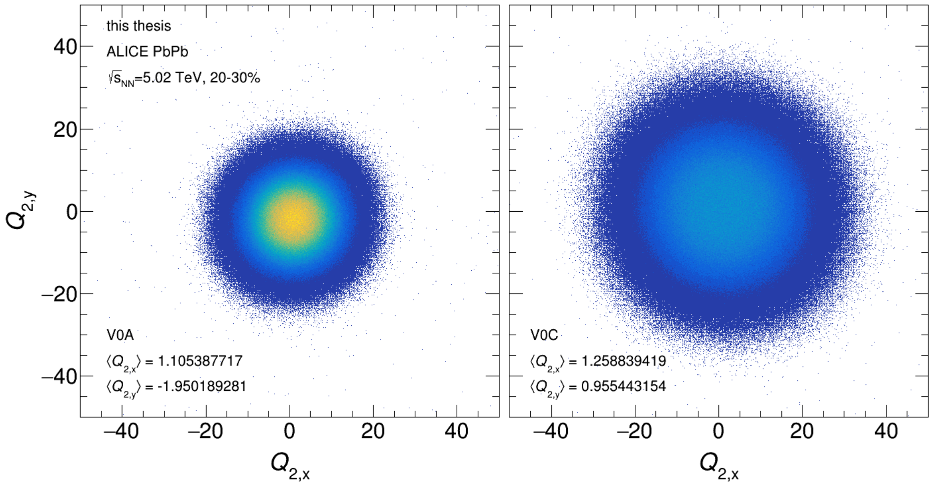

Figure A.8: Q_n vector distribution for 20-30% centrality

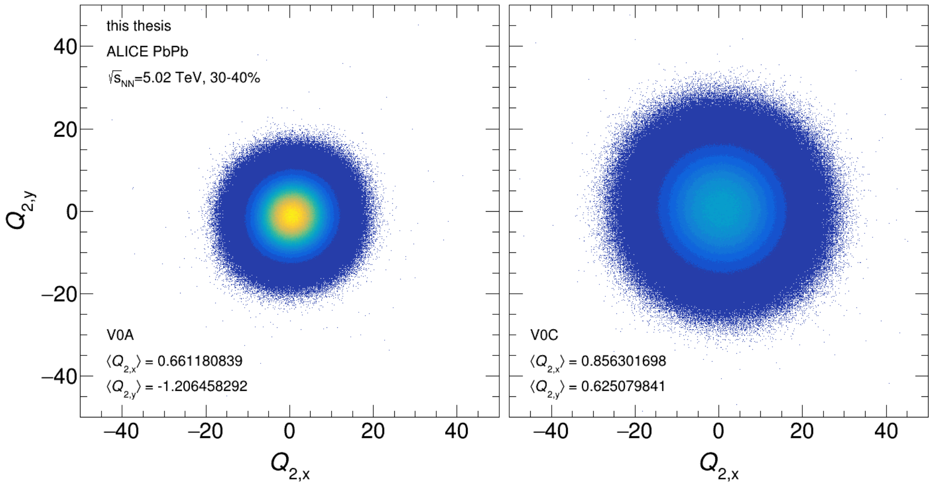

Figure A.9: Q_n vector distribution for 30-40% centrality

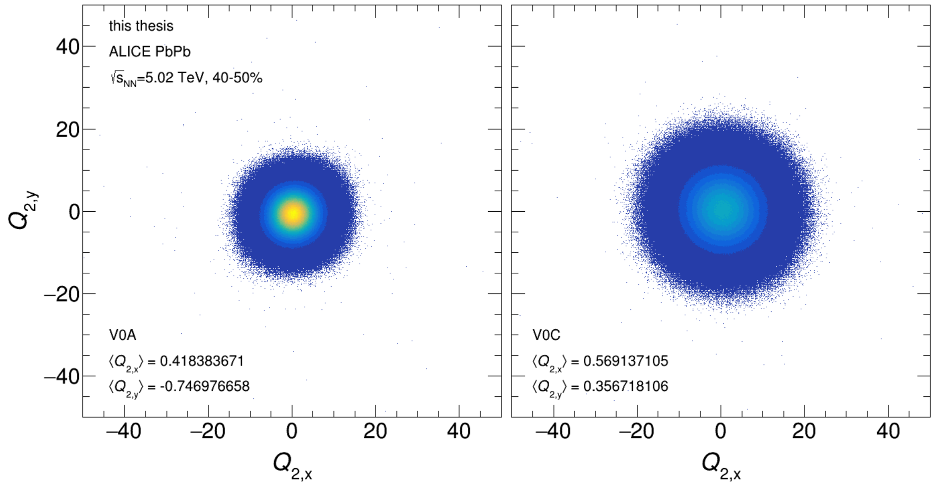

Figure A.10: Q_n vector distribution for 40-50% centrality

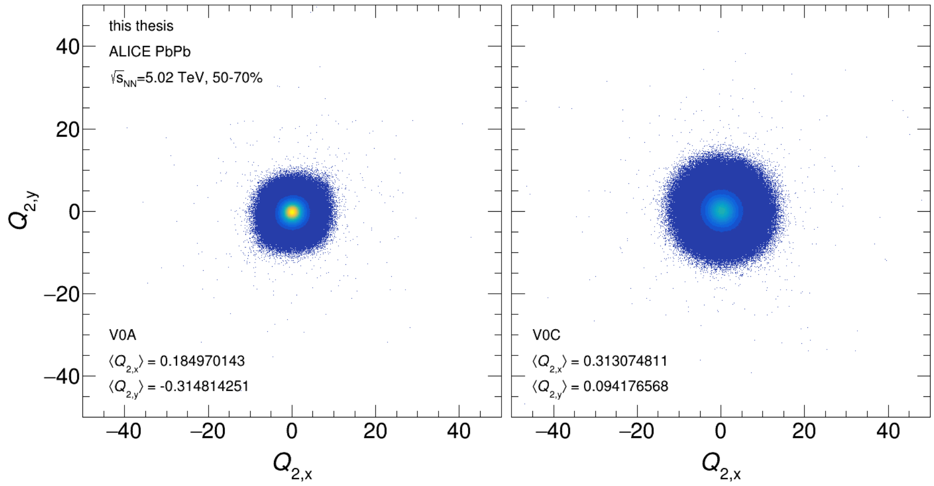

Figure A.11: Q_n vector distribution for 50-70% centrality

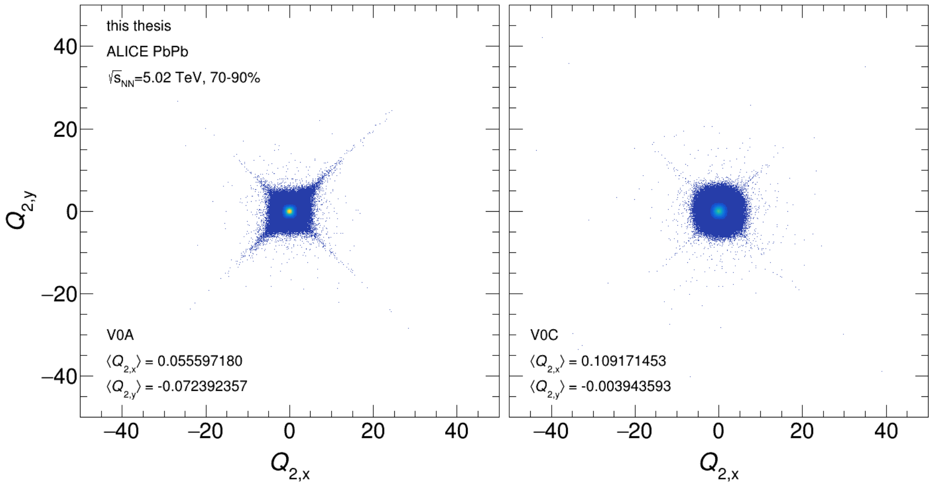

Figure A.12: Q_n vector distribution for 70-90% centrality

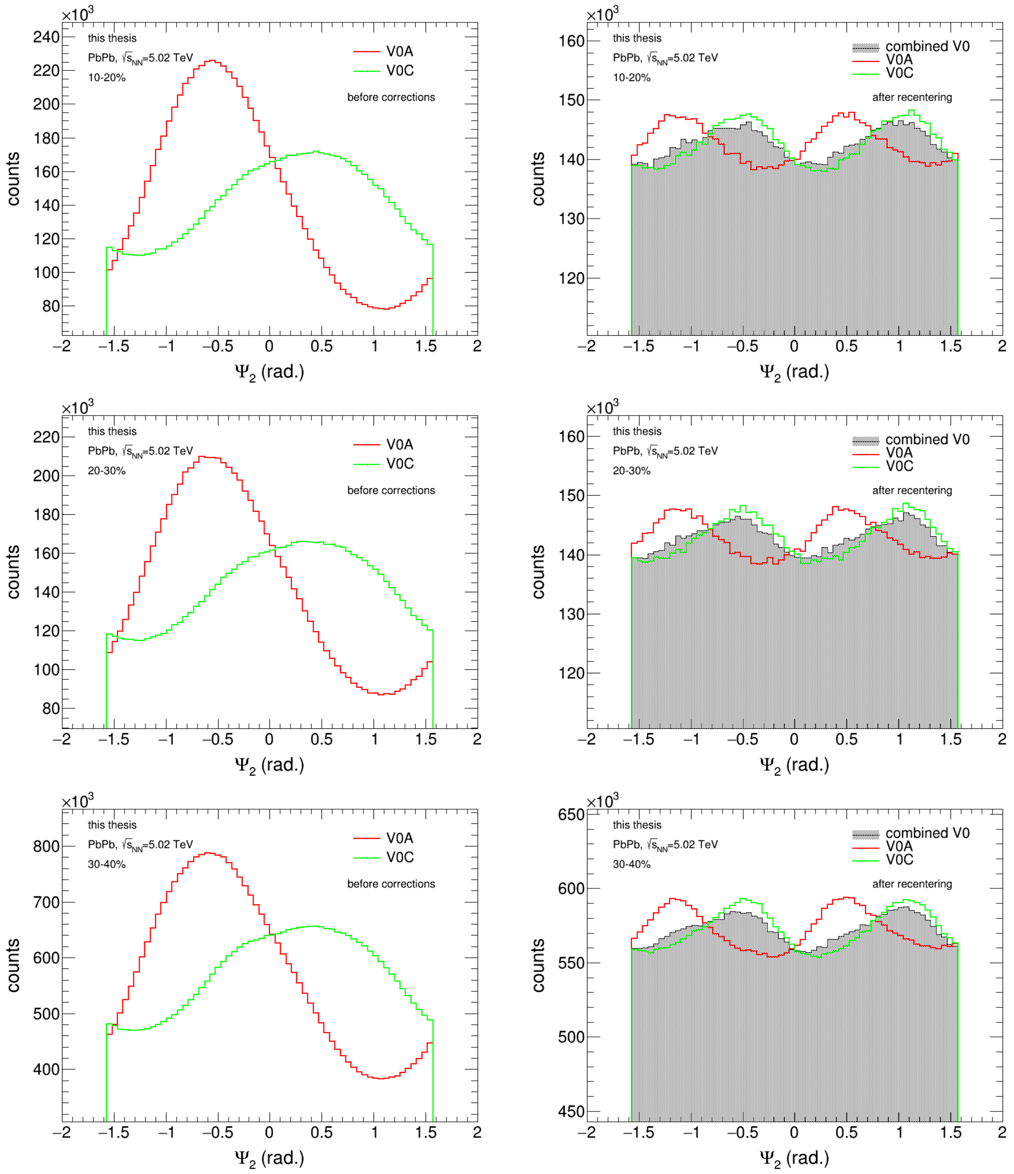

Figure A.13: Ψ_2 distributions before corrections and after recentering, for centrality binis 10-20%, 20-30%, 30-40%

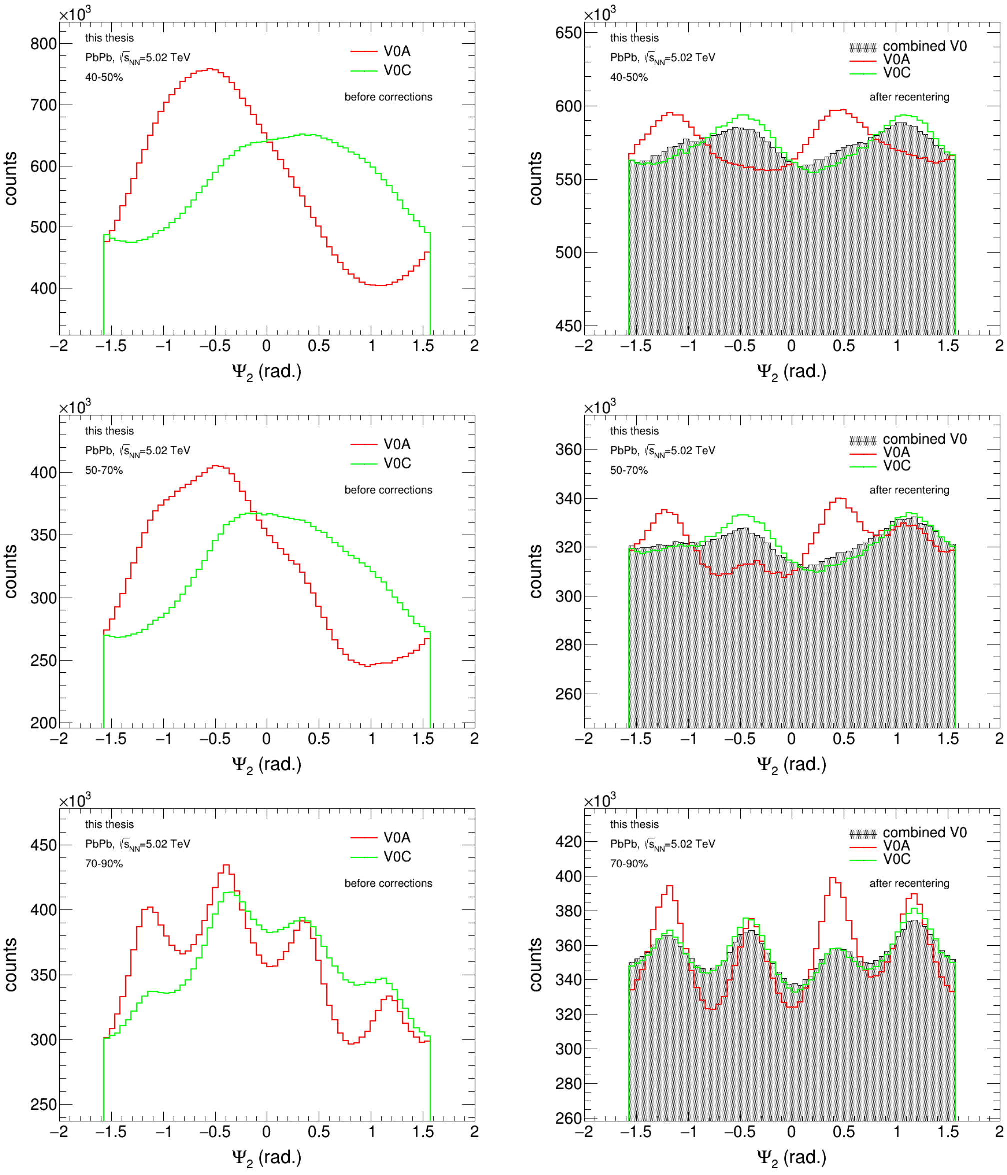

Figure A.14: Ψ_2 distributions before corrections and after recentering, for centrality binis 40-50%, 50-70%, 70-90%

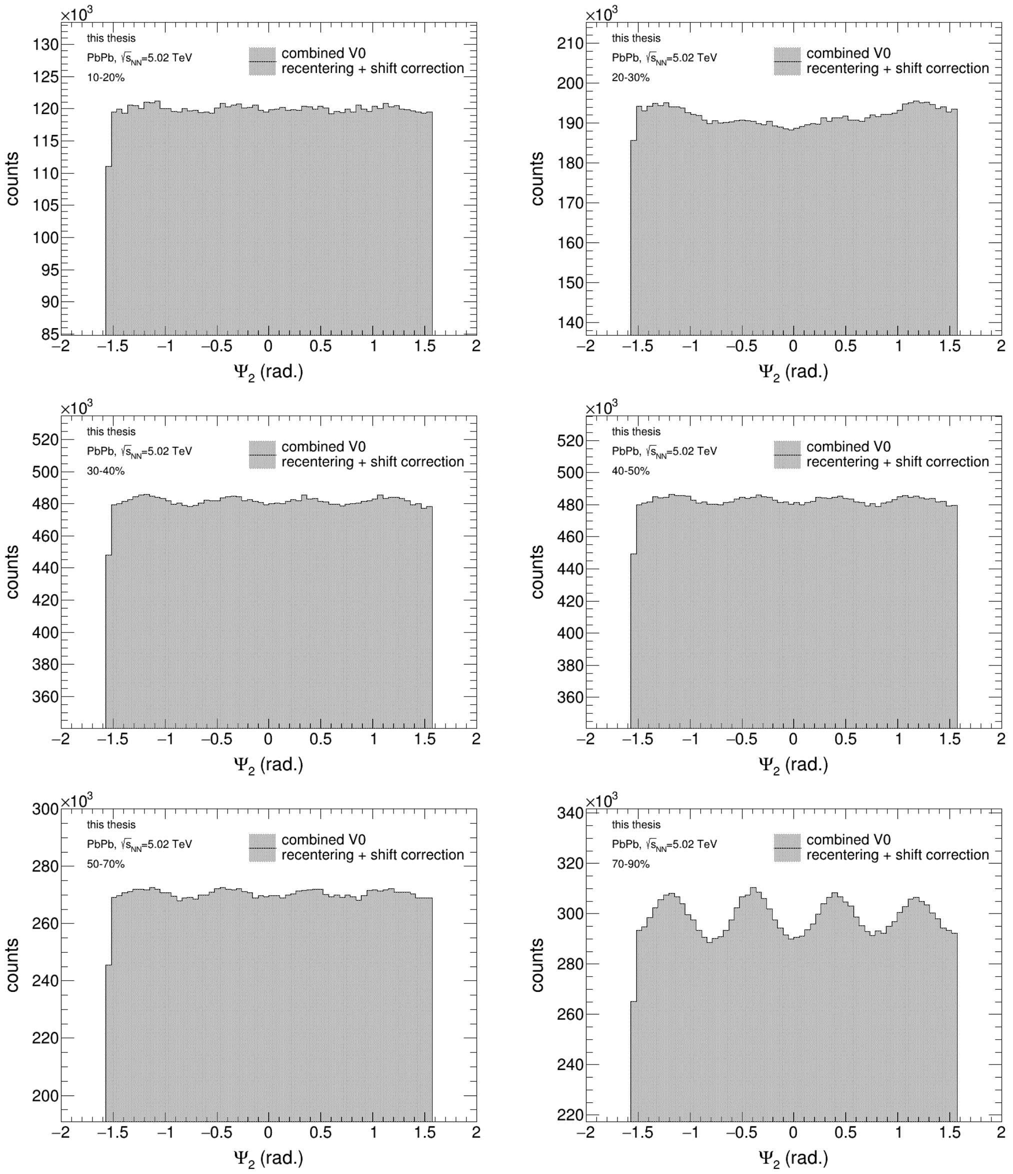

Figure A.15: full corrected Ψ_2 distributions for centrality bins 10-20%, 20-30%, 30-40%

A.3 JET p_{T} DISTRIBUTIONS, SE AND ME FOR ALL CENTRALITIES

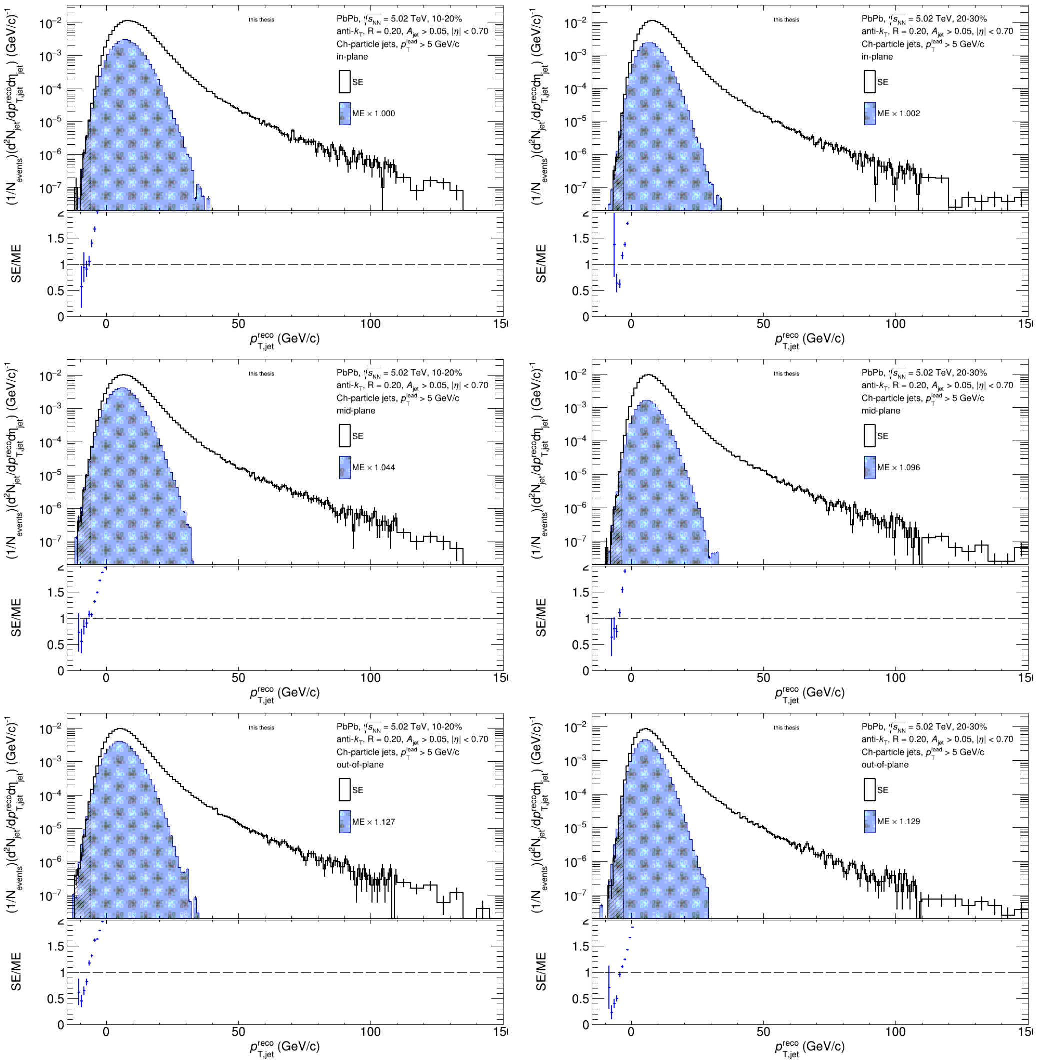

Figure A.16: SE and ME jet p_T distributions for centrality bins 10-20% and 20-30%

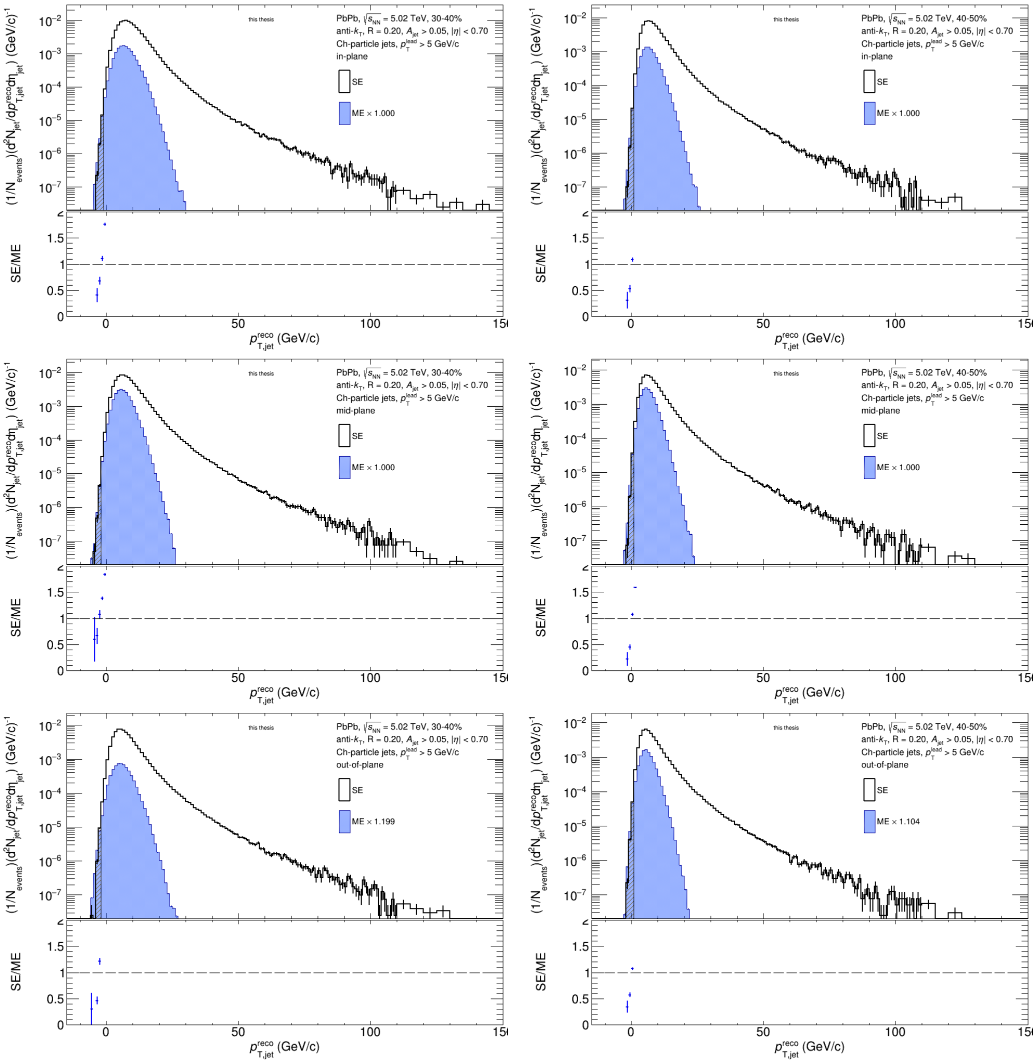

Figure A.17: SE and ME jet p_T distributions for centrality bins 30-40% and 40-50%

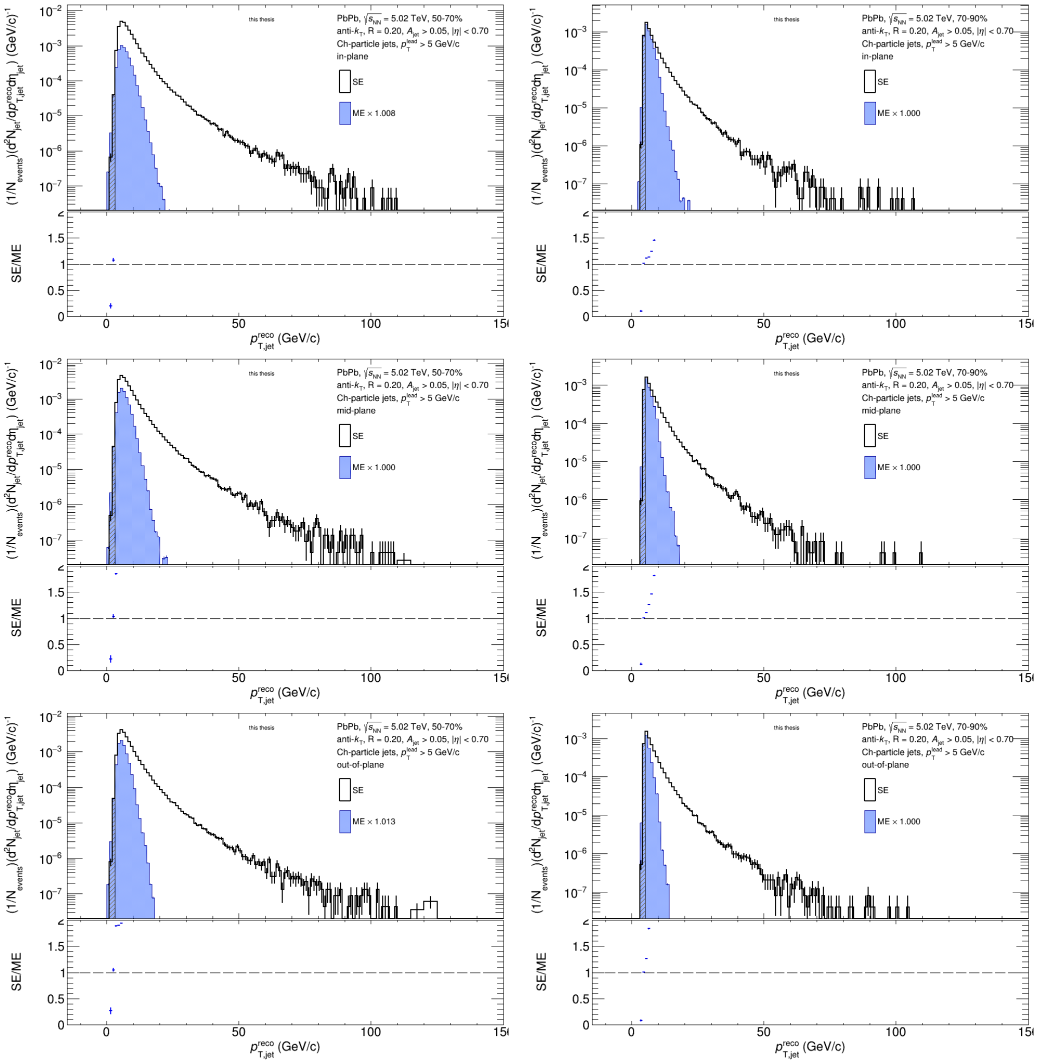

Figure A.18: SE and ME jet p_T distributions for centrality bins 50-70% and 70-90%

A.4 BACKGROUND FITS

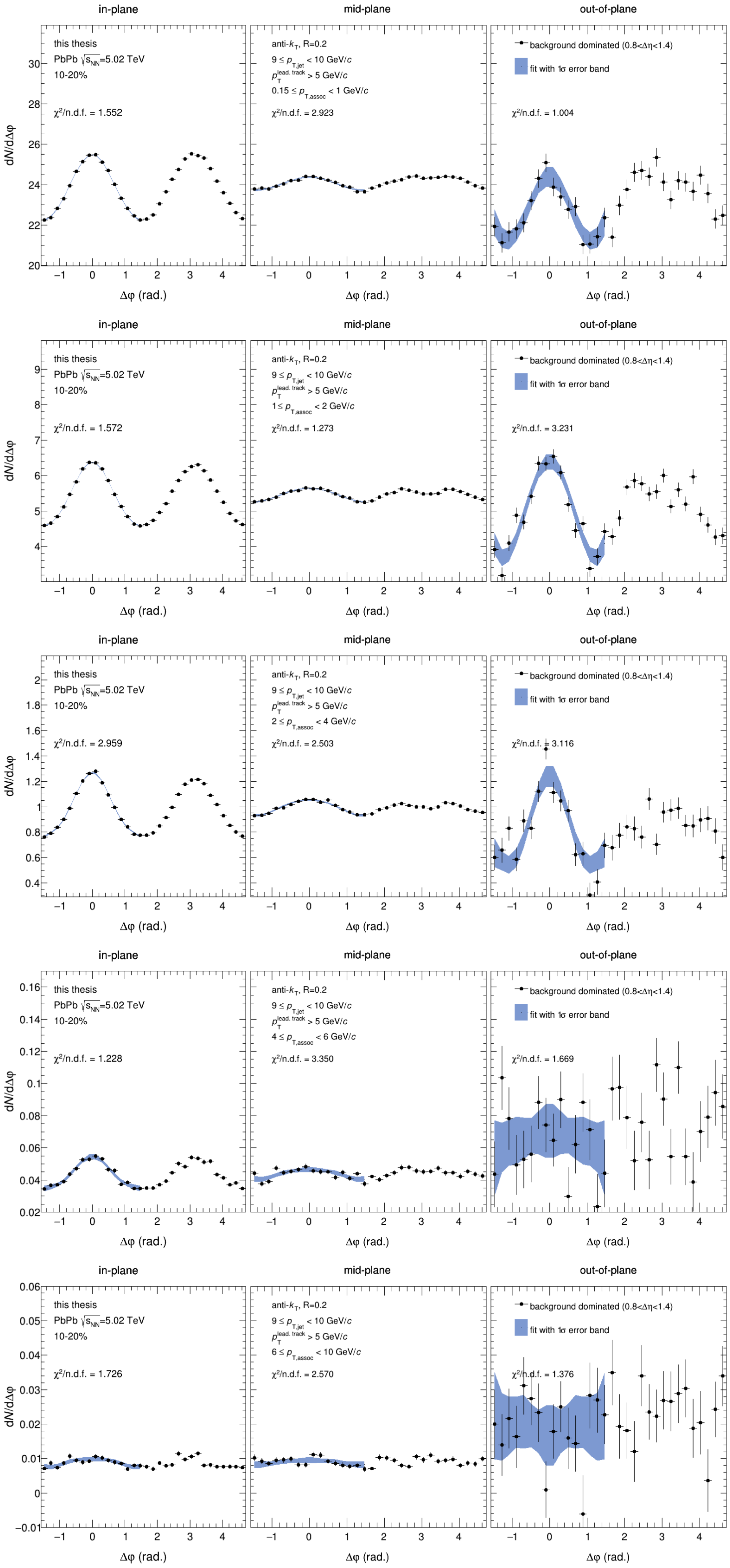

Figure A.19: Example for background subtraction: 10-20%, $9 \le p_{T,jet} < 10$ GeV/c

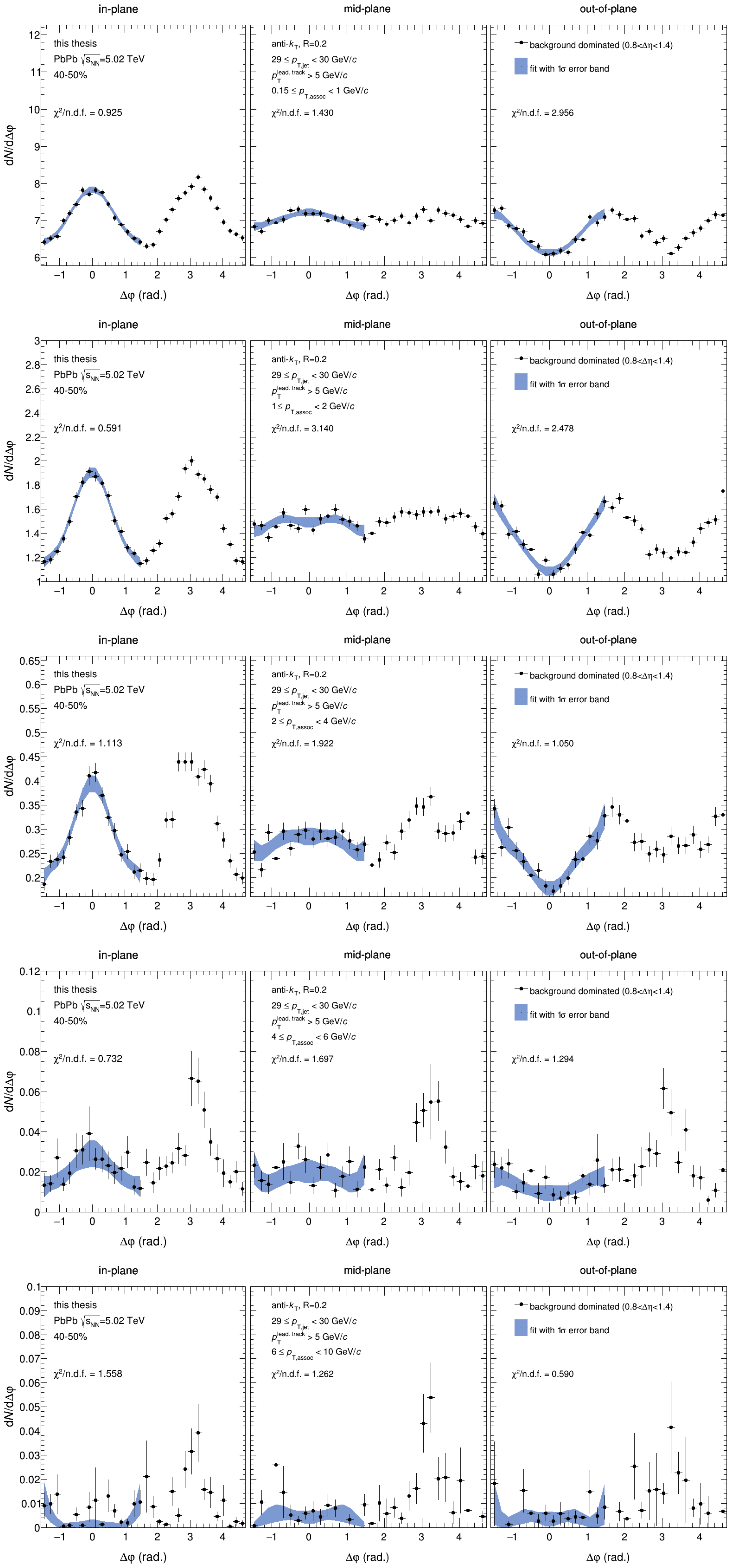

Figure A.20: Example for background subtraction: 40-50%, $29 \le p_{\mathrm{T,jet}} < 30$ GeV/c

A.5 RESPONSE MATRICES, UNFOLDING MATRICES AND UNFOLDED JET p_{T} SPECTRA

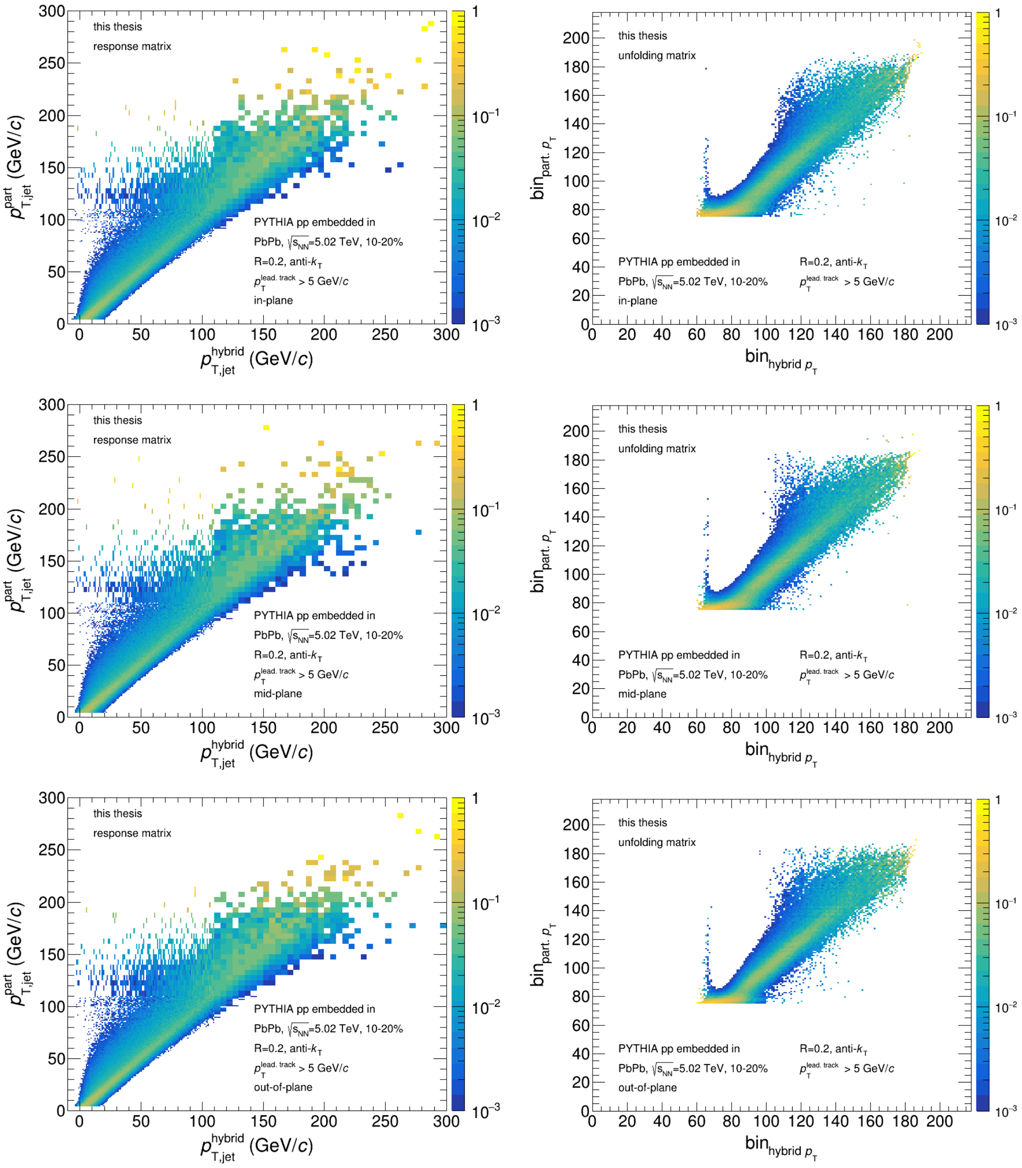

Figure A.21: Response and unfolding matrix for 10-20% centrality

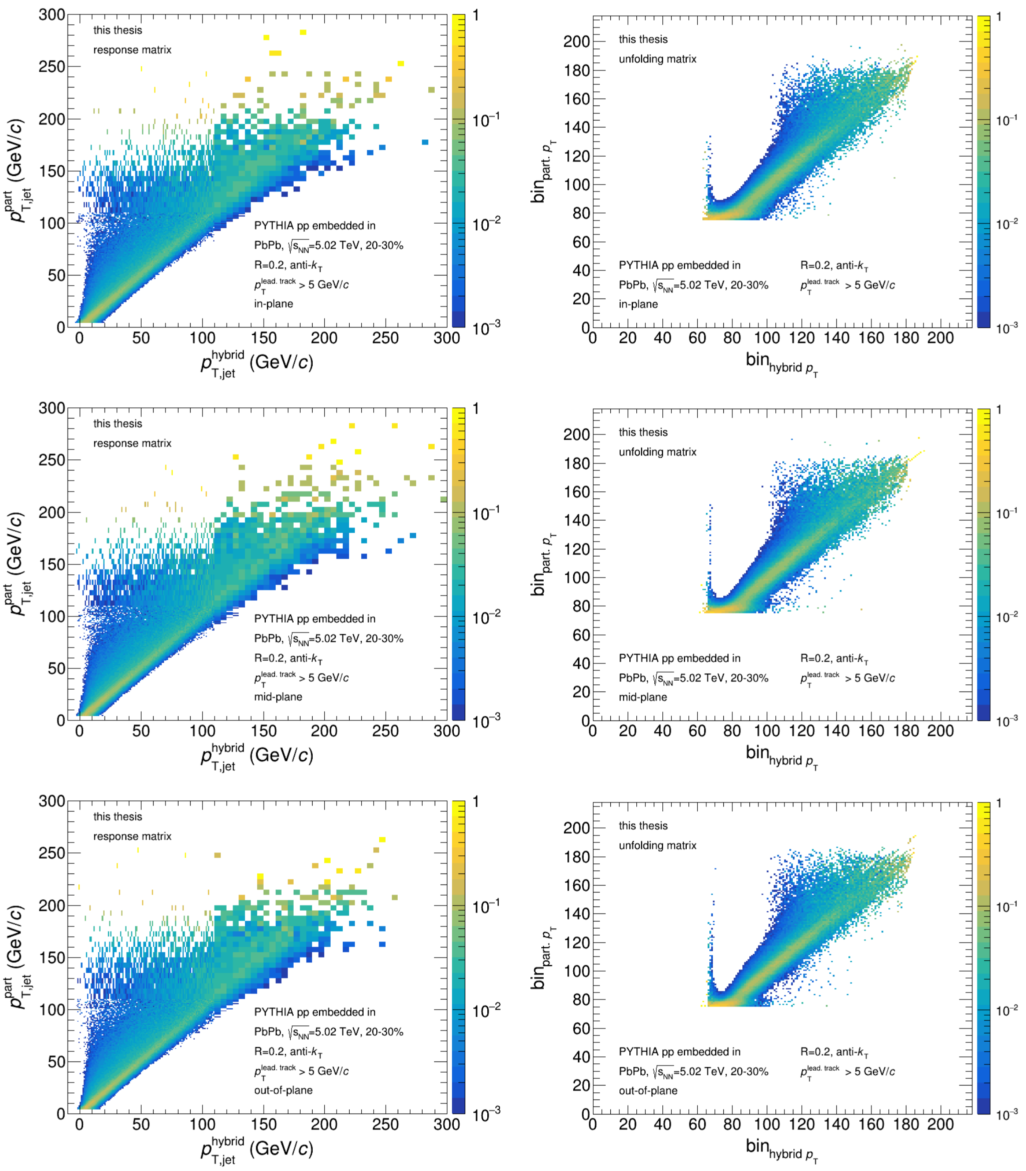

Figure A.22: Response and unfolding matrix for 20-30% centrality

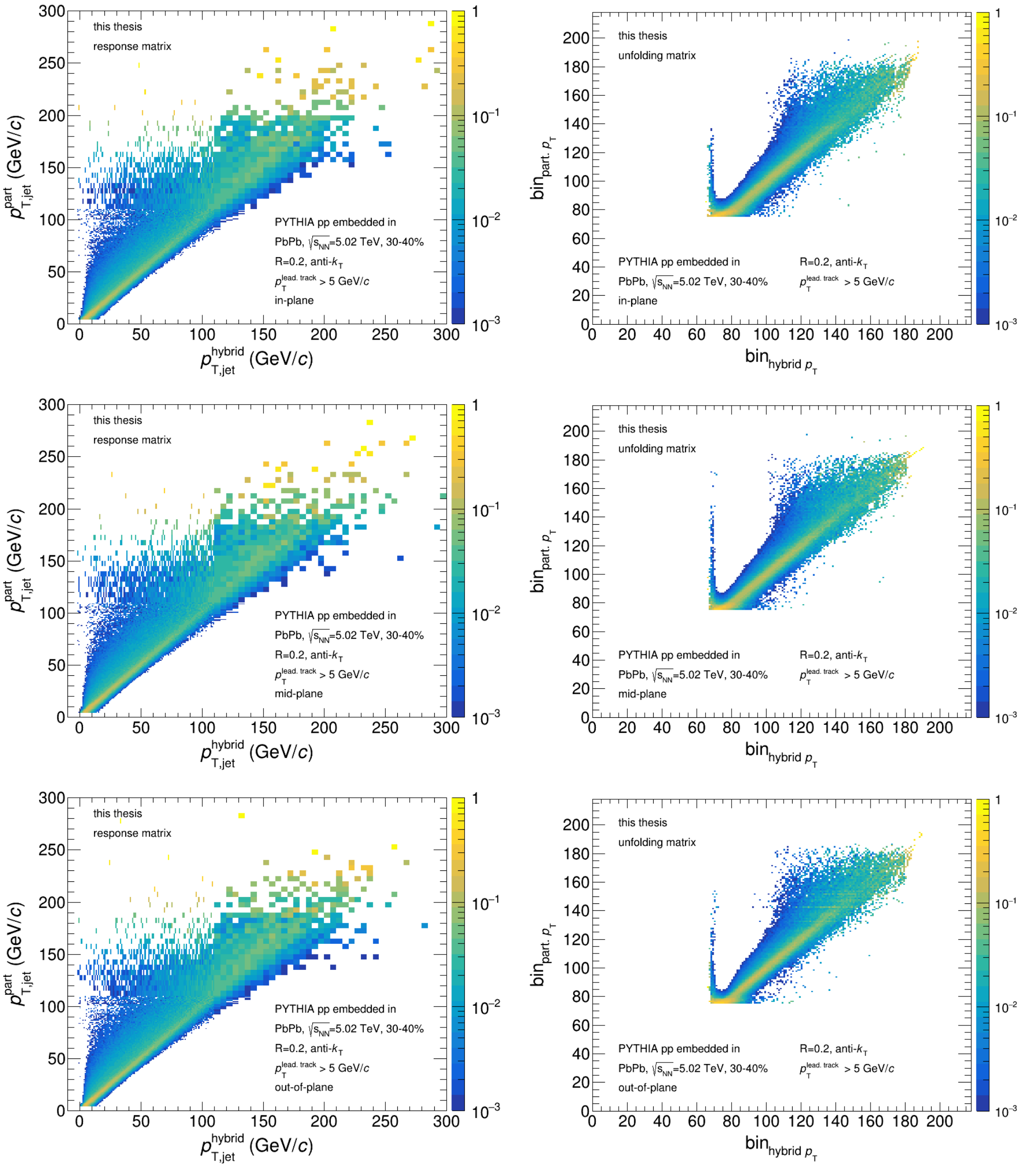

Figure A.23: Response and unfolding matrix for 30-40% centrality

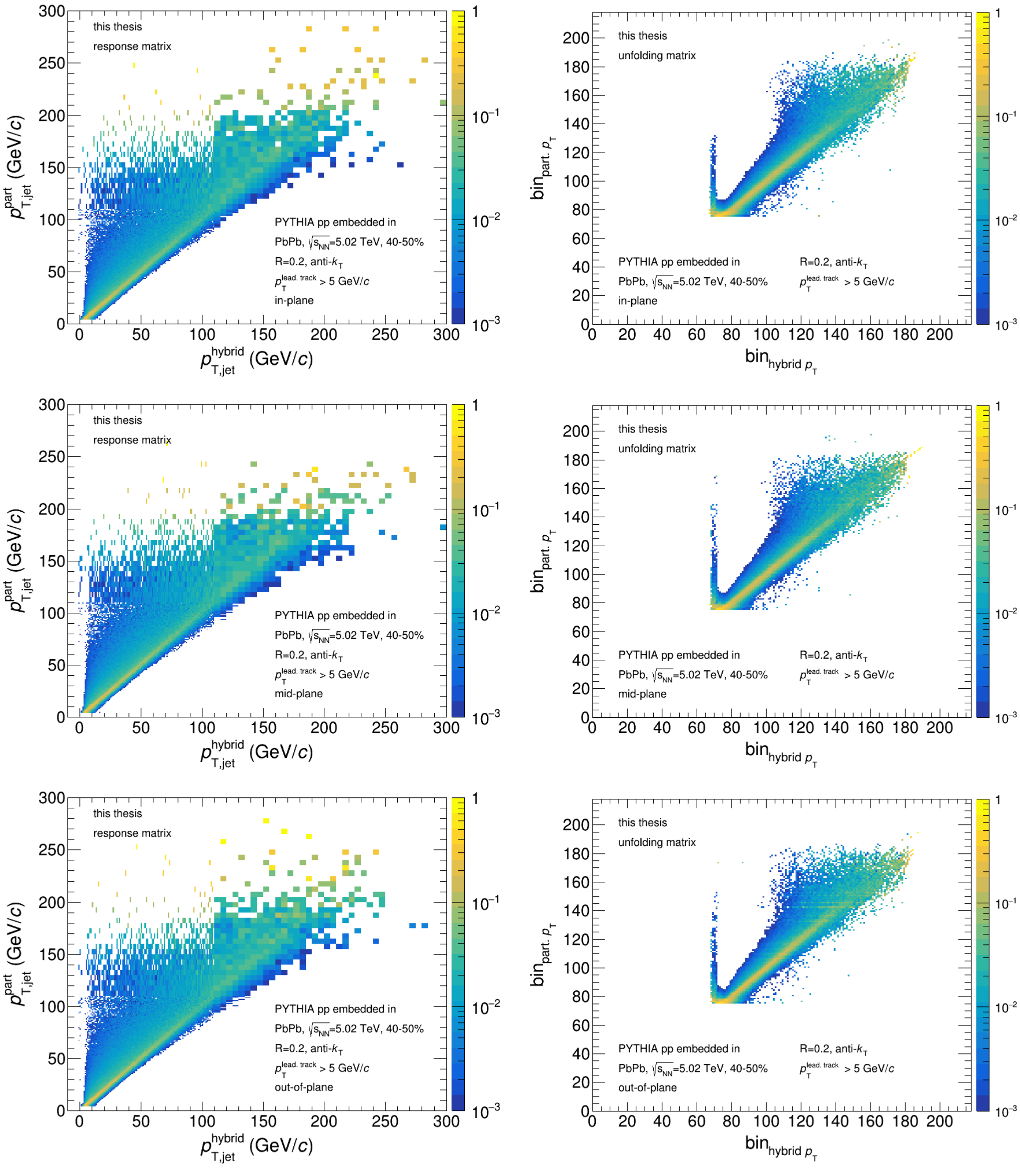

Figure A.24: Response and unfolding matrix for 40-50% centrality

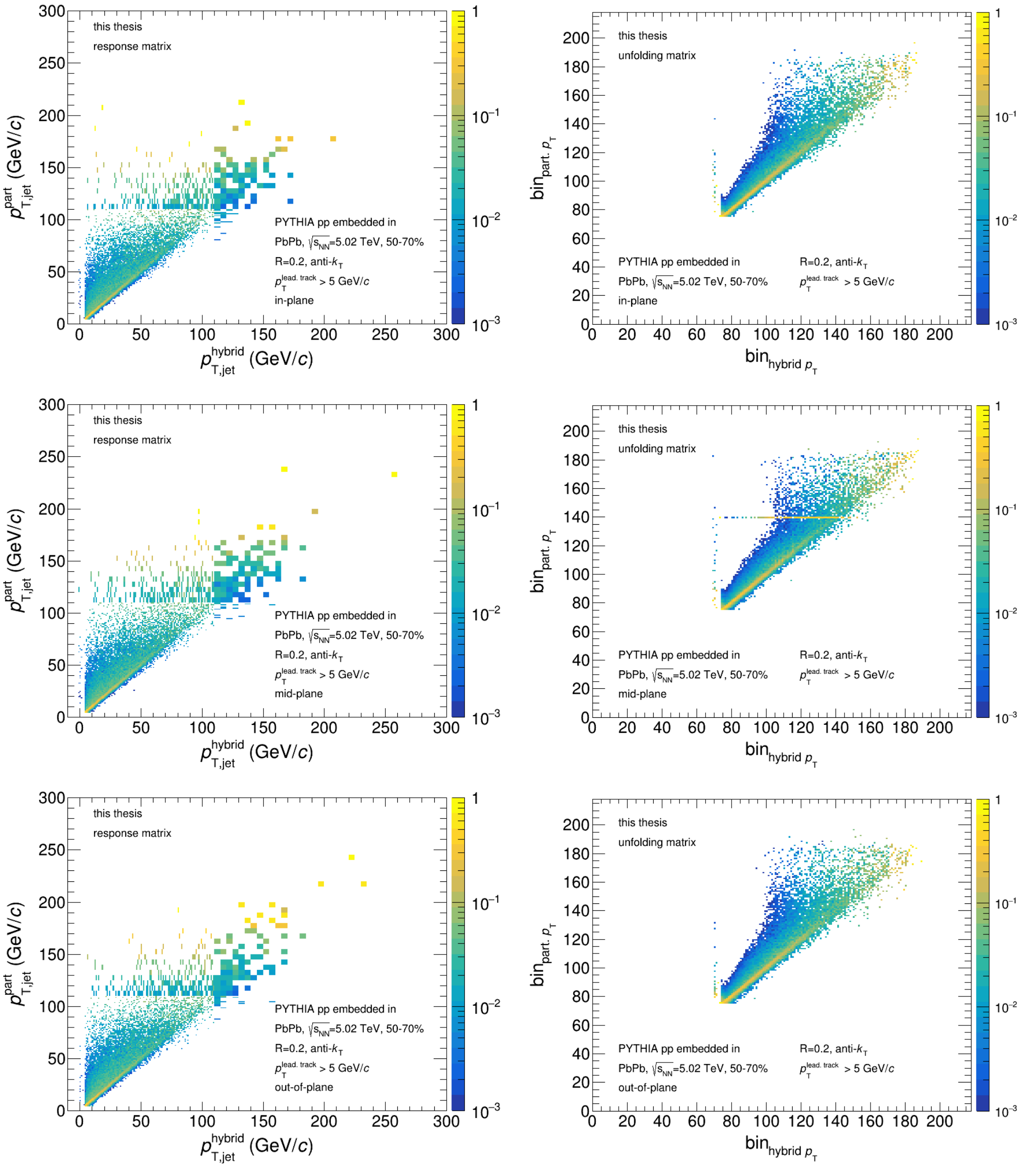

Figure A.25: Response and unfolding matrix for 50-70% centrality

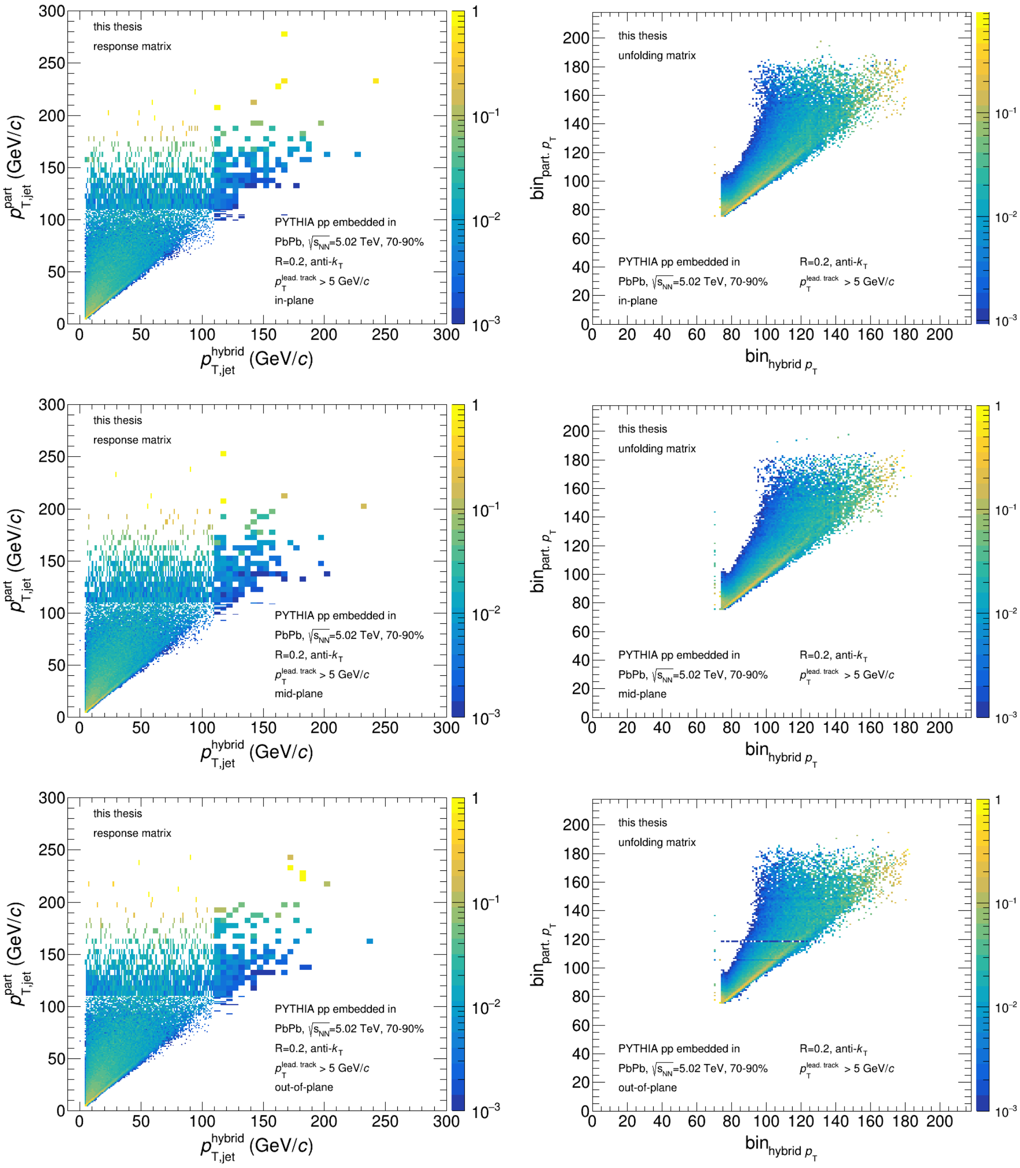

Figure A.26: Response and unfolding matrix for 70-90% centrality

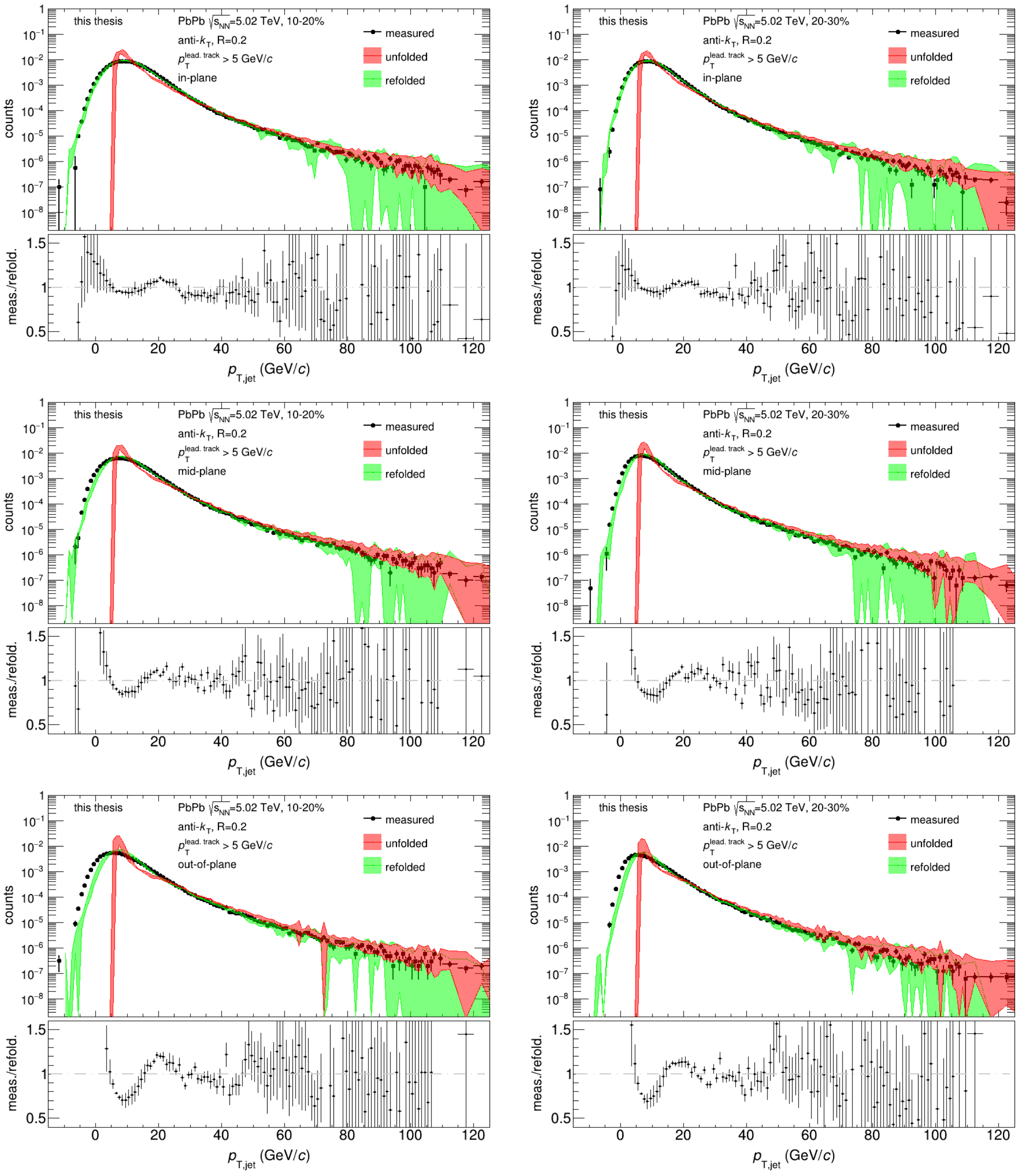

Figure A.27: Un- and refolded spectra for 10-20% and 20-30% centrality

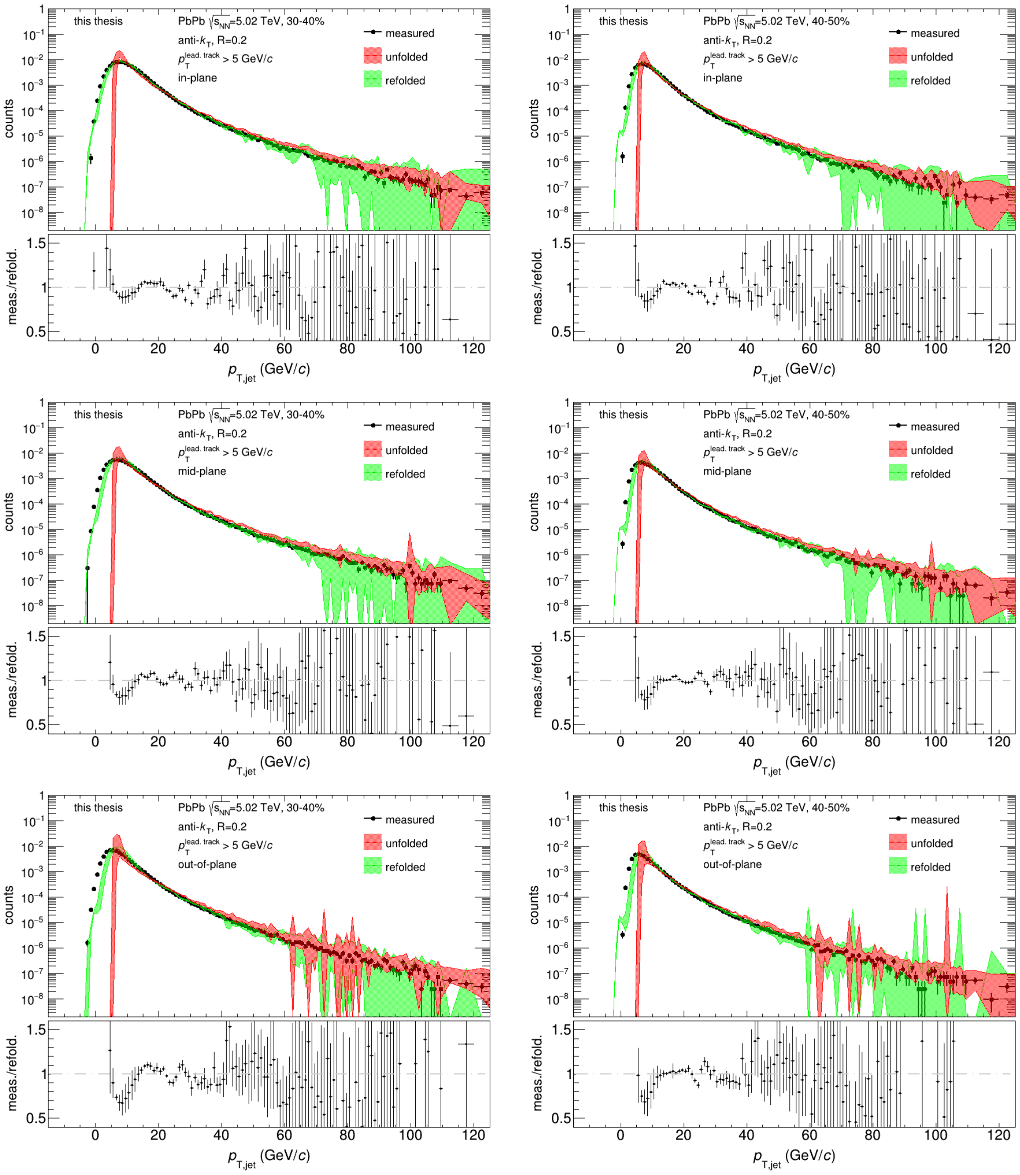

Figure A.28: Un- and refolded spectra for 30-40% and 40-50% centrality

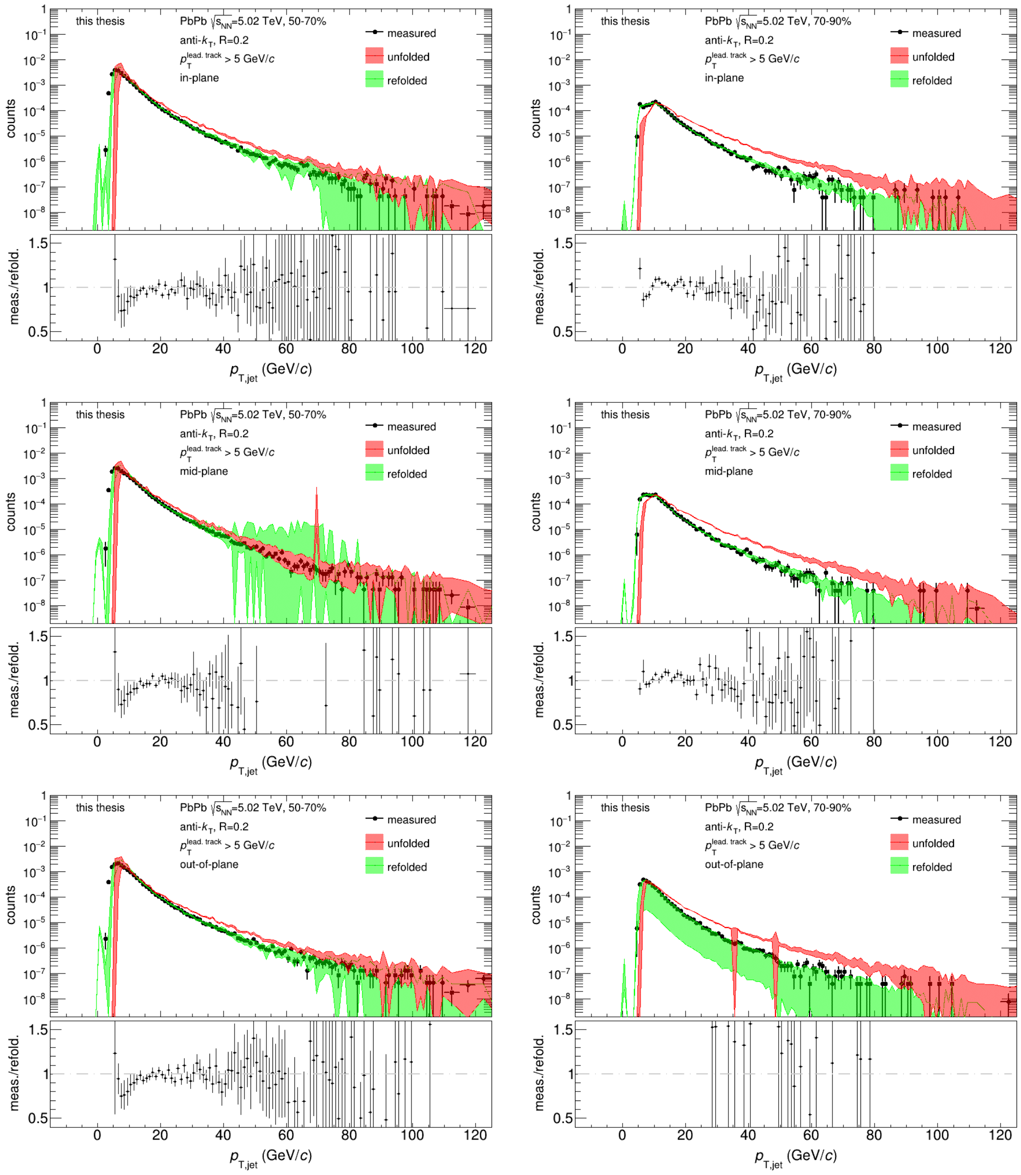

Figure A.29: Un- and refolded spectra for 50-70% and 70-90% centrality

A.6 $\Delta\varphi$ PROJECTIONS OF THE JET-HADRON CORRELATION FUNCTIONS

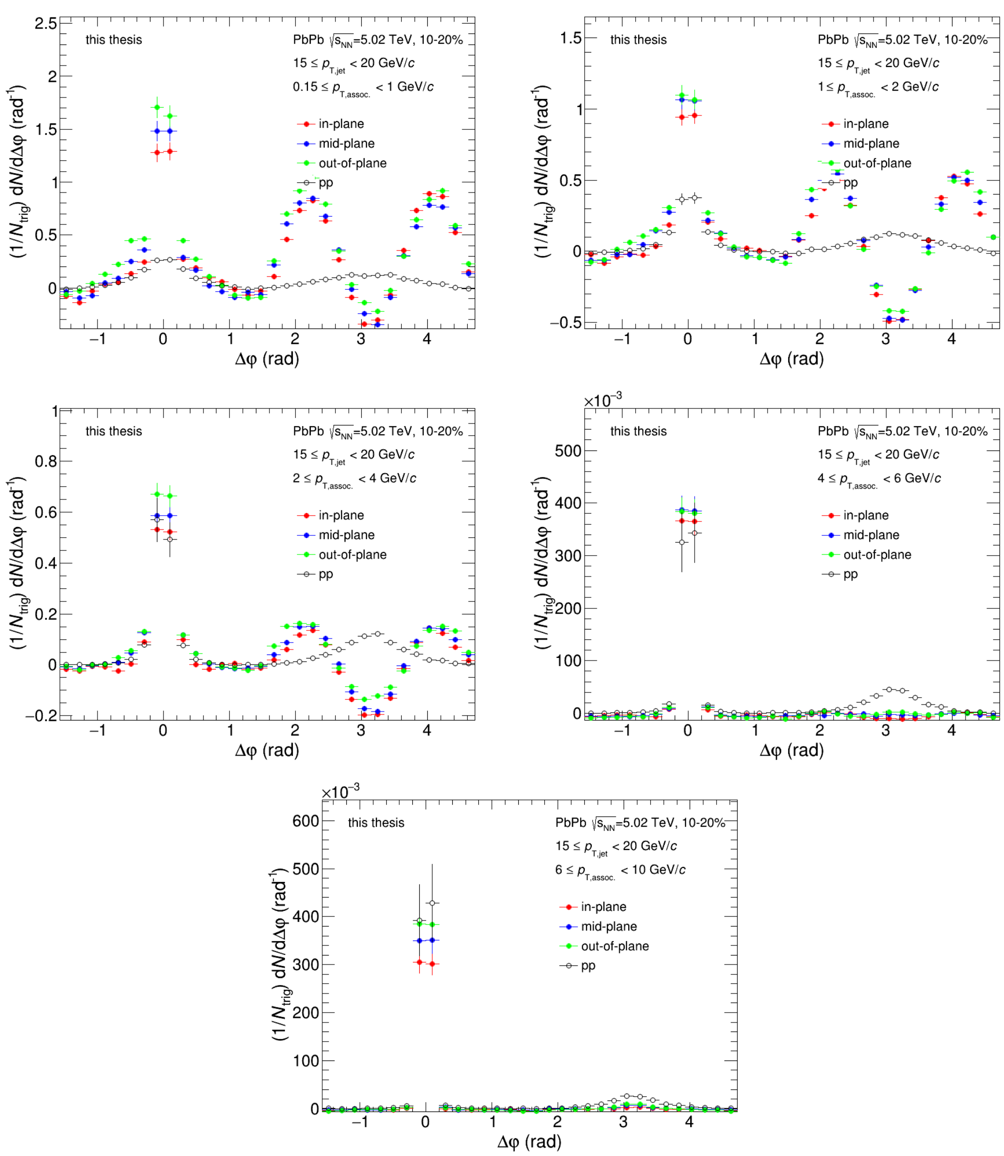

Figure A.30: centrality bin: 10-20%; p_T bin: $15 \leq p_T < 20$ GeV/c

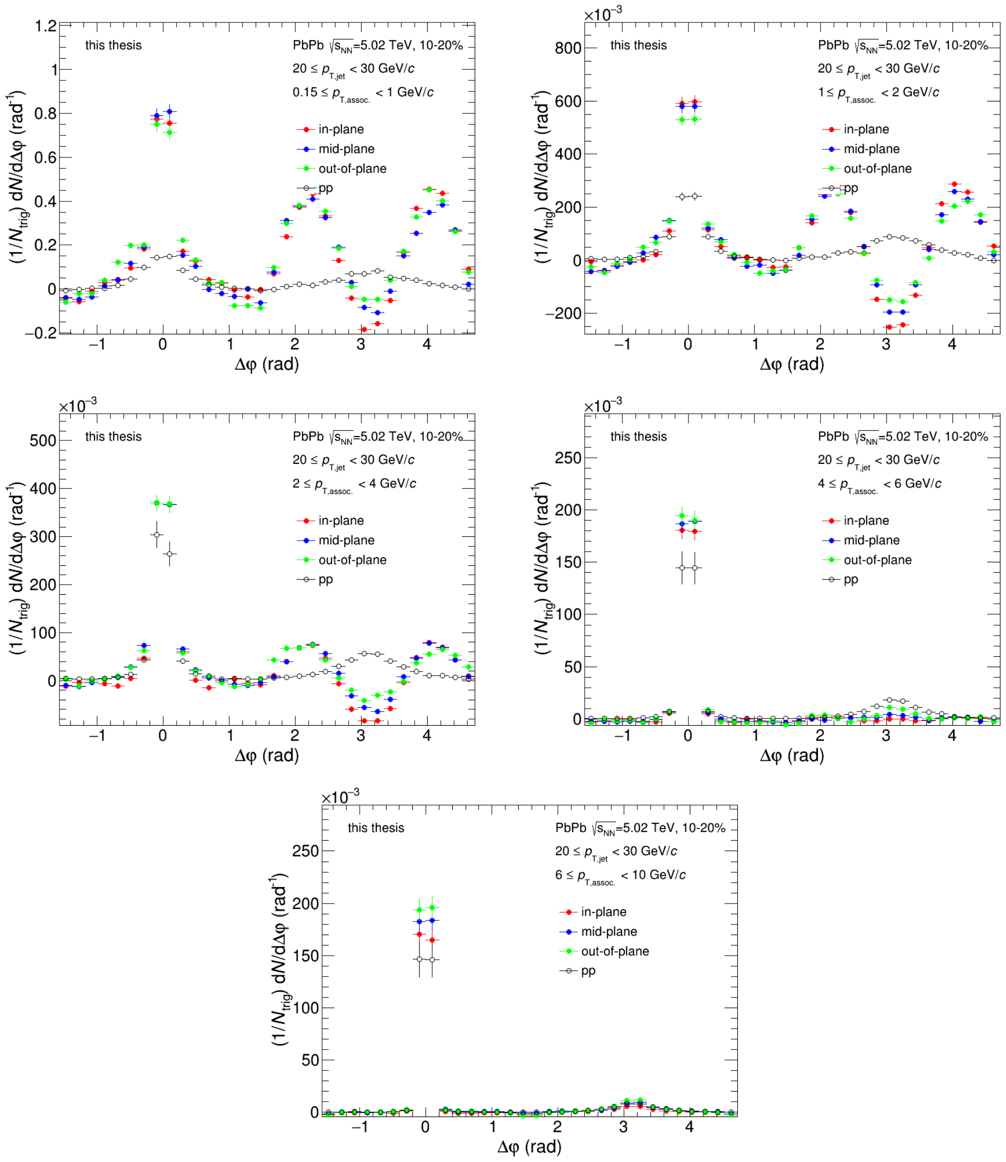

Figure A.31: centrality bin: 10-20%; p_T bin: $20 \leq p_T < 30$ GeV/c

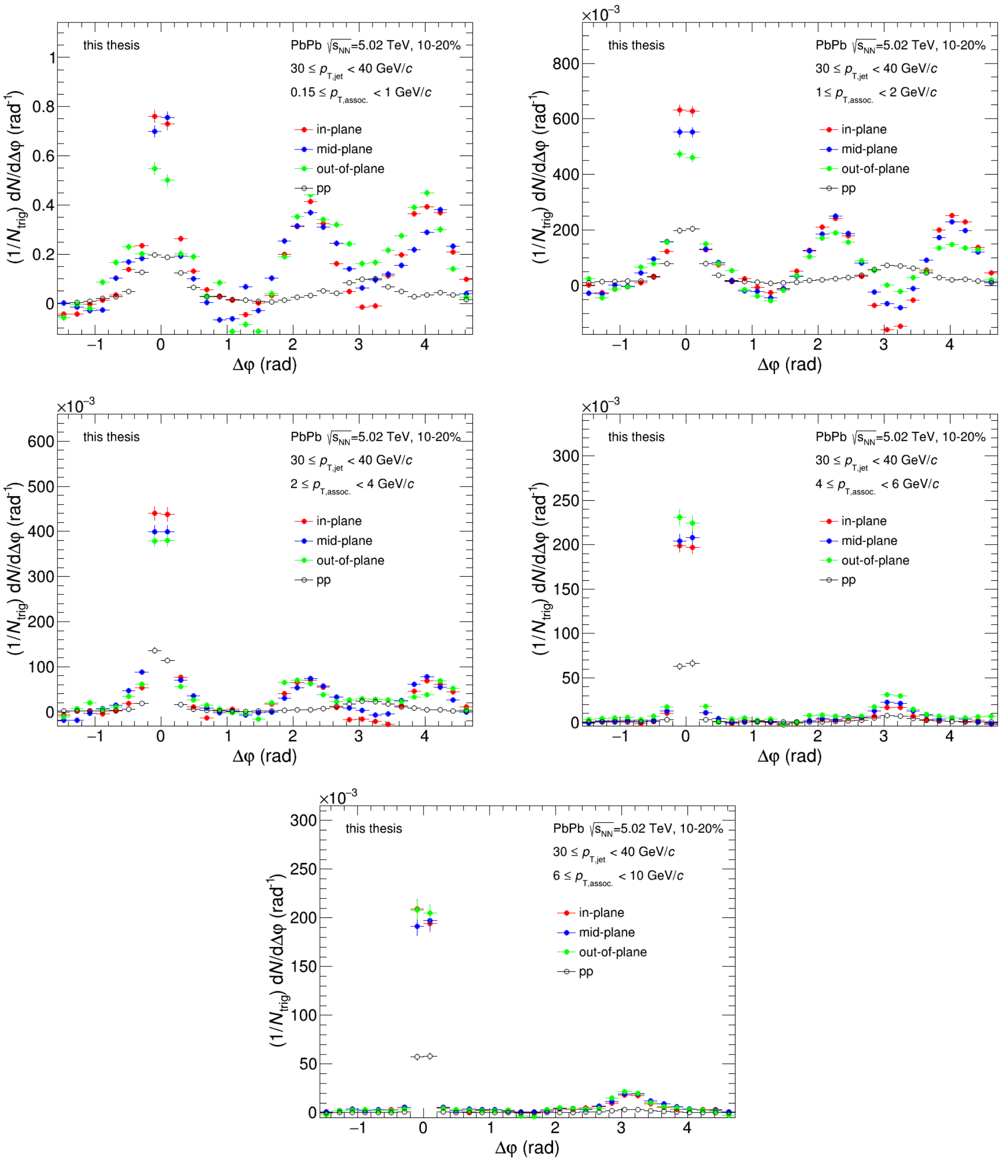

Figure A.32: centrality bin: 10-20%; p_T bin: $30 \leq p_T < 40$ GeV/c

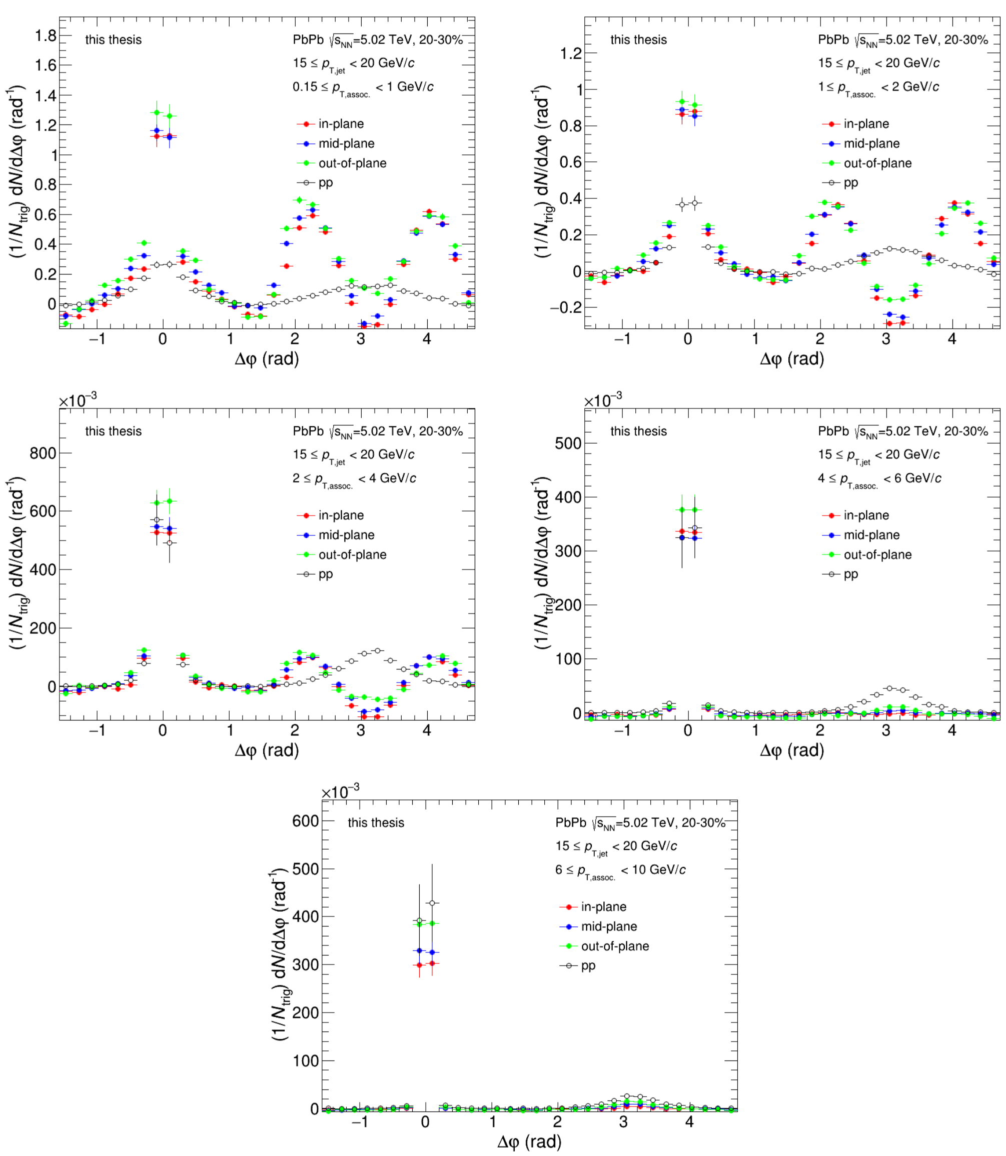

Figure A.33: centrality bin: 20-30%; p_T bin: $15 \leq p_T < 20$ GeV/c

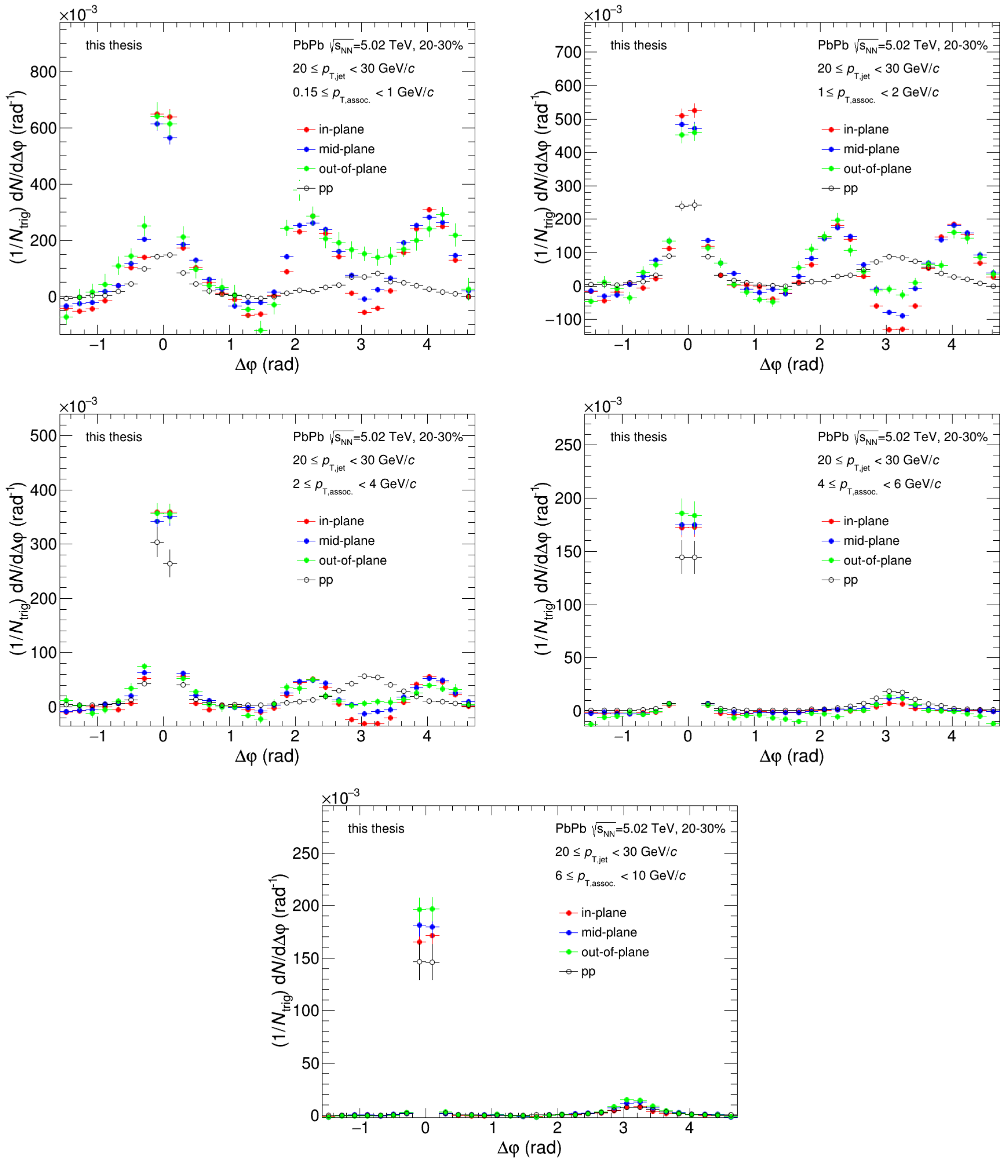

Figure A.34: centrality bin: 20-30%; p_T bin: $20 \leq p_T < 30$ GeV/c

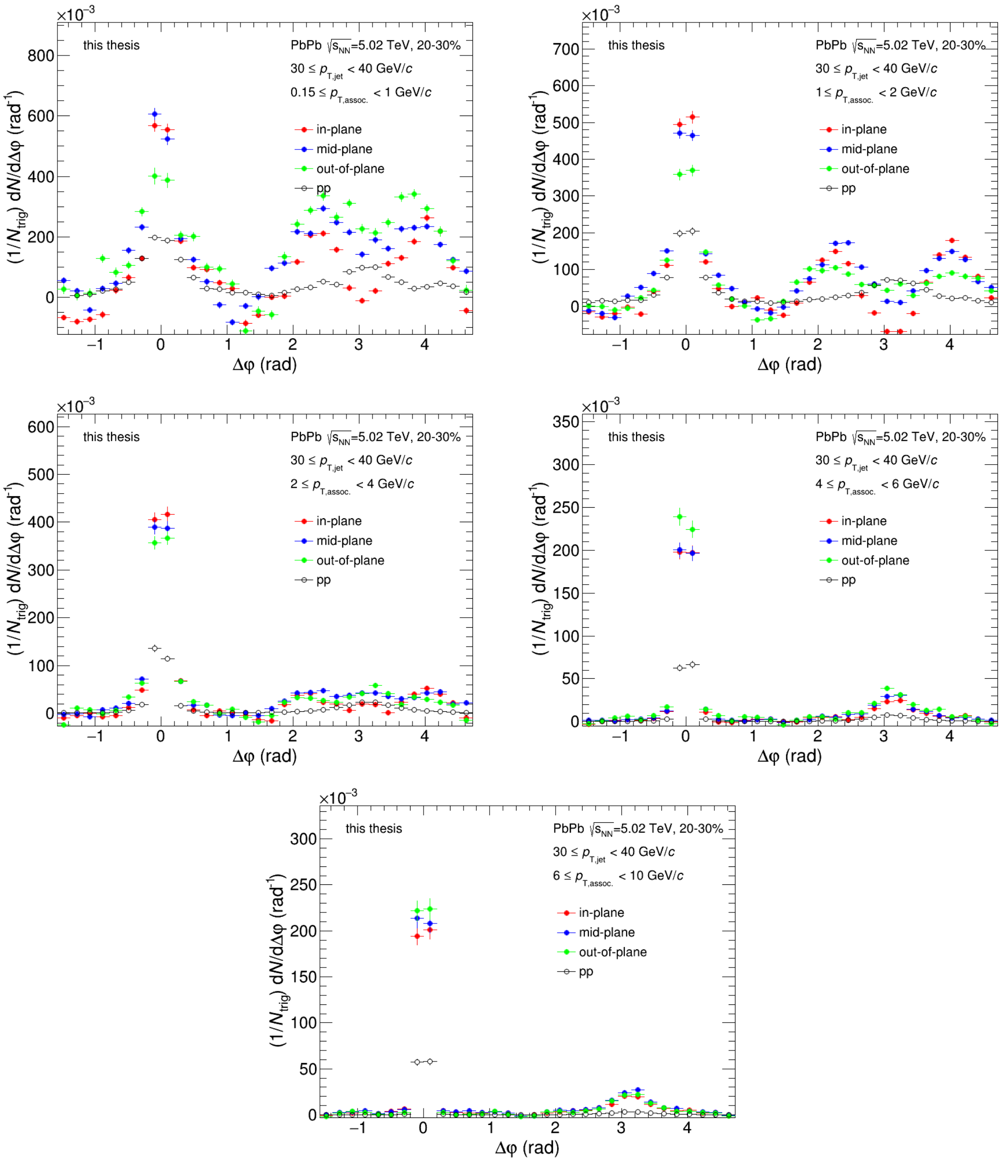

Figure A.35: centrality bin: 20-30%; p_T bin: $30 \leq p_T < 40$ GeV/c

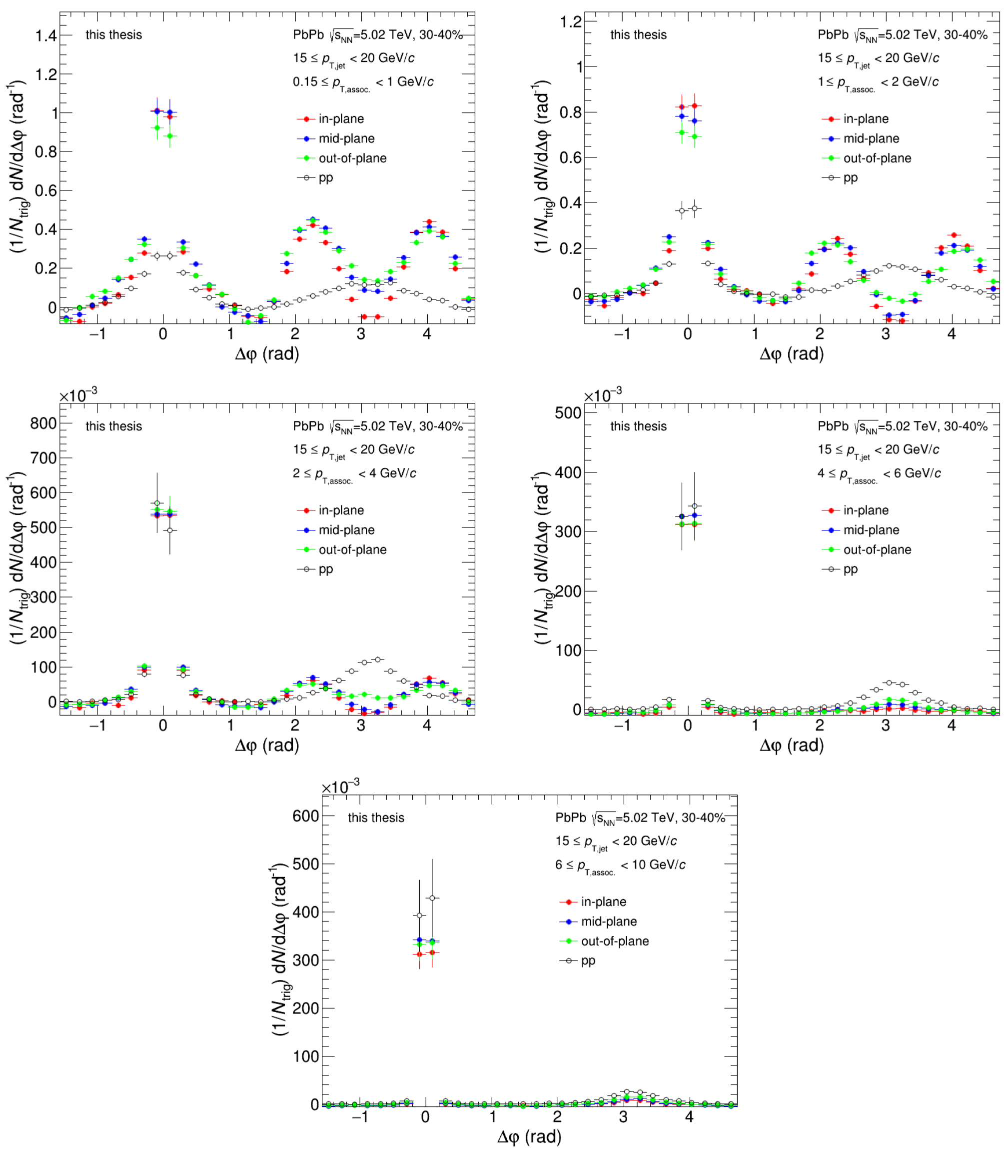

Figure A.36: centrality bin: 30-40%; p_{T} bin: $15 \leq p_{\mathrm{T}} < 20$ GeV/c

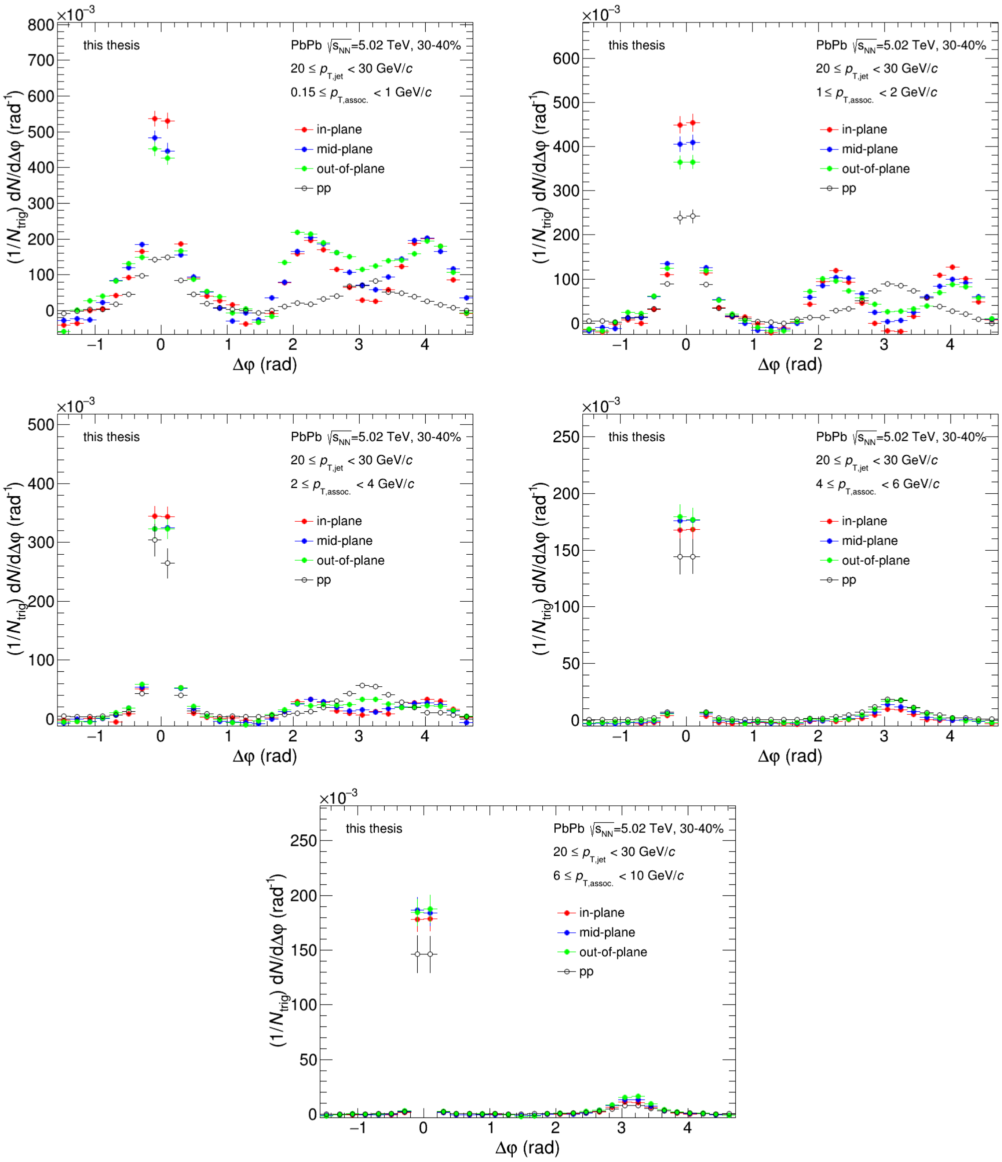

Figure A.37: centrality bin: 30-40%; p_T bin: $20 \le p_T < 30$ GeV/c

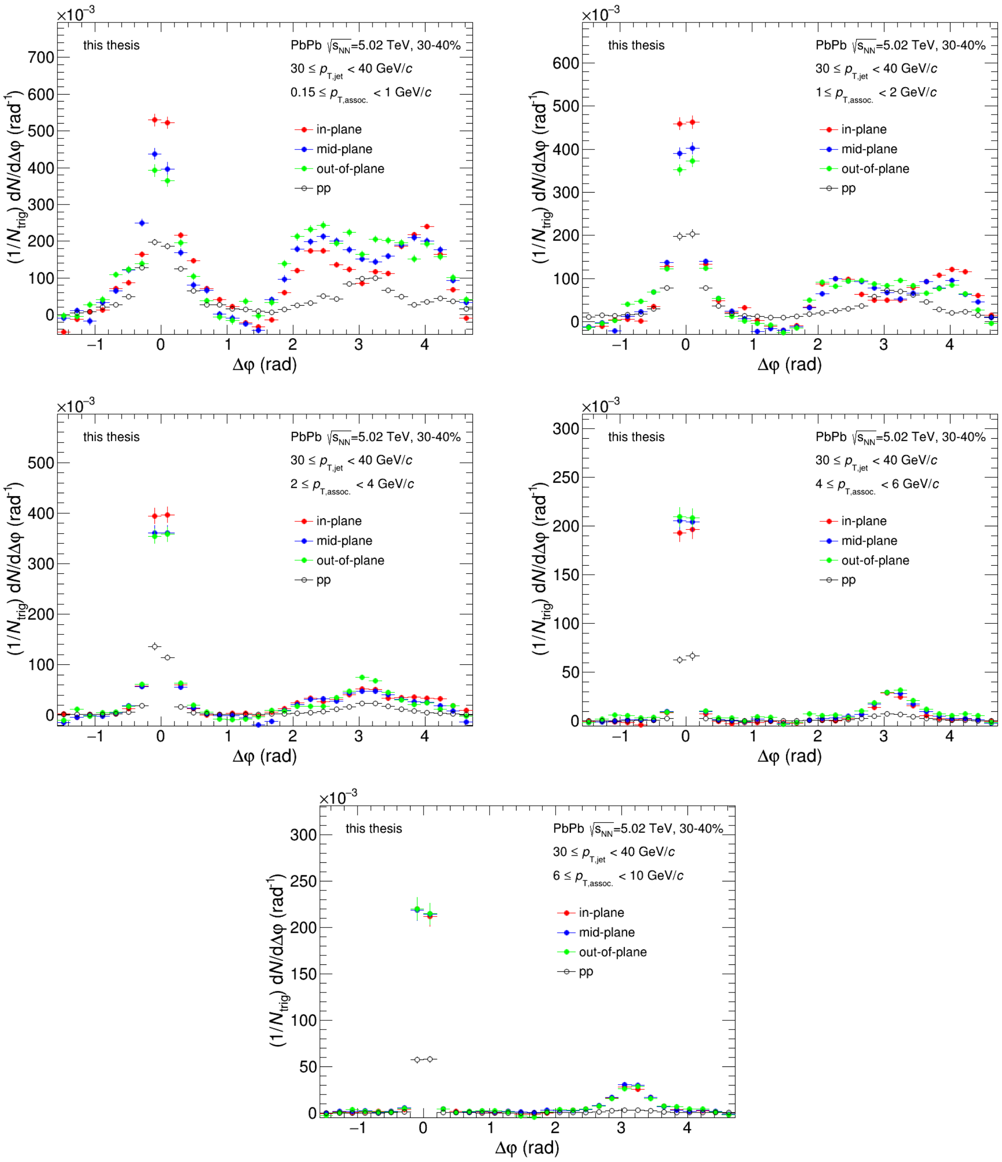

Figure A.38: centrality bin: 30-40%; p_T bin: $30 \leq p_\mathrm{T} < 40$ GeV/c

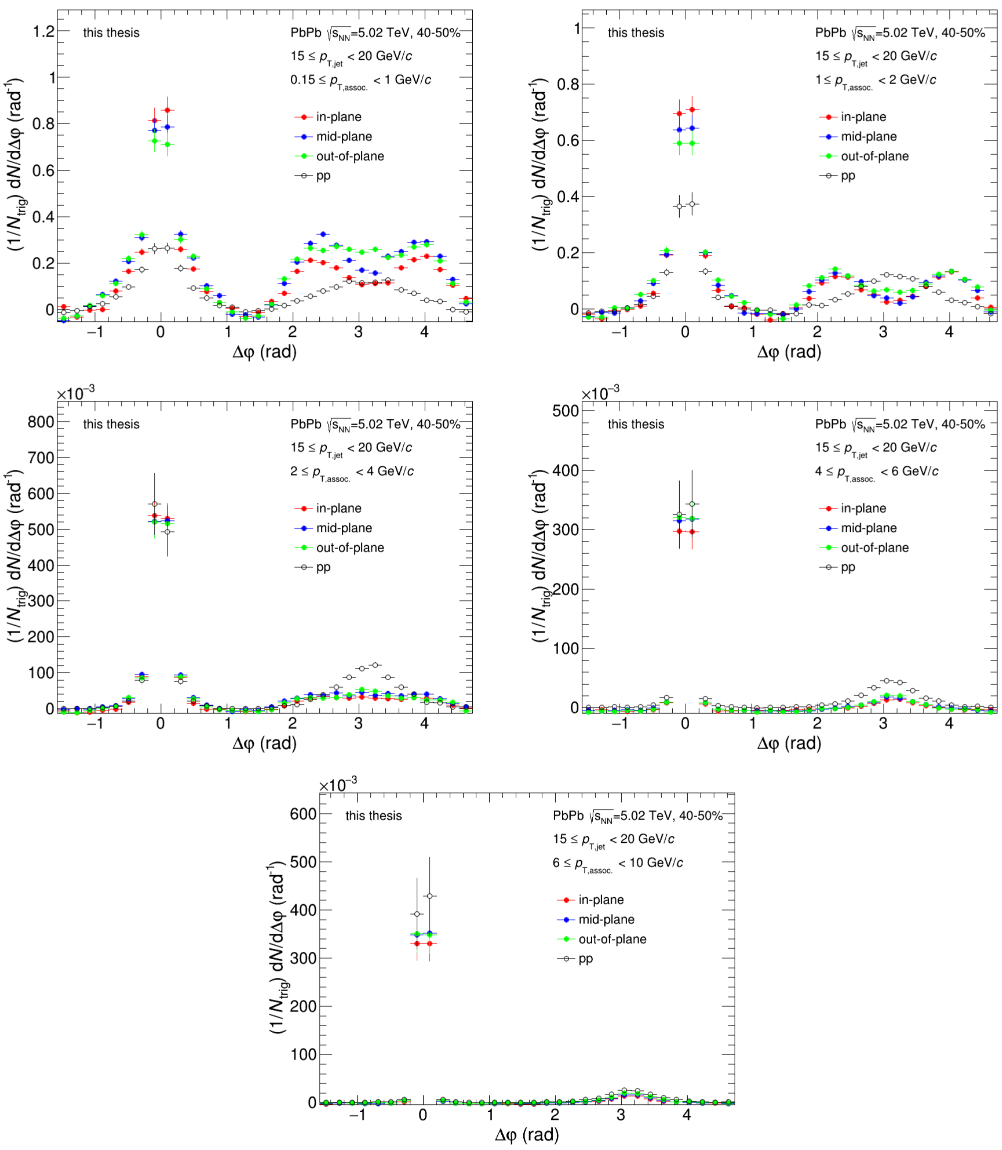

Figure A.39: centrality bin: 40-50%; p_T bin: $15 \leq p_T < 20$ GeV/c

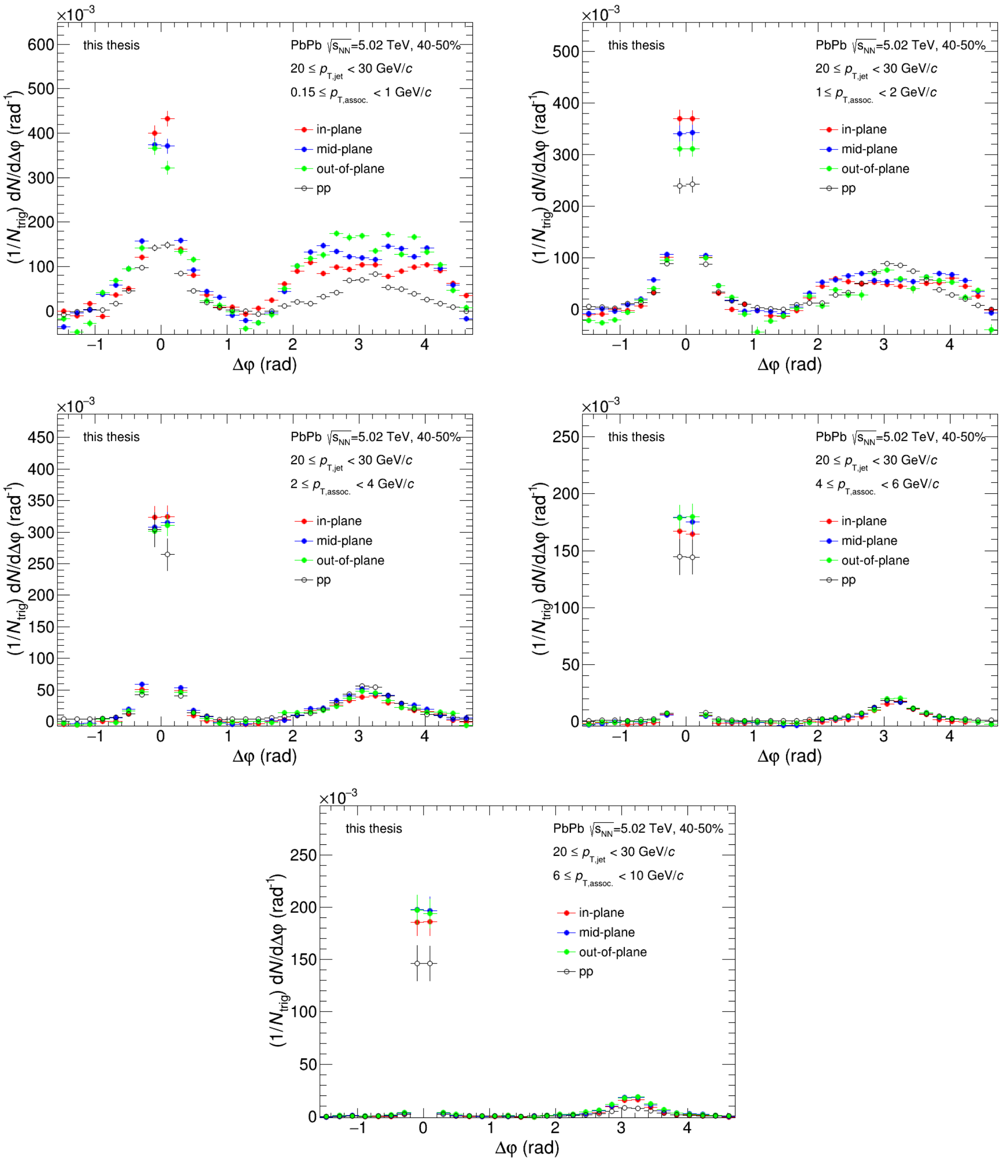

Figure A.40: centrality bin: 40-50%; p_T bin: $20 \leq p_T < 30$ GeV/c

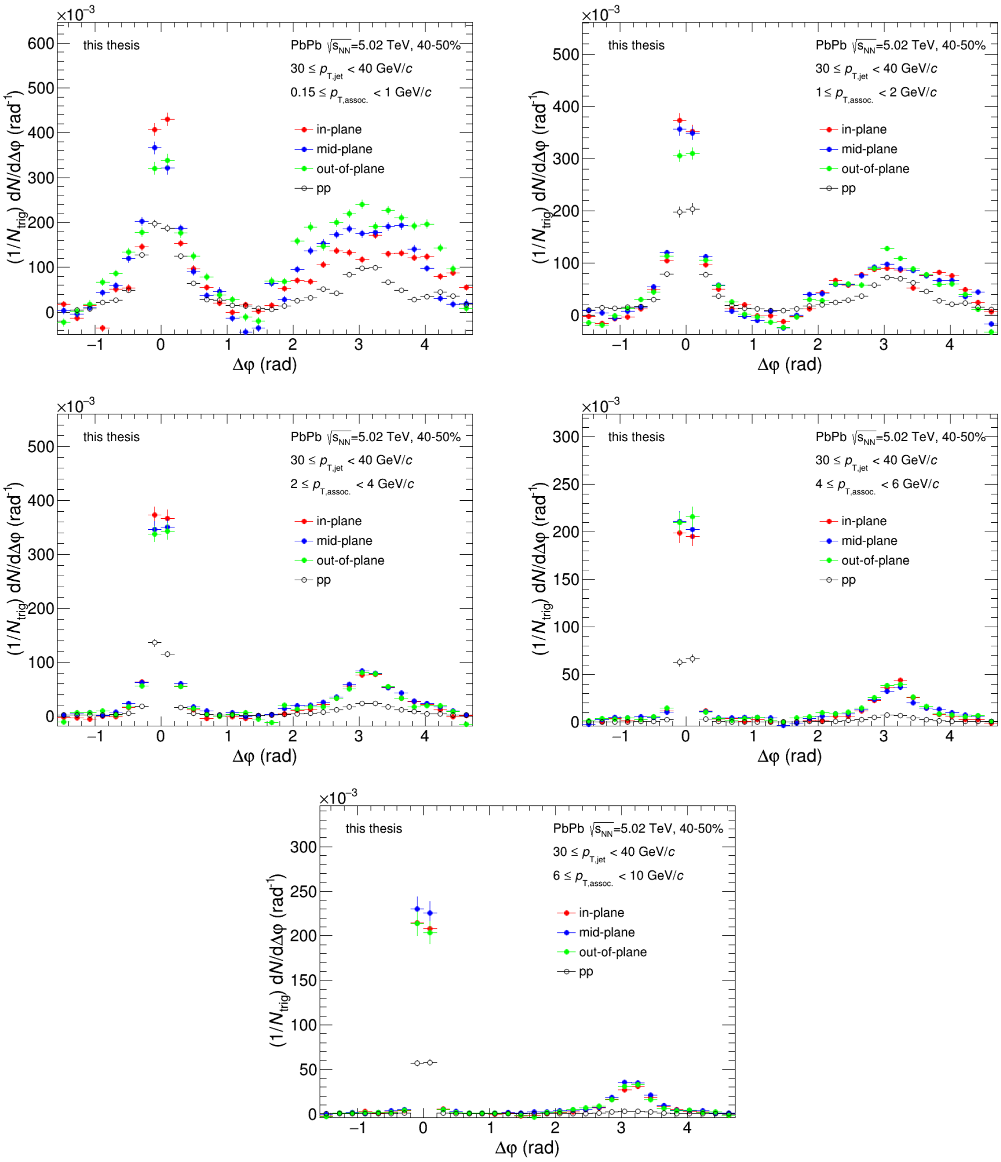

Figure A.41: centrality bin: 40-50%; p_T bin: $30 \leq p_T < 40$ GeV/c

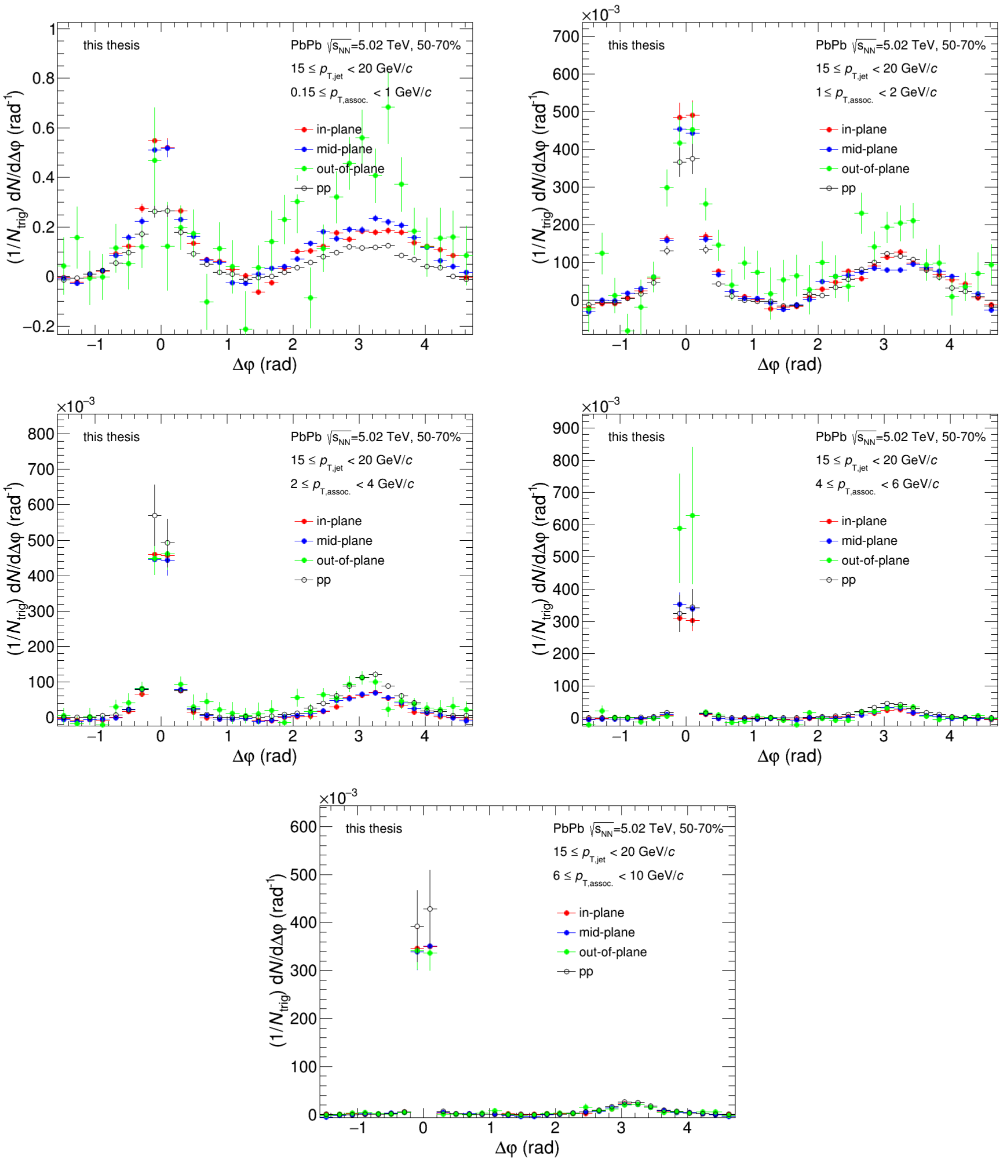

Figure A.42: centrality bin: 50-70%; p_T bin: $15 \leq p_T < 20$ GeV/c

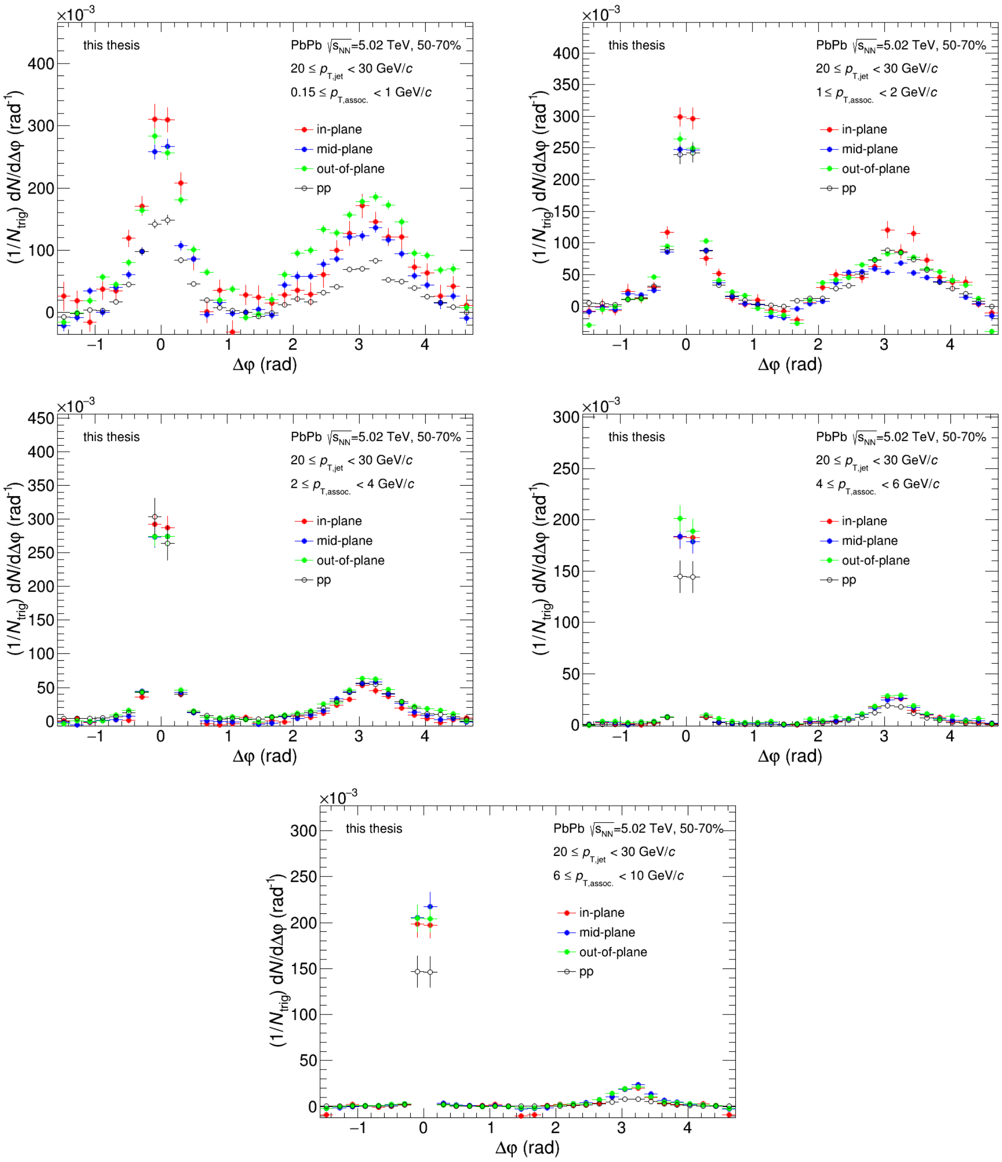

Figure A.43: centrality bin: 50-70%; p_{T} bin: $20 \leq p_{\mathrm{T}} < 30$ GeV/c

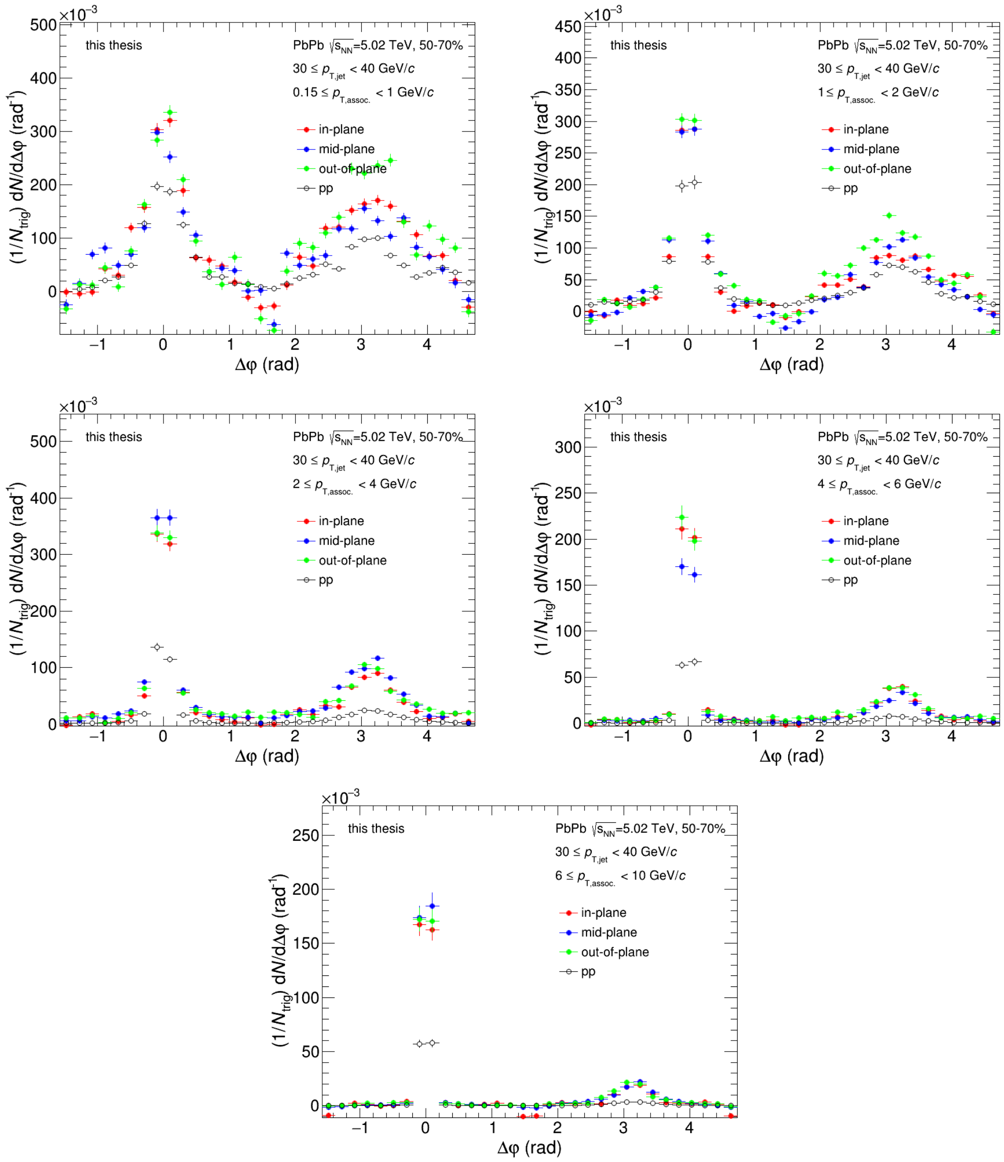

Figure A.44: centrality bin: 50-70%; p_T bin: $30 \leq p_T < 40$ GeV/c

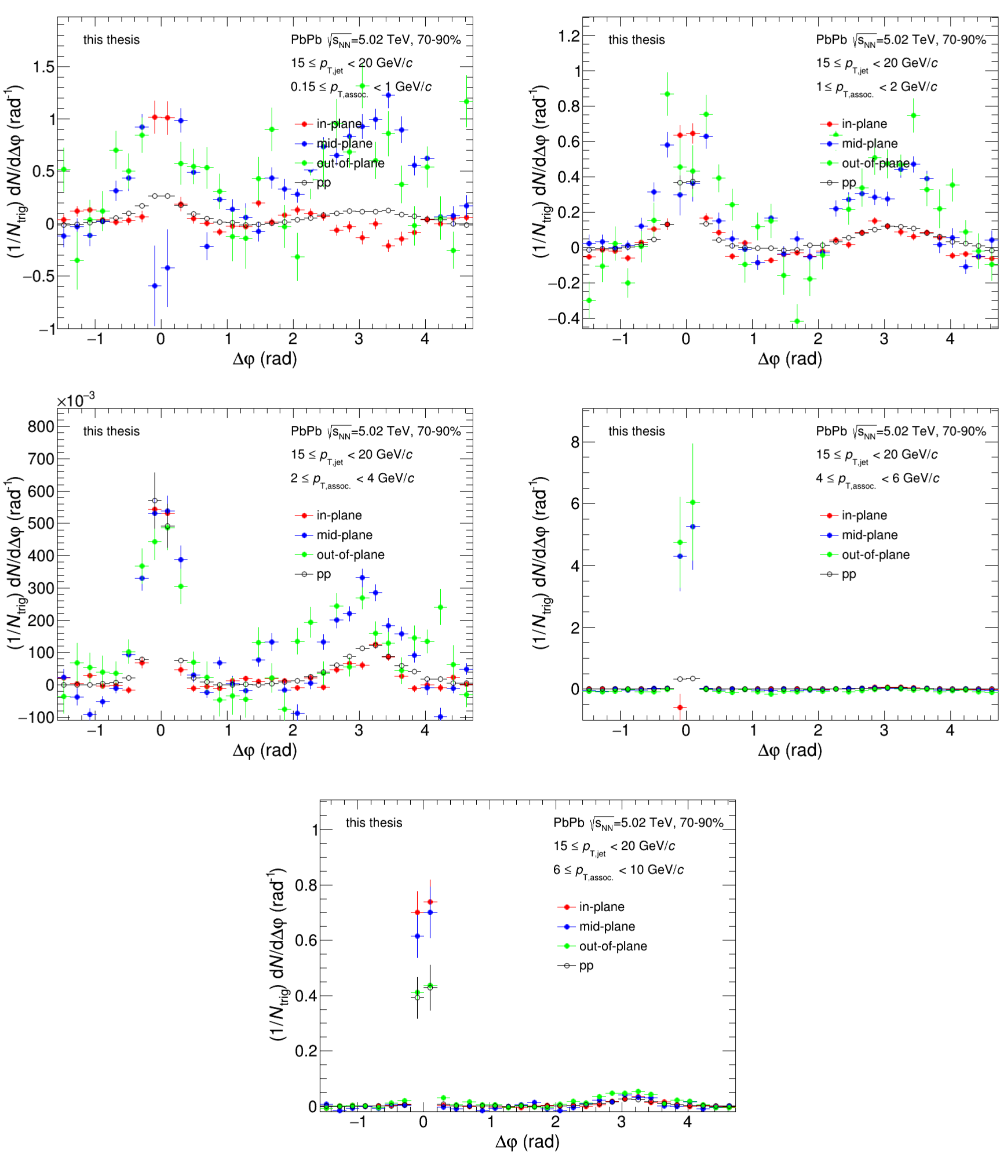

Figure A.45: centrality bin: 70-90%; p_T bin: $15 \le p_T < 20$ GeV/c

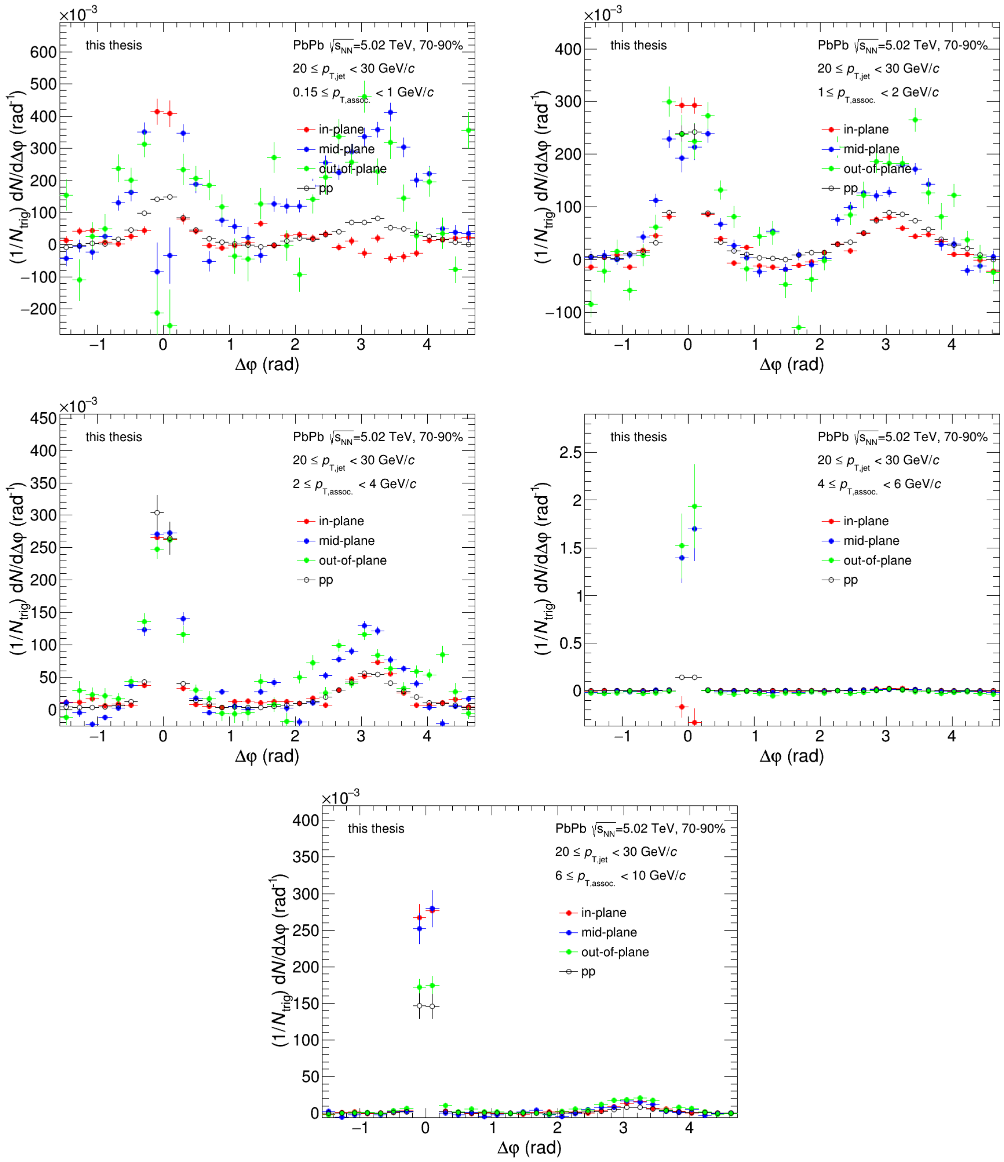

Figure A.46: centrality bin: 70-90%; p_T bin: $20 \leq p_\mathrm{T} < 30$ GeV/c

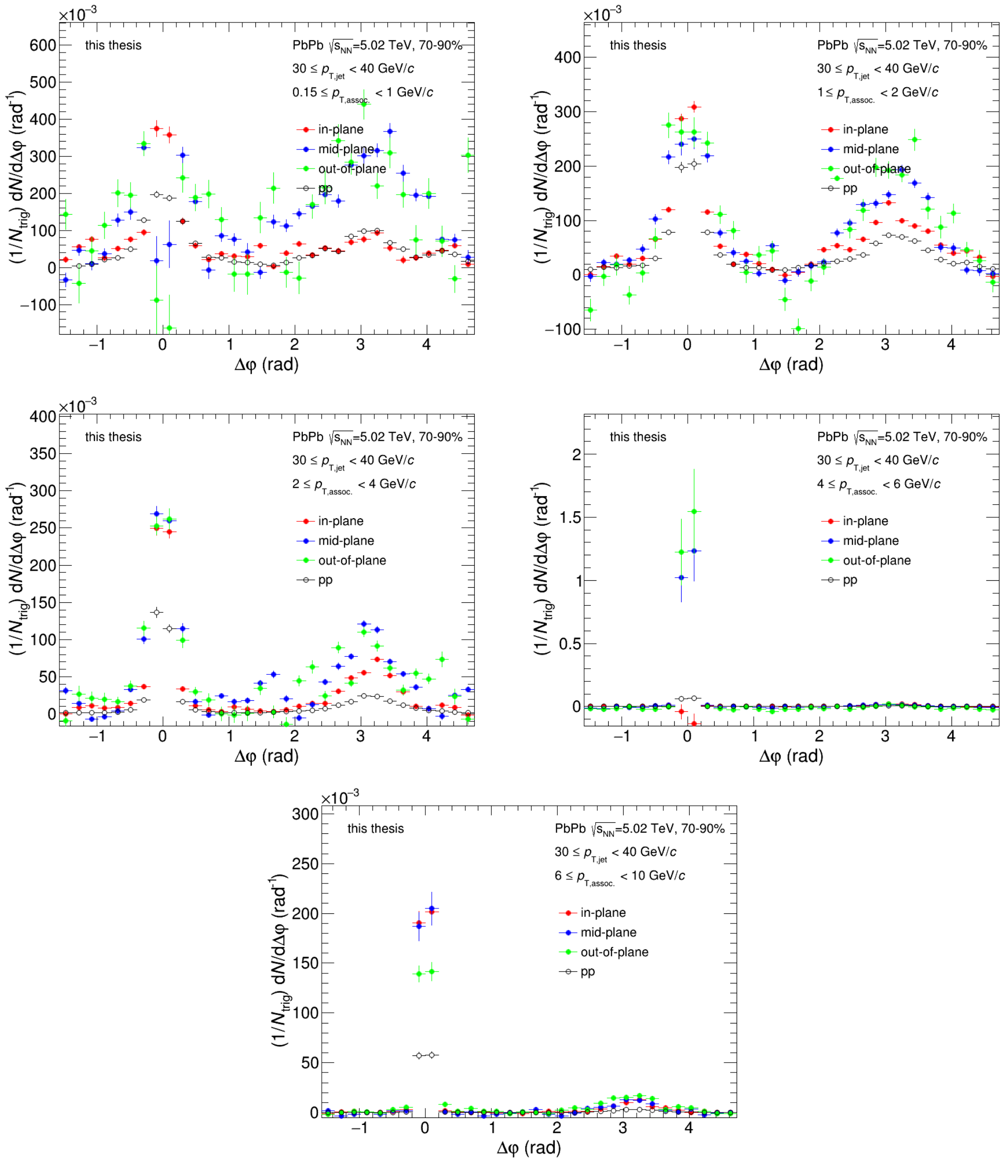

Figure A.47: centrality bin: 70-90%; p_{T} bin: $30 \leq p_{\mathrm{T}} < 40$ GeV/c

A.7 YIELDS AND I_{AA}

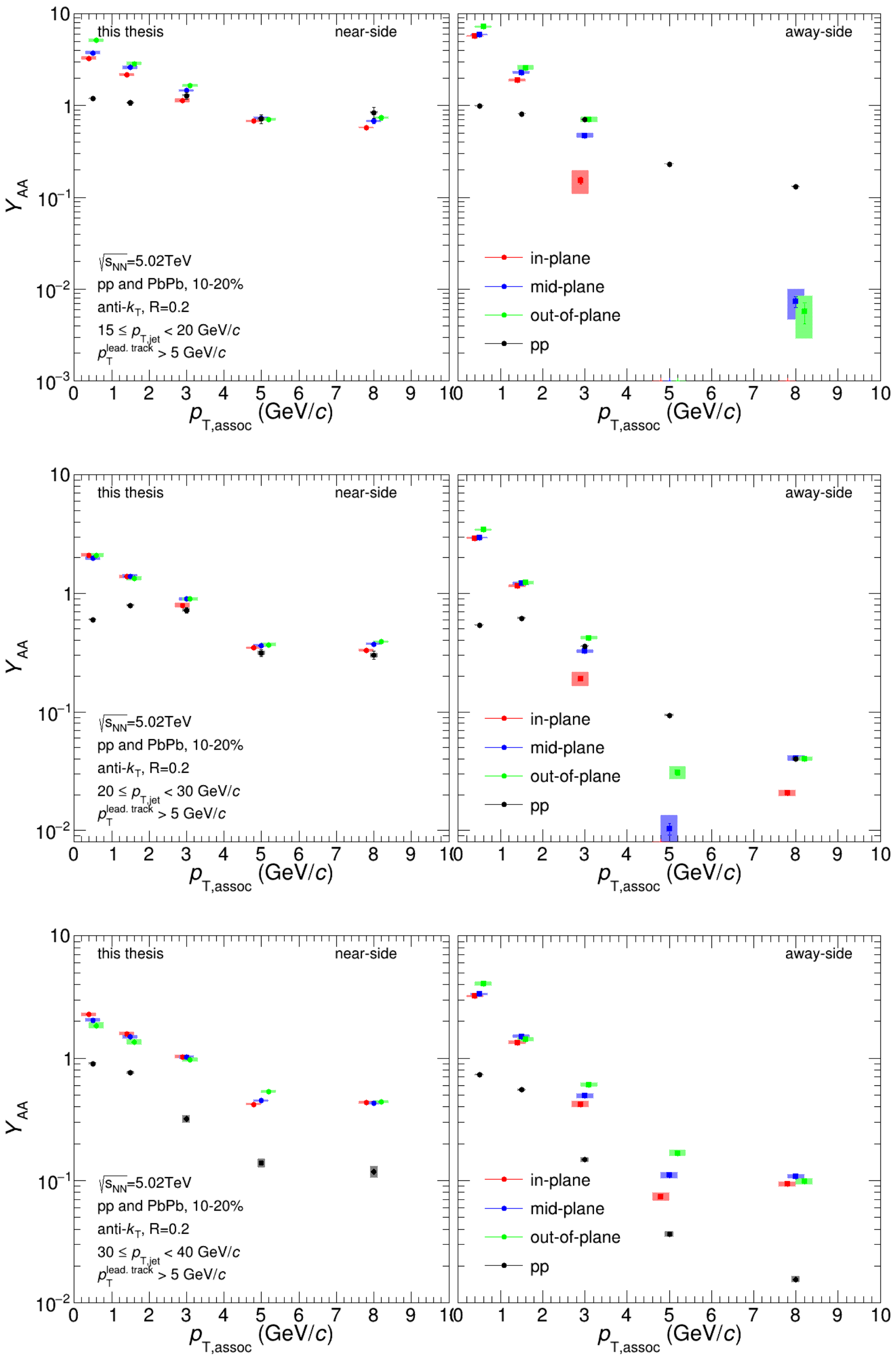

Figure A.48: Per-trigger yields for 10-20% centrality PbPb and pp

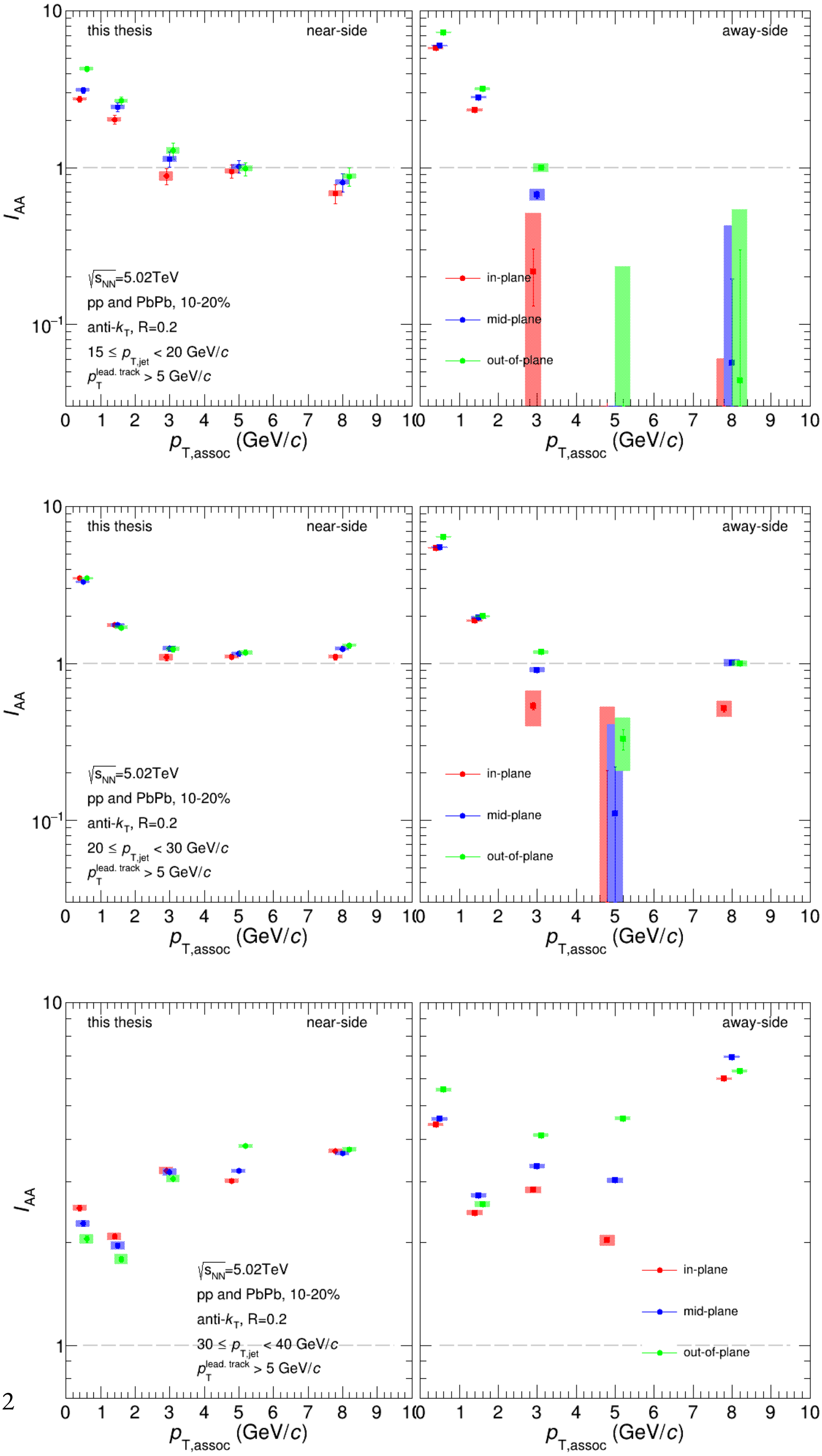

Figure A.49: I_{AA} for 10-20% centrality

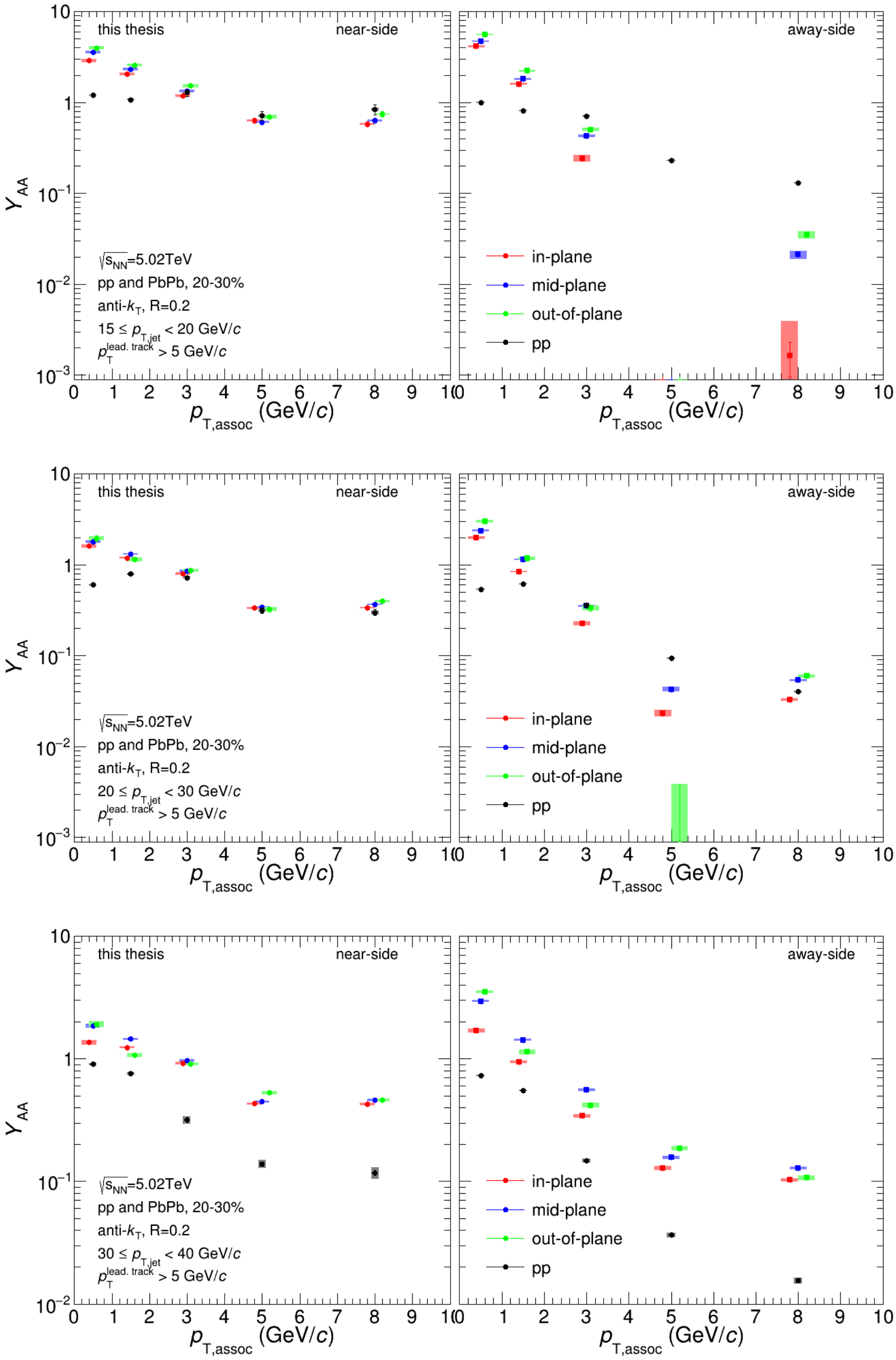

Figure A.50: Per-trigger yields for 20-30% centrality PbPb and pp

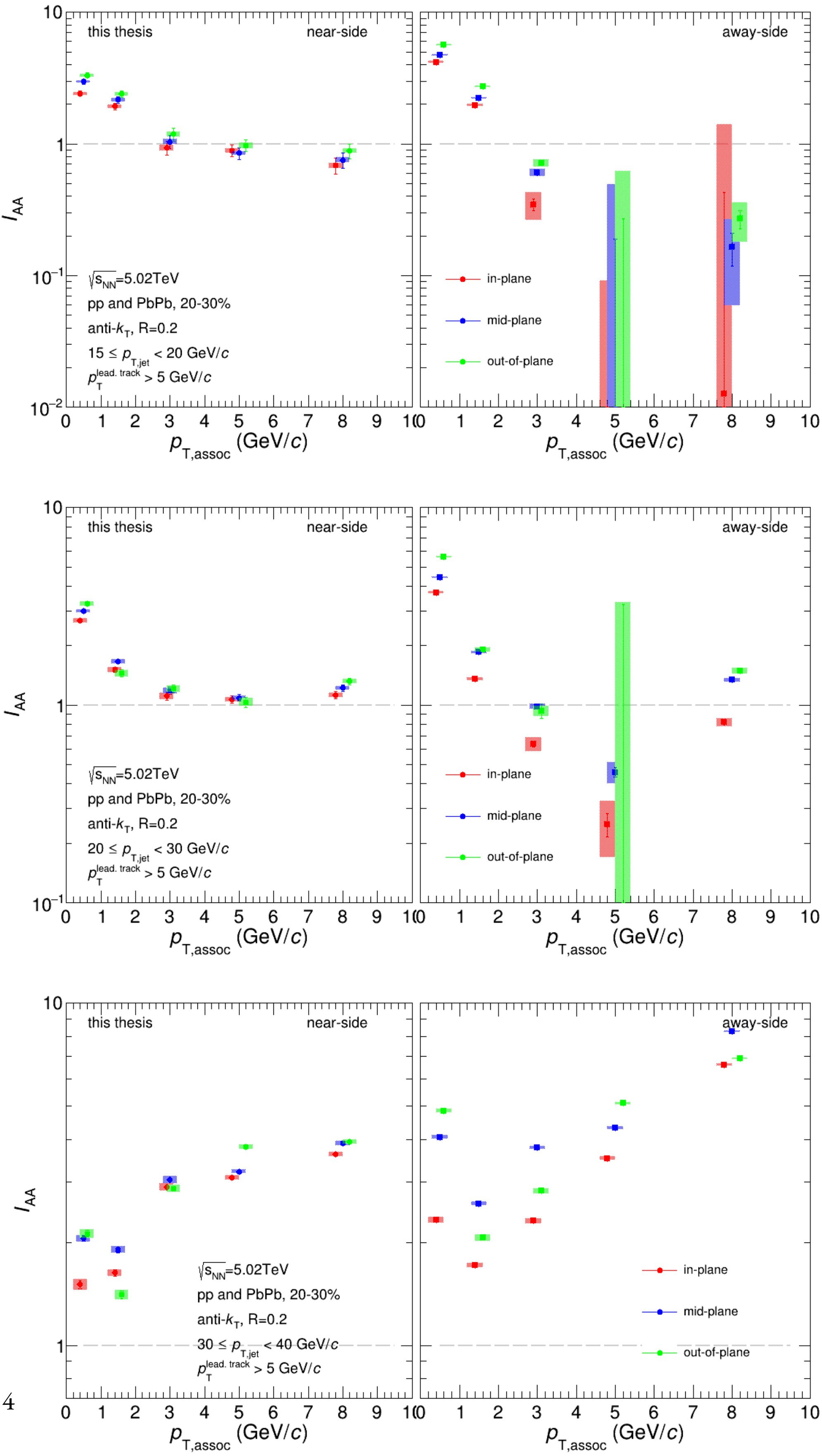

Figure A.51: I_{AA} for 20-30% centrality

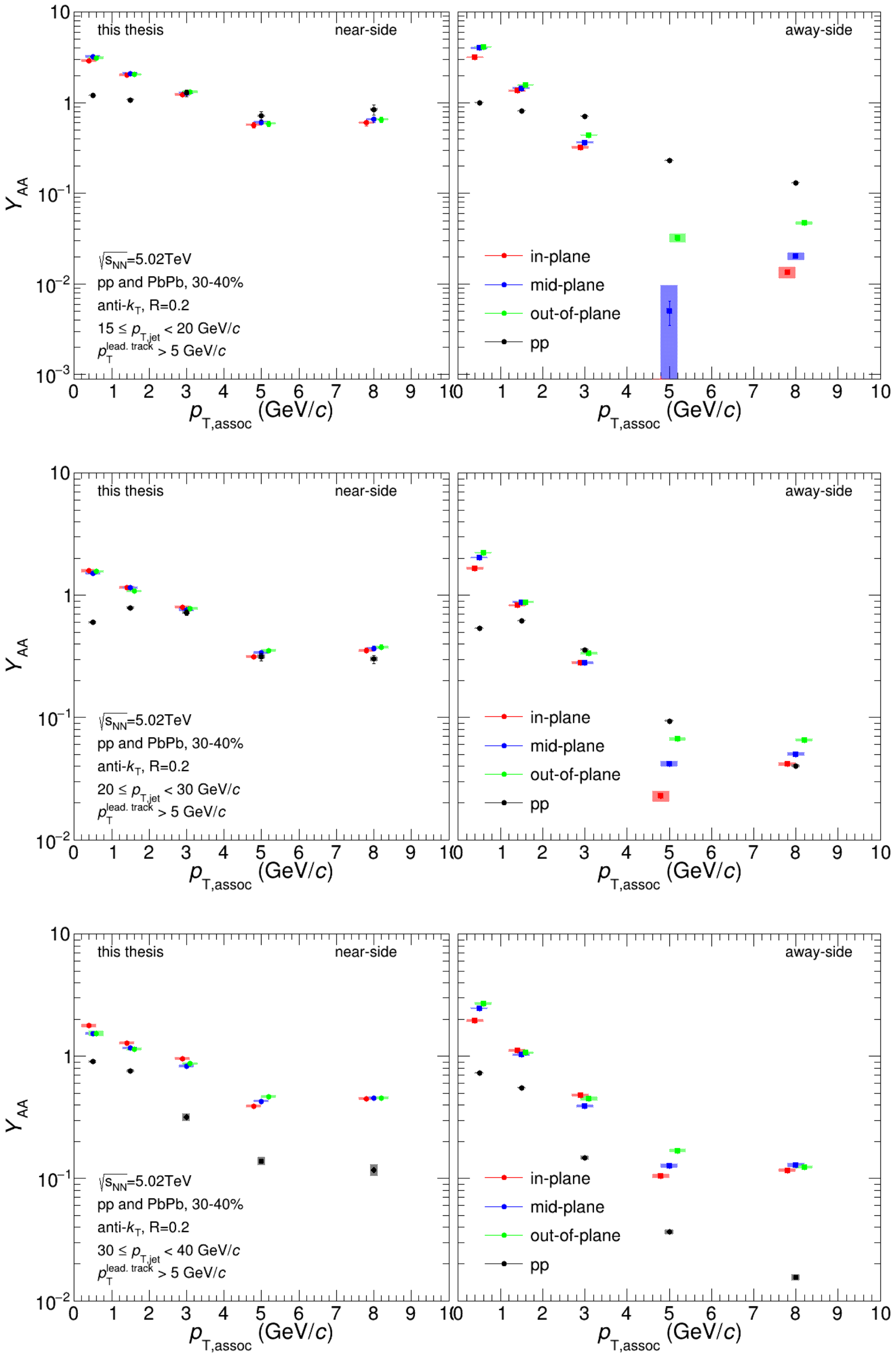

Figure A.52: Per-trigger yields for 30-40% centrality PbPb and pp

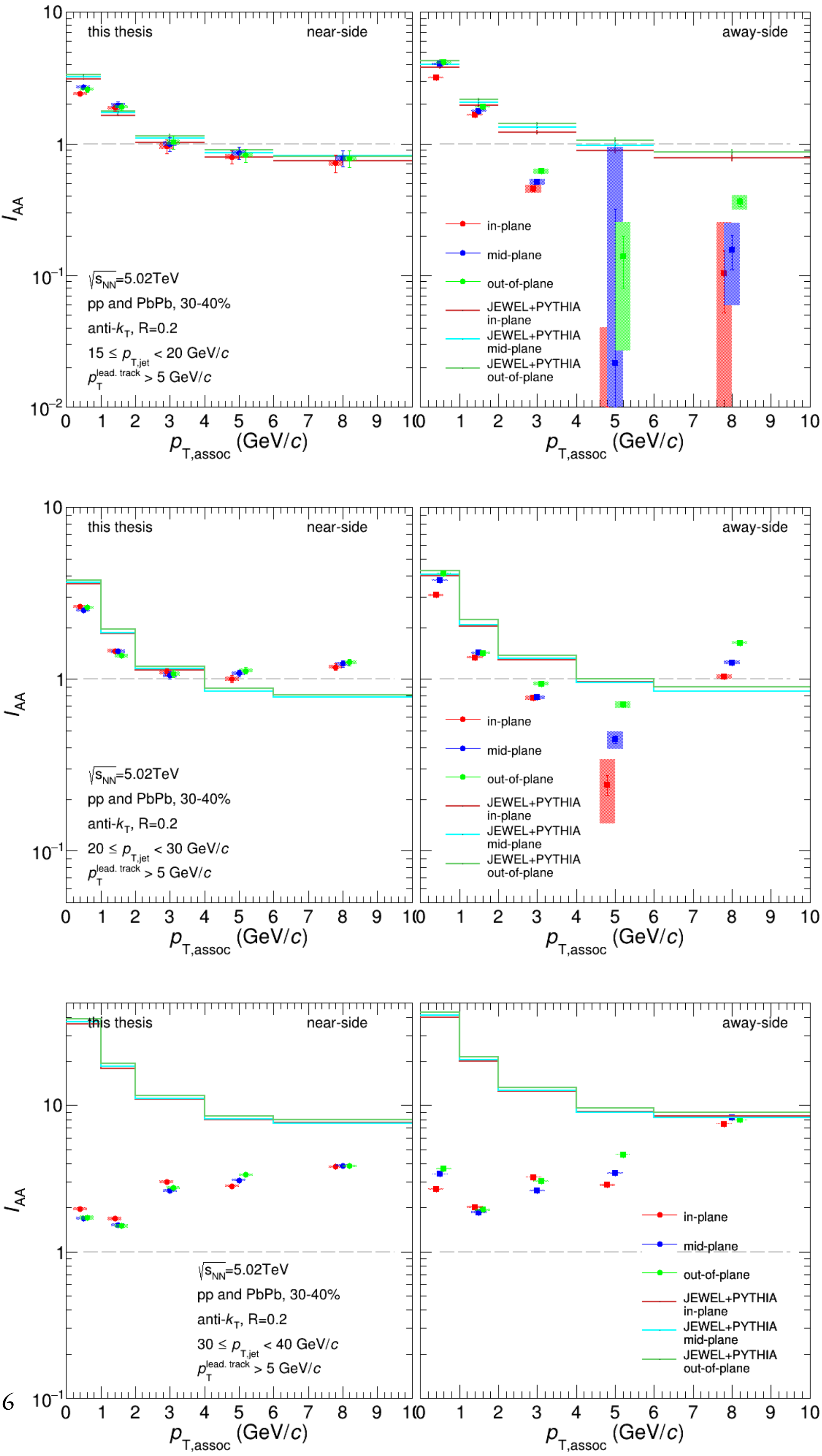

Figure A.53: I_{AA} for 30-40% centrality

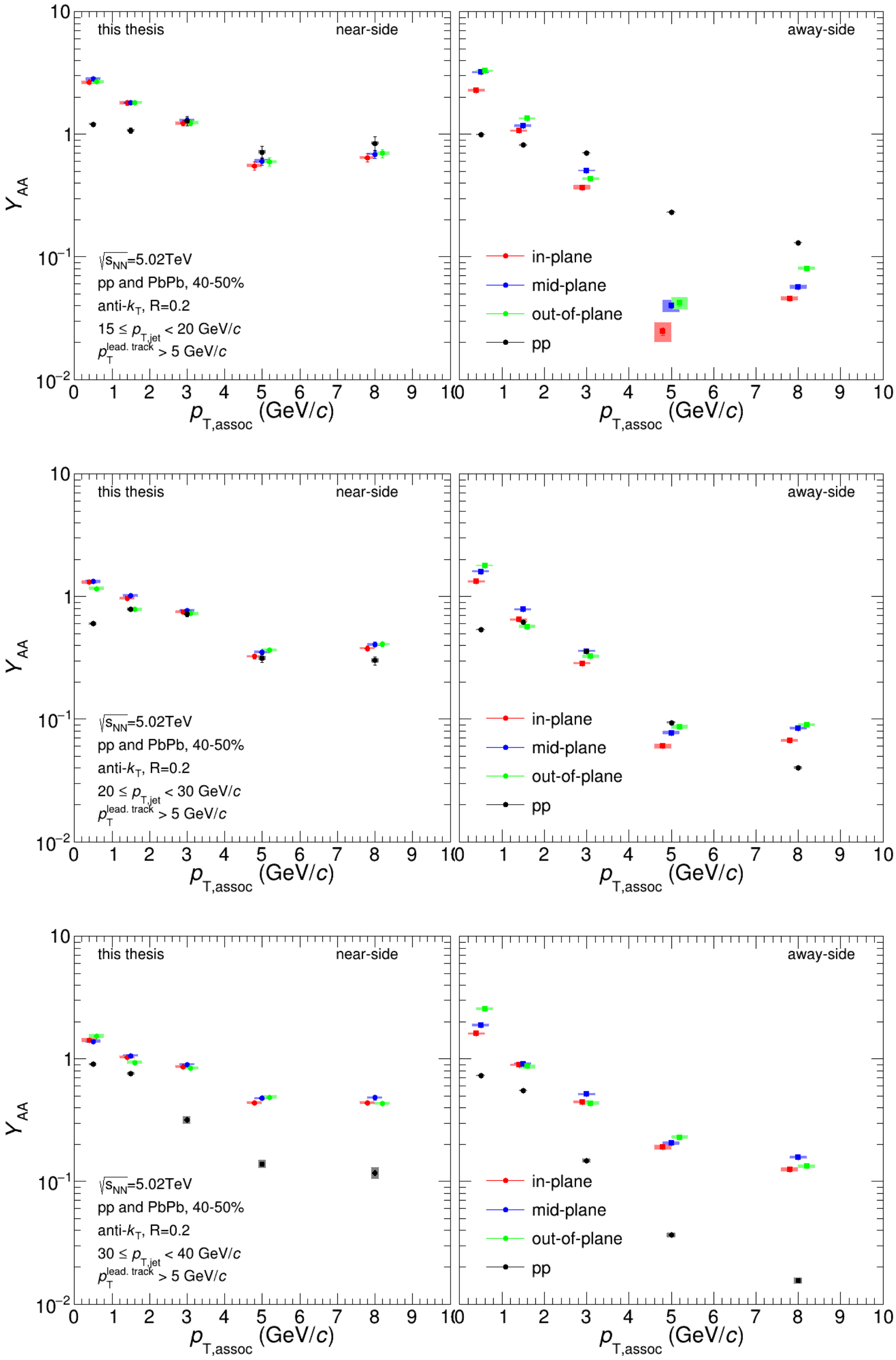

Figure A.54: Per-trigger yields for 40-50% centrality PbPb and pp

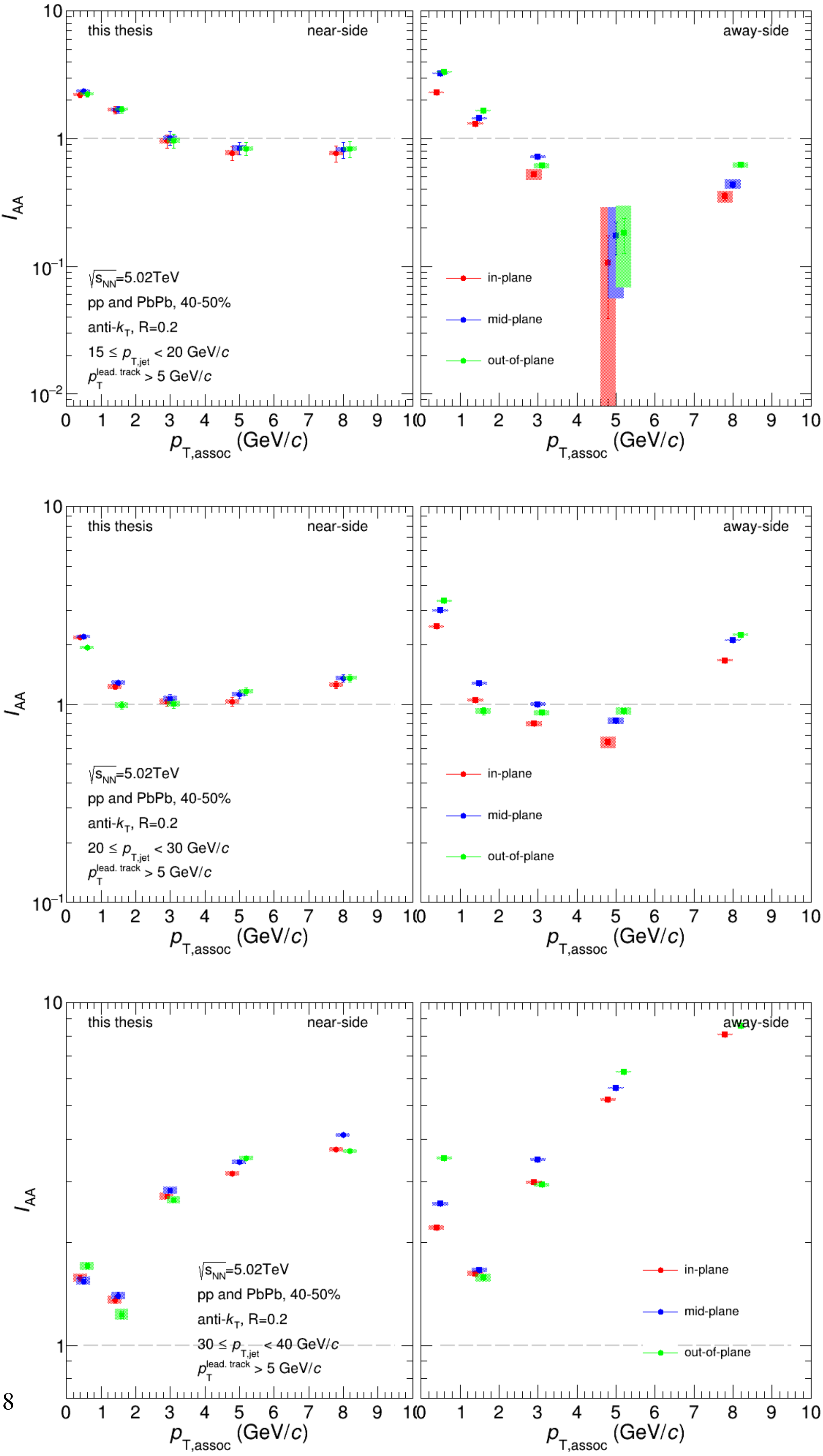

Figure A.55: I_{AA} for 40-50% centrality

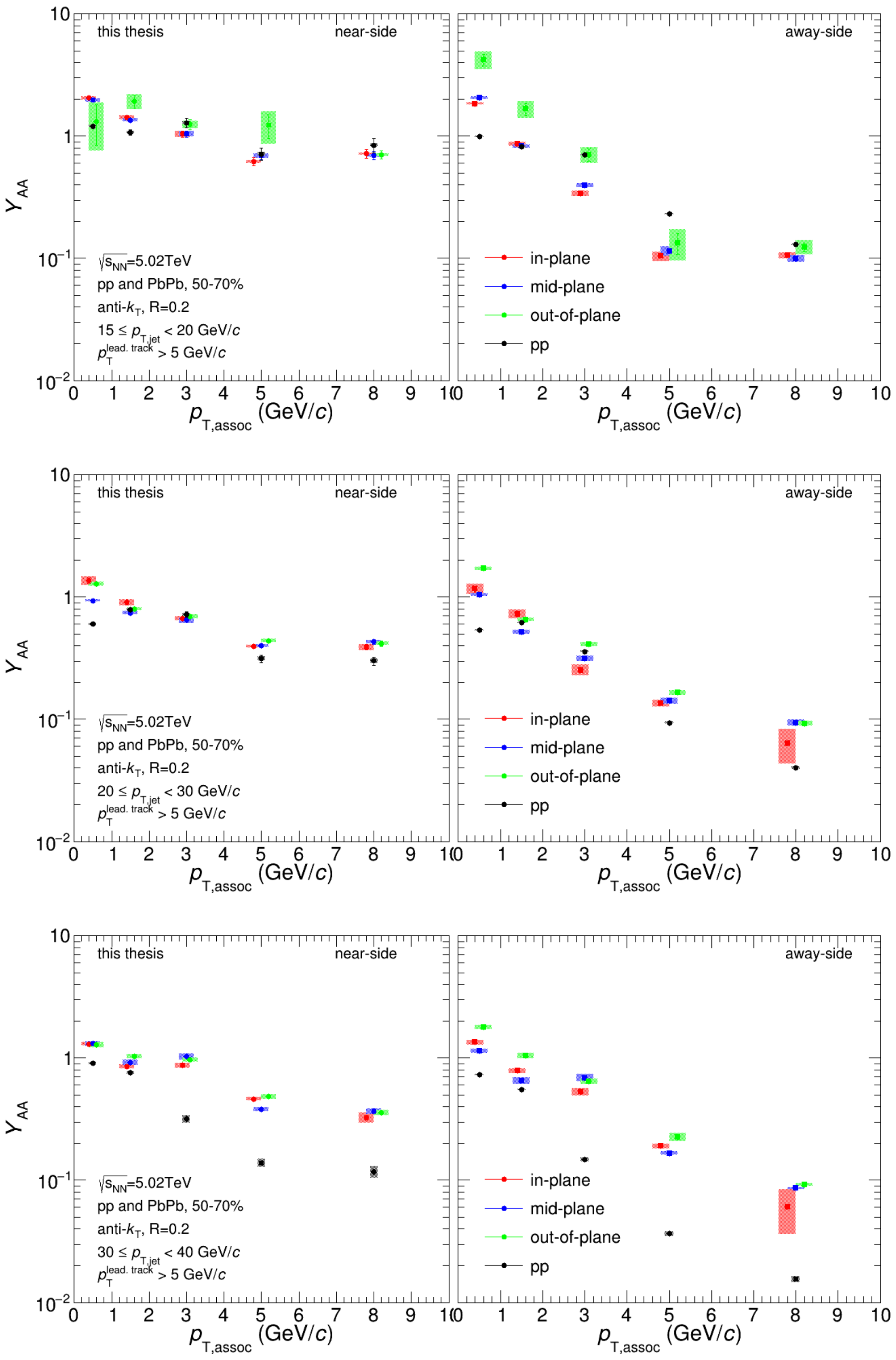

Figure A.56: Per-trigger yields for 50-70% centrality PbPb and pp

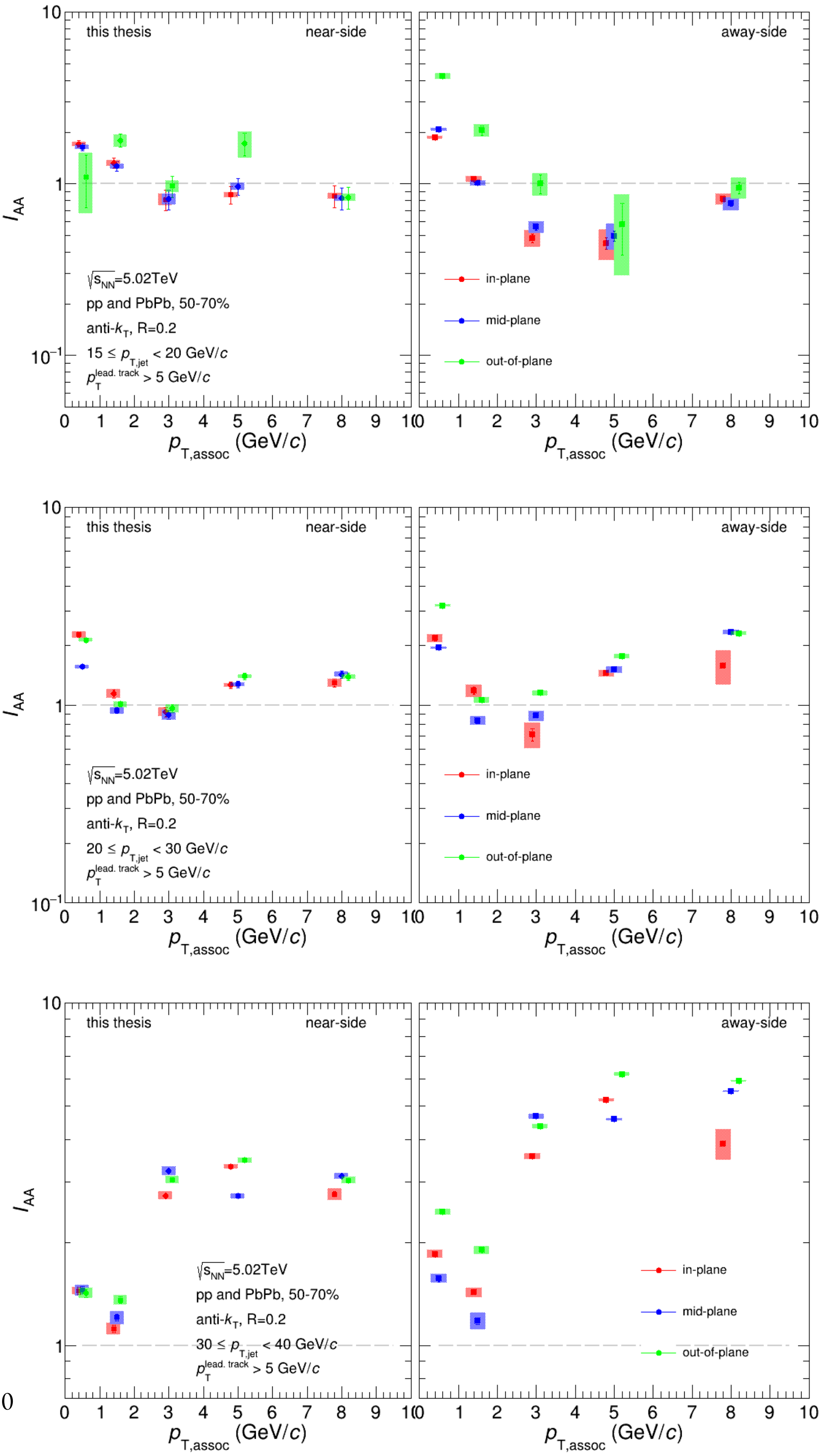

Figure A.57: I_{AA} for 50-70% centrality

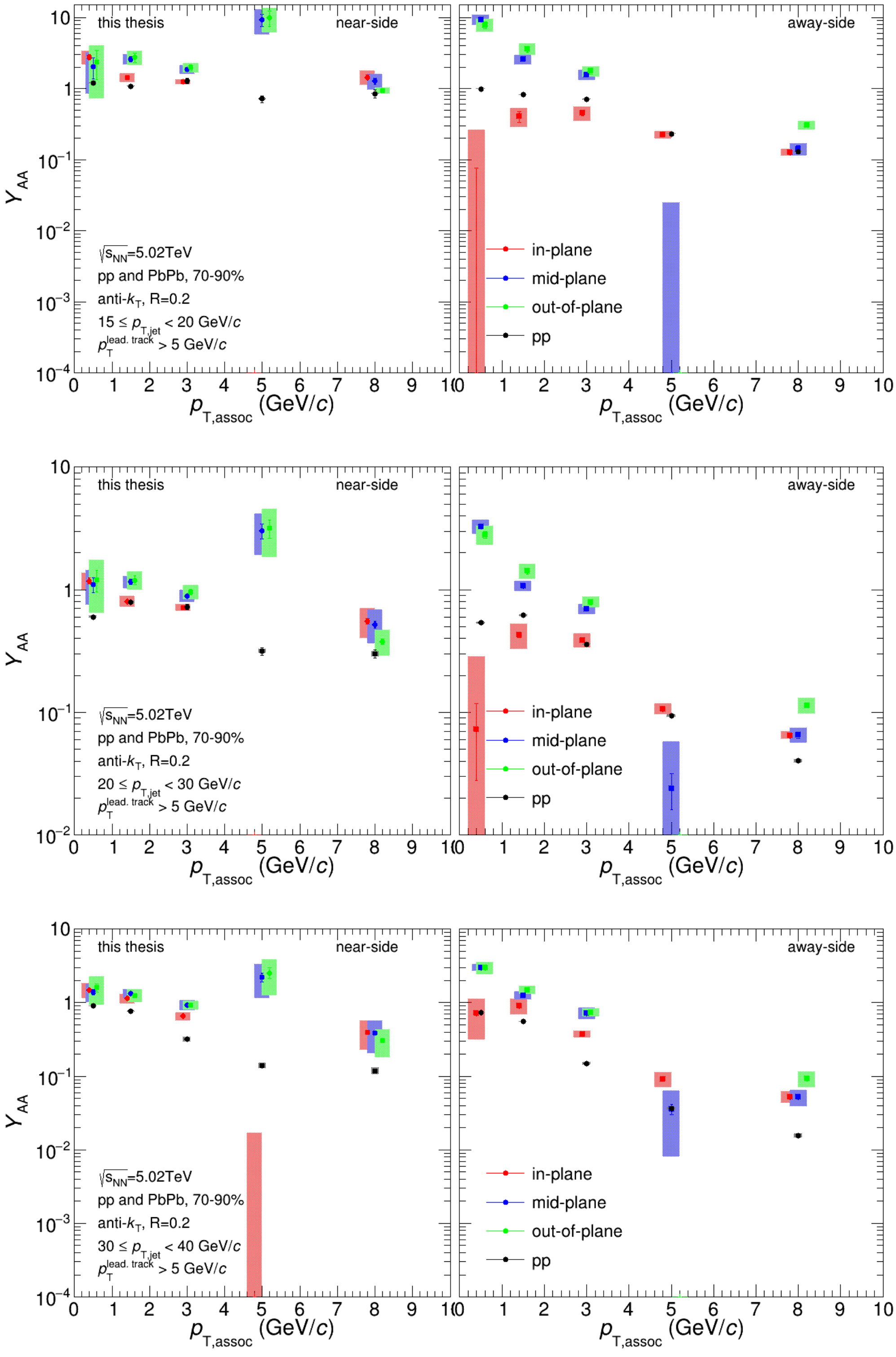

Figure A.58: Per-trigger yields for 70-90% centrality PbPb and pp

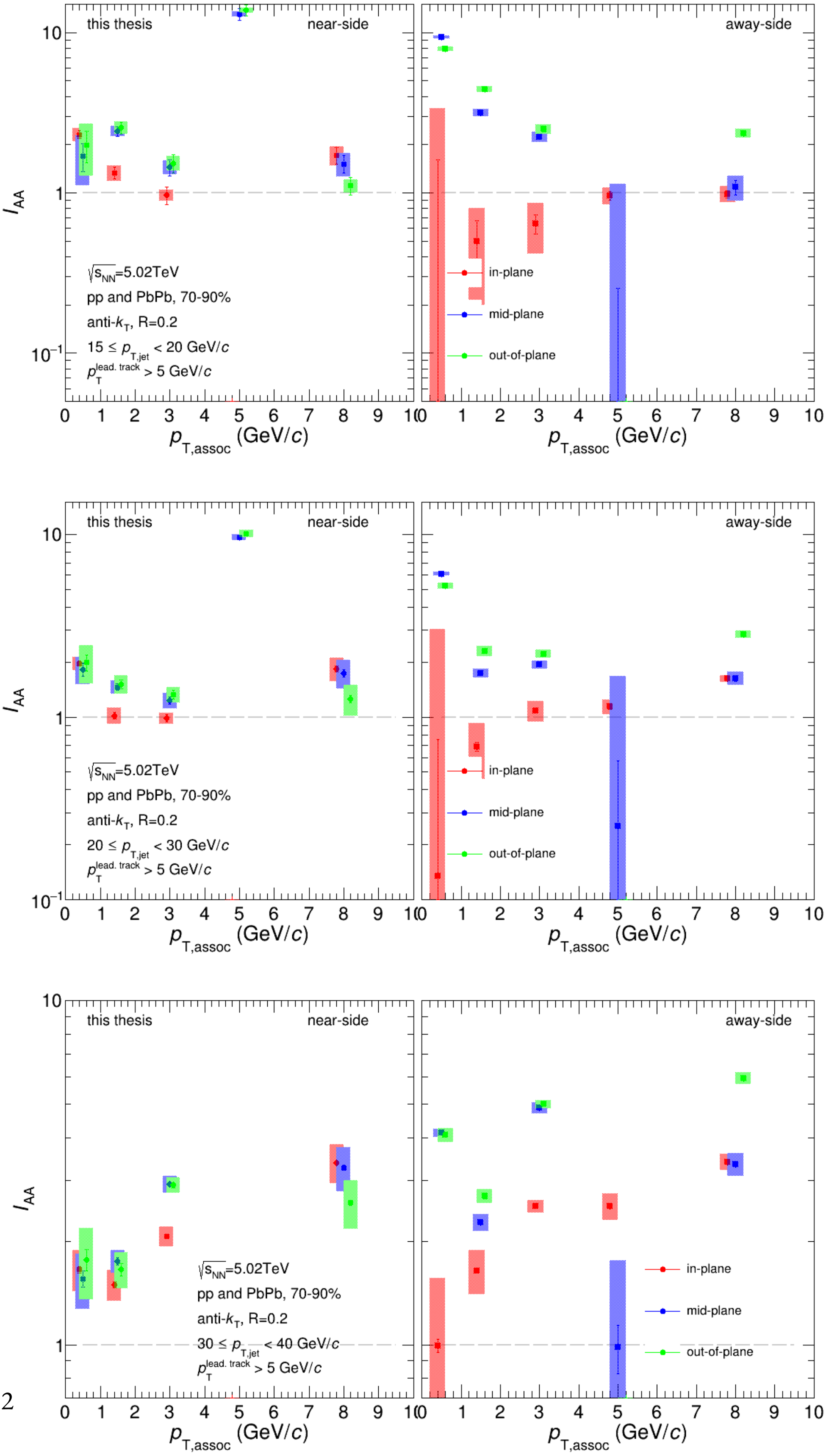

Figure A.59: I_{AA} for 70-90% centrality

BIBLIOGRAPHY

[1] M. Thomson, *Modern Particle Physics*. Cambridge University Press, 2013.

[2] S. Bethke, "Experimental tests of asymptotic freedom", *Prog. Part. Nucl. Phys.* **58** (2007) 351–386, `arXiv:hep-ex/0606035`.

[3] H.-T. Ding, F. Karsch, and S. Mukherjee, "Thermodynamics of strong-interaction matter from Lattice QCD", *Int. J. Mod. Phys. E* **24** (2015) 1530007, `arXiv:1504.05274 [hep-lat]`.

[4] **HotQCD** Collaboration, A. Bazavov *et al.*, "Equation of state in (2+1)-flavor QCD", *Phys. Rev. D* **90** (2014) 094503, `arXiv:1407.6387 [hep-lat]`.

[5] R. Stock, *Relativistic Nucleus-Nucleus Collisions and the QCD Matter Phase Diagram*, pp. 311–453. Springer International Publishing, 2020.

[6] M. L. Miller, K. Reygers, S. J. Sanders, and P. Steinberg, "Glauber modeling in high energy nuclear collisions", *Ann. Rev. Nucl. Part. Sci.* **57** (2007) 205–243, `arXiv:nucl-ex/0701025`.

[7] S. A. Voloshin, A. M. Poskanzer, and R. Snellings, "Collective phenomena in non-central nuclear collisions", *Landolt-Bornstein* **23** (2010) 293–333, `arXiv:0809.2949 [nucl-ex]`.

[8] **STAR** Collaboration, C. Adler *et al.*, "Azimuthal anisotropy and correlations in the hard scattering regime at RHIC", *Phys. Rev. Lett.* **90** (2003) 032301, `arXiv:nucl-ex/0206006`.

[9] S. Sarkar, H. Satz, and B. Sinha, *The Physics of the Quark-Gluon Plasma*. Springer, 2010.

[10] **ALICE** Collaboration, S. Acharya *et al.*, "Measurement of charged jet cross section in pp collisions at $\sqrt{s} = 5.02$ TeV", *Phys. Rev. D* **100** (2019) 092004, `arXiv:1905.02536 [nucl-ex]`.

[11] **PHENIX** Collaboration, S. S. Adler *et al.*, "Common suppression pattern of eta and pi0 mesons at high transverse momentum in Au+Au collisions at $\sqrt{s_{NN}} =$ 200 GeV", *Phys. Rev. Lett.* **96** (2006) 202301, `arXiv:nucl-ex/0601037`.

[12] **ALICE** Collaboration, S. Acharya *et al.*, "Transverse momentum spectra and nuclear modification factors of charged particles in pp, p-Pb and Pb-Pb collisions at the LHC", *JHEP* **11** (2018) 013, `arXiv:1802.09145 [nucl-ex]`.

[13] **ALICE** Collaboration, S. Acharya *et al.*, "Jet-hadron correlations measured relative to the second order event plane in Pb-Pb collisions at $\sqrt{s_{\mathrm{NN}}} = 2.76$ TeV", *Phys. Rev. C* **101** (2020) 064901, `arXiv:1910.14398 [nucl-ex]`.

[14] **ALICE** Collaboration, K. Aamodt *et al.*, "Particle-yield modification in jet-like azimuthal di-hadron correlations in Pb-Pb collisions at $\sqrt{s_{NN}} = 2.76$ TeV", *Phys. Rev. Lett.* **108** (2012) 092301, `arXiv:1110.0121 [nucl-ex]`.

[15] **PHENIX** Collaboration, A. Adare *et al.*, "Suppression of away-side jet fragments with respect to the reaction plane in Au+Au collisions at $\sqrt{s_{NN}} = 200$ GeV", *Phys. Rev. C* **84** (2011) 024904, `arXiv:1010.1521 [nucl-ex]`.

[16] "CERN's accelerator complex." `https://www.home.cern/science/accelerators/accelerator-complex`.

[17] "ALICE Schematics." `https://cds.cern.ch/record/2263642`. accessed: 19-07-2024.

[18] **ALICE** Collaboration, P. Cortese *et al.*, "ALICE technical design report on forward detectors: FMD, T0 and V0", Tech. Rep. CERN-LHCC-2004-025, Sept, 2004.

[19] **ALICE** Collaboration, E. Abbas *et al.*, "Performance of the ALICE VZERO system", *JINST* **8** (2013) P10016, `arXiv:1306.3130 [nucl-ex]`.

[20] J. Alme *et al.*, "The ALICE TPC, a large 3-dimensional tracking device with fast readout for ultra-high multiplicity events", *Nucl. Instrum. Meth. A* **622** (2010) 316–367, `arXiv:1001.1950 [physics.ins-det]`.

[21] **ALICE TPC** Collaboration, W. Yu, "Particle identification of the ALICE TPC via dE/dx", *Nucl. Instrum. Meth. A* **706** (2013) 55–58.

[22] **ALICE** Collaboration, S. Acharya *et al.*, "The ALICE Transition Radiation Detector: construction, operation, and performance", *Nucl. Instrum. Meth. A* **881** (2018) 88–127, `arXiv:1709.02743 [physics.ins-det]`.

[23] M. Cacciari, G. P. Salam, and G. Soyez, "The anti-k_t jet clustering algorithm", *JHEP* **04** (2008) 063, `arXiv:0802.1189 [hep-ph]`.

[24] **HotQCD** Collaboration, A. Bazavov *et al.*, "Chiral crossover in QCD at zero and non-zero chemical potentials", *Phys. Lett. B* **795** (2019) 15–21, `arXiv:1812.08235 [hep-lat]`.

[25] S. Borsanyi, Z. Fodor, J. N. Guenther, R. Kara, S. D. Katz, P. Parotto, A. Pasztor, C. Ratti, and K. K. Szabo, "QCD Crossover at Finite Chemical Potential from Lattice Simulations", *Phys. Rev. Lett.* **125** (2020) 052001, `arXiv:2002.02821 [hep-lat]`.

[26] J. C. Collins and M. J. Perry, "Superdense Matter: Neutrons Or Asymptotically Free Quarks?", *Phys. Rev. Lett.* **34** (1975) 1353.

[27] E. Annala, T. Gorda, A. Kurkela, J. Nättilä, and A. Vuorinen, "Evidence for quark-matter cores in massive neutron stars", *Nature Phys.* **16** (2020) 907–910, `arXiv:1903.09121 [astro-ph.HE]`.

[28] "RHIC | Relativistic Heavy Ion Collider." `https://www.bnl.gov/rhic/rhic.php`.

[29] M. Connors, C. Nattrass, R. Reed, and S. Salur, "Jet measurements in heavy ion physics", *Rev. Mod. Phys.* **90** (2018) 025005, `arXiv:1705.01974 [nucl-ex]`.

[30] **ALICE** Collaboration, J. Adam *et al.*, "Higher harmonic flow coefficients of identified hadrons in Pb-Pb collisions at $\sqrt{s_{\mathrm{NN}}} = 2.76$ TeV", *JHEP* **09** (2016) 164, `arXiv:1606.06057 [nucl-ex]`.

[31] J. E. Huth *et al.*, "Toward a standardization of jet definitions", in *1990 DPF Summer Study on High-energy Physics: Research Directions for the Decade (Snowmass 90)*, pp. 0134–136. Dec, 1990.

[32] R. Baier, Y. L. Dokshitzer, A. H. Mueller, S. Peigne, and D. Schiff, "Radiative energy loss of high-energy quarks and gluons in a finite volume quark - gluon plasma", *Nucl. Phys. B* **483** (1997) 291–320, `arXiv:hep-ph/9607355`.

[33] L. D. Landau and I. Pomeranchuk, "Limits of applicability of the theory of bremsstrahlung electrons and pair production at high-energies", *Dokl. Akad. Nauk Ser. Fiz.* **92** (1953) 535–536.

[34] L. D. Landau and I. Pomeranchuk, "Electron cascade process at very high-energies", *Dokl. Akad. Nauk Ser. Fiz.* **92** (1953) 735–738.

[35] A. B. Migdal, "Bremsstrahlung and pair production in condensed media at high-energies", *Phys. Rev.* **103** (1956) 1811–1820.

[36] J. G. Milhano and K. C. Zapp, "Origins of the di-jet asymmetry in heavy ion collisions", *Eur. Phys. J. C* **76** (2016) 288, `arXiv:1512.08107 [hep-ph]`.

[37] J. Noronha-Hostler, B. Betz, J. Noronha, and M. Gyulassy, “Event-by-event hydrodynamics + jet energy loss: A solution to the $R_{AA} \otimes v_2$ puzzle”, *Phys. Rev. Lett.* **116** (2016) 252301, `arXiv:1602.03788 [nucl-th]`.

[38] Y. He, M. Nie, S. Cao, R. Ma, L. Yi, and H. Caines, “Deciphering yield modification of hadron-triggered semi-inclusive recoil jets in heavy-ion collisions”, *Phys. Lett. B* **854** (2024) 138739, `arXiv:2401.05238 [nucl-th]`.

[39] **STAR** Collaboration, H. Agakishiev *et al.*, “Event-plane-dependent dihadron correlations with harmonic v_n subtraction in Au + Au collisions at $\sqrt{s_{NN}} = 200$ GeV”, *Phys. Rev. C* **89** (2014) 041901, `arXiv:1404.1070 [nucl-ex]`.

[40] L. Evans and P. Bryant, “LHC Machine”, *JINST* **3** (2008) S08001.

[41] “LHC Guide.” `https://cds.cern.ch/record/2255762/files/?ln=de`, 2017.

[42] **Particle Data Group** Collaboration, R. L. Workman *et al.*, “Review of Particle Physics”, *PTEP* **2022** (2022) 083C01.

[43] **ALICE** Collaboration, K. Aamodt *et al.*, “The ALICE experiment at the CERN LHC”, *JINST* **3** (2008) S08002.

[44] **ALICE** Collaboration, B. B. Abelev *et al.*, “Performance of the ALICE Experiment at the CERN LHC”, *Int. J. Mod. Phys. A* **29** (2014) 1430044, `arXiv:1402.4476 [nucl-ex]`.

[45] “The CERN Experimental Programme - Grey Book database.” `"https://greybook.cern.ch/experiment/detail?id=ALICE"`. accessed: 28-07-2024.

[46] **ALICE** Collaboration, G. Dellacasa *et al.*, “ALICE: Technical design report of the time projection chamber”, Tech. Rep. CERN-OPEN-2000-183, CERN-LHCC-2000-001, Jan, 2000.

[47] **ALICE TPC** Collaboration, J. Adolfsson *et al.*, “The upgrade of the ALICE TPC with GEMs and continuous readout”, *JINST* **16** (2021) P03022, `arXiv:2012.09518 [physics.ins-det]`.

[48] **ALICE** Collaboration, P. Cortese, “ALICE transition-radiation detector: Technical Design Report”, Tech. Rep. CERN-LHCC-2001-021, ALICE-TDR-9, LYCEN-2001-97, ALICE-TDR-9, CERN-LHCC-2001-021, LYCEN-2001-97, 2001.

[49] V. L. Ginzburg and I. M. Frank, “Radiation of a uniformly moving electron due to its transition from one medium into another”, *J. Phys. (USSR)* **9** (1945) 353–362.

[50] **ALICE** Collaboration, F. Carnesecchi, "Performance of the ALICE Time-Of-Flight detector at the LHC", *JINST* **14** (2019) C06023, `arXiv:1806.03825 [physics.ins-det]`.

[51] R. E. Kalman, "A New Approach to Linear Filtering and Prediction Problems", *J. Fluids Eng.* **82** (1960) 35–45.

[52] C. Bierlich *et al.*, "A comprehensive guide to the physics and usage of PYTHIA 8.3", *SciPost Phys. Codeb.* **2022** (2022) 8, `arXiv:2203.11601 [hep-ph]`.

[53] X.-N. Wang and M. Gyulassy, "HIJING: A Monte Carlo model for multiple jet production in pp, pA and AA collisions", *Phys. Rev. D* **44** (1991) 3501–3516.

[54] W.-T. Deng, X.-N. Wang, and R. Xu, "Hadron production in p+p, p+Pb, and Pb+Pb collisions with the HIJING 2.0 model at energies available at the CERN Large Hadron Collider", *Phys. Rev. C* **83** (2011) 014915, `arXiv:1008.1841 [hep-ph]`.

[55] N. Grünwald, "Studies of jets in heavy-ion collisions at alice with a novel mixed-event approach", Master's thesis, Heidelberg University, 2022.

[56] K. C. Zapp, "JEWEL 2.0.0: directions for use", *Eur. Phys. J. C* **74** (2014) 2762, `arXiv:1311.0048 [hep-ph]`.

[57] K. C. Zapp, F. Krauss, and U. A. Wiedemann, "A perturbative framework for jet quenching", *JHEP* **03** (2013) 080, `arXiv:1212.1599 [hep-ph]`.

[58] K. Zapp, G. Ingelman, J. Rathsman, J. Stachel, and U. A. Wiedemann, "A Monte Carlo Model for 'Jet Quenching'", *Eur. Phys. J. C* **60** (2009) 617–632, `arXiv:0804.3568 [hep-ph]`.

[59] A. Buckley, J. Ferrando, S. Lloyd, K. Nordström, B. Page, M. Rüfenacht, M. Schönherr, and G. Watt, "LHAPDF6: parton density access in the LHC precision era", *Eur. Phys. J. C* **75** (2015) 132, `arXiv:1412.7420 [hep-ph]`.

[60] J. D. Bjorken, "Highly Relativistic Nucleus-Nucleus Collisions: The Central Rapidity Region", *Phys. Rev. D* **27** (1983) 140–151.

[61] J. G. Milhano and K. Zapp, "Improved background subtraction and a fresh look at jet sub-structure in JEWEL", *Eur. Phys. J. C* **82** (2022) 1010, `arXiv:2207.14814 [hep-ph]`.

[62] **ALICE** Collaboration, J. Adam *et al.*, "Azimuthal anisotropy of charged jet production in $\sqrt{s_{\mathrm{NN}}} = 2.76$ TeV Pb-Pb collisions", *Phys. Lett. B* **753** (2016) 511–525, `arXiv:1509.07334 [nucl-ex]`.

[63] A. M. Poskanzer and S. A. Voloshin, "Methods for analyzing anisotropic flow in relativistic nuclear collisions", *Phys. Rev. C* **58** (1998) 1671–1678, `arXiv:nucl-ex/9805001`.

[64] S. Catani, Y. L. Dokshitzer, M. H. Seymour, and B. R. Webber, "Longitudinally invariant $k_\perp$-clustering algorithms for hadron-hadron collisions", *Nucl. Phys. B* **406** (1993) 187–224.

[65] M. Cacciari, G. P. Salam, and G. Soyez, "FastJet User Manual", *Eur. Phys. J. C* **72** (2012) 1896, `arXiv:1111.6097 [hep-ph]`.

[66] M. Cacciari and G. P. Salam, "Dispelling the N^3 myth for the k_t jet-finder", *Phys. Lett. B* **641** (2006) 57–61, `arXiv:hep-ph/0512210`.

[67] **STAR** Collaboration, L. Adamczyk *et al.*, "Measurements of jet quenching with semi-inclusive hadron+jet distributions in Au+Au collisions at $\sqrt{s_{NN}} = 200$ GeV", *Phys. Rev. C* **96** (2017) 024905, `arXiv:1702.01108 [nucl-ex]`.

[68] **ALICE** Collaboration, N. A. Grünwald, "New measurements of inclusive jet suppression and jet v_2 in Pb–Pb collisions at $\sqrt{s_{NN}} = 5.02$ TeV with ALICE", *EPJ Web Conf.* **296** (2024) 11005.

[69] N. Sharma, J. Mazer, M. Stuart, and C. Nattrass, "Background subtraction methods for precision measurements of di-hadron and jet-hadron correlations in heavy ion collisions", *Phys. Rev. C* **93** (2016) 044915, `arXiv:1509.04732 [nucl-ex]`.

[70] J. Bielcikova, S. Esumi, K. Filimonov, S. Voloshin, and J. P. Wurm, "Elliptic flow contribution to two particle correlations at different orientations to the reaction plane", *Phys. Rev. C* **69** (2004) 021901, `arXiv:nucl-ex/0311007`.

[71] G. Bohm and G. Zech, *Introduction to Statistics and Data Analysis for Physicists; 2nd revised edition*. DESY, Hamburg, 2010.

[72] G. D'Agostini, "A Multidimensional unfolding method based on Bayes' theorem", *Nucl. Instrum. Meth. A* **362** (1995) 487–498.

[73] G. D'Agostini, "Improved iterative Bayesian unfolding", in *Alliance Workshop on Unfolding and Data Correction*. Oct, 2010. `arXiv:1010.0632 [physics.data-an]`.

[74] **ALICE** Collaboration, B. Abelev *et al.*, "Measurement of charged jet suppression in Pb-Pb collisions at $\sqrt{s_{NN}} = 2.76$ TeV",*JHEP* **03** (2014) 013, `arXiv:1311.0633 [nucl-ex]`.

[75] D. L. D. Keijdener, *Azimuthal differences of quenched jets*. PhD thesis, Utrecht University, 2023.